University of Genoa

Doctorate school of Chemical and Materials Sciences and Technologies
Curriculum of Medicinal, Food and Cosmetic Sciences
XXX Cycle

STUDY OF DERIVATIVES FOR DIAGNOSTIC IMAGING OF EARLY ATHEROMATOUS LESIONS

Tutor

Prof. Gabriele Caviglioli

PhD student

Sara Pastorino

15 March 2018

TABLE OF CONTENTS

1. GENERAL INTRODUCTION

1.1 Pathogenesis of Atherosclerosis

Atherosclerosis (from the Greek words ‘sclerosis’, meaning hardening and ‘athere’, meaning gruel) is a chronic disease of large and medium-sized arteries, characterized by endothelial dysfunction, vascular inflammation and the accumulation of modified lipid, inflammatory cells and cell debris in ‘plaques’ within the vascular wall [1].

This disease begins in the most vulnerable sites of the blood vessels: near the branch points and along the inner curvature or regions in which the uniformity of the blood flow is disturbed. Cells in the tubular regions of the arteries, where blood flow is uniform and laminar, are ellipsoid in shape and aligned in the flow direction; on the contrary, cells in regions of arterial branching or curvature, where flow is disturbed, have polygonal shapes and no particular orientation [2]. Impaired laminar flow induces a small and oscillating shear stress on the artery wall, where endothelial cells (EC) may react by different mechanosensors (PCAM-1/VE-cadherin/VEGFR2) to this mechanical stress. The endothelial cells respond to shear stress by increasing the synthesis of vasoactive mediators, such as nitric oxide (NO), to control vascular tone, which causes an immediate reduction in shear stress.

Additionally, cells react by secreting extracellular matrix proteins and matrix metalloproteinases (MMPs) to promote remodelling and repair, and by expressing growth factors, e.g. TGF-β (transforming growth factor beta), to control cell survival and proliferation. However, if the shear stress is still present, through mechanotransduction, the nuclear factor-κB (NF-κB) path is triggered as part of the inflammatory process. Elevated NF-κB activity results in the expression of NF-κB-dependent genes, which encode adhesion molecules, such as PCAM-1, ICAM-1, VCAM-1, P-selectin and E-selectin, cytokines (TNF-α, IL-1, IL-6, IL-12) and growth factors. Regardless of mechanotrandsuction, the turbulent flow also disturbs intercellular tight junctions of the endothelium and causes thinning of the endothelial glycocalyx, which could favour migration of low density lipoprotein (LDL) and white blood cells to the subendothelial intima [3].

A primary initiating event in atherosclerotic plaque formation is the accumulation of LDL in the subendothelial matrix.

Accumulation is greater when levels of circulating LDL raise, and both transport and retention of LDL are increased in the preferred sites of lesion formation.

LDL diffuses passively through EC junctions, and its retention in the vessel wall seems to involve interactions between the LDL constituent apolipoprotein B (apoB) and matrix proteoglycans. Trapped LDL undergoes modification, including oxidation, lipolysis, proteolysis and aggregation, and such modifications contribute to inflammation as well as to foam-cell formation.

One of the most significant modifications for early lesion formation is lipid oxidation as a result of exposure to reactive oxygen species (ROS). Such modifications initially give rise to 'minimally oxidized' LDL species that stimulates the overlying ECs to produce chemotactic proteins such as monocyte chemotactic protein-1 (MCP-1) and growth factors such as macrophage colony-stimulating factor (M-CSF), resulting in the recruitment of monocytes to the vessel wall.

Oxidized LDL (OxLDL) can also inhibit the production of nitric oxide (NO), which has multiple anti-atherogenic properties, including vasorelaxation (Fig. 1).

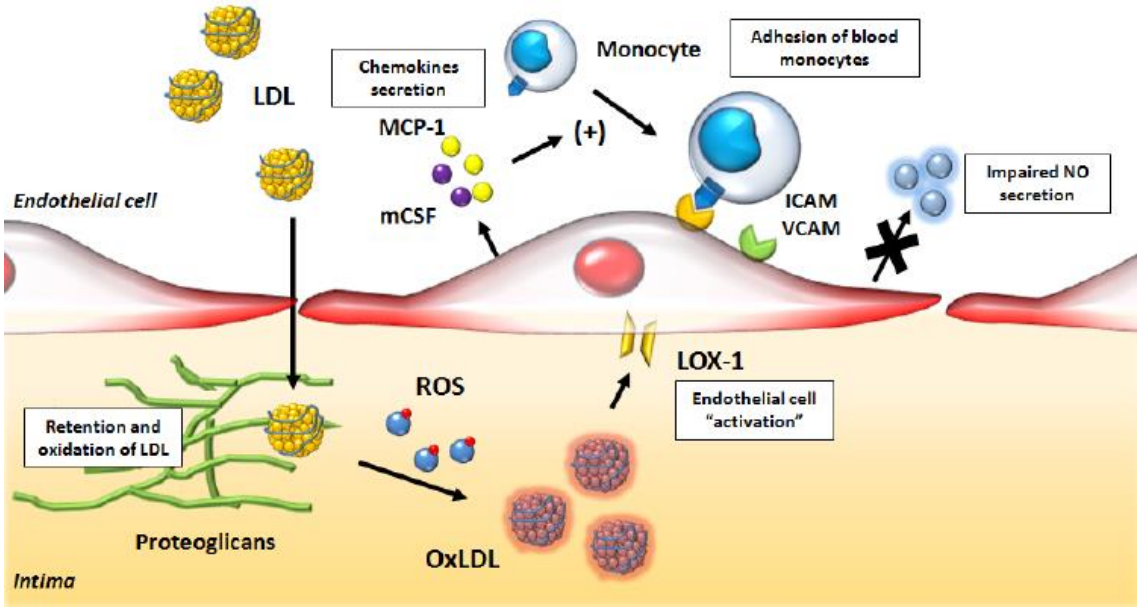

Fig. 1: Role of OxLDL in endothelial dysfunction.

The first step in adhesion is the 'rolling' of leukocytes along the endothelial surface, which is mediated by selectins that bind to carbohydrate ligands on leukocytes.

The firm adhesion of monocytes to the endothelium is mediated by the integrin VLA-4 (very late antigen-4) on these cells, which interacts with two known ligands. In fact, VLA-4 binds to sites within the first and fourth immunoglobulin-like domains of the full-length 7-domain form of vascular cell adhesion molecule-1 (VCAM-1), expressed on ECs. Another ligand for VLA-4 is fibronectin (FN): VLA-4 recognizes a sequence within the alternatively spliced connecting segment-1 (CS-1) region of FN [4].

The M-CSF cytokine stimulates the proliferation and differentiation of macrophages, and influences various macrophage functions such as the expression of scavenger receptors.

LDL must be extensively modified ('highly oxidized') before it can be taken up sufficiently rapidly by the macrophages to form foam cells. This modification presumably involves ROS produced by ECs and macrophages, but several enzymes are also thought to be involved, including myeloperoxidase, sphingomyelinase, and a secretory phospholipase.

The rapid uptake of highly oxidized (and otherwise modified) LDL particles by the macrophages, leading to foam-cell formation, is mediated by a group of receptors that recognize a wide array of ligands: the 'scavenger' receptors (SRs) such as SR-AI/II, SR-BI, cluster of differentiation 36 (CD36), lectin-like oxidized LDL receptor-1 (LOX-1) and toll-like receptors (TLRs) (Fig. 2).

The expression of these receptors is regulated by peroxisome proliferator-activated receptor-γ, a transcription factor whose ligands include oxidized fatty acids, and by cytokines such as TNF-α and interferon-γ [2].

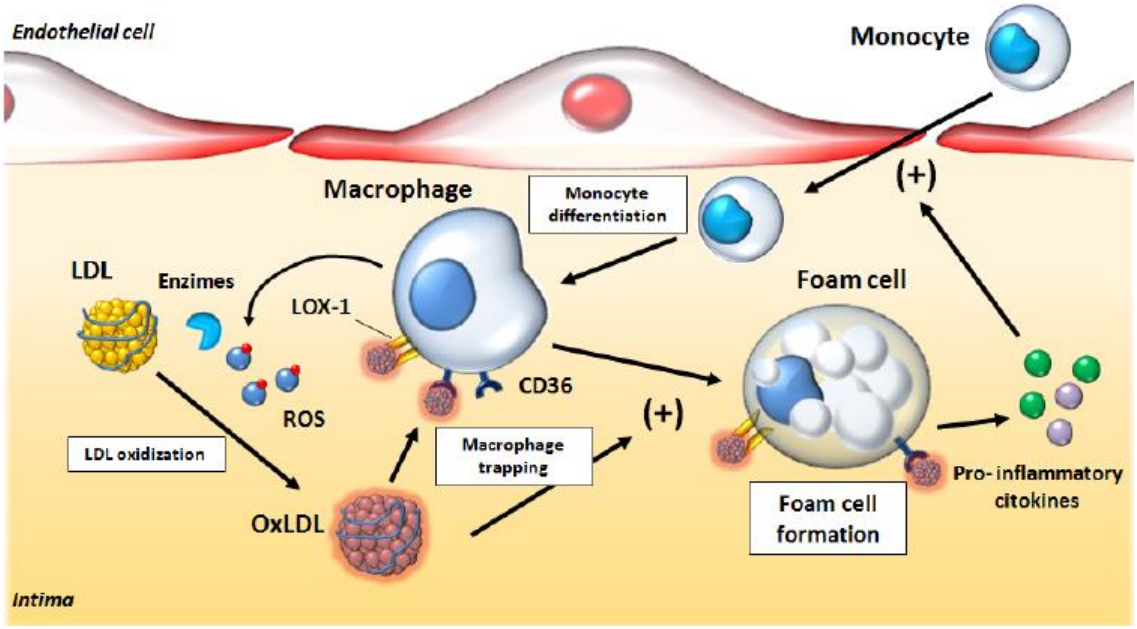

Fig. 2: Role of OxLDL in foam cell formation.

After internalization, lipoproteins are delivered to the late endosome/lysosome, where cholesteryl esters of the LDL are hydrolysed into free cholesterol (FC) and fatty acids by the lysosomal acid lipase (LAL).

To prevent the FC-associated cell toxicity, the FC released is re-esterified on the endoplasmic reticulum (ER) by ACAT1 (Acyl coenzyme A:cholesterol acyltransferase-1) and stored in cytoplasmic lipid droplets. These droplets are responsible for the foamy appearance of the macrophage and thus the name of foam cells.

The resulting cholesteryl esters are hydrolysed by neutral cholesterol ester hydrolase 1 (nCEH) to release FC via transporters-mediated efflux [5]. In fact, the accumulated cholesterol is removed from the macrophages in the subintima of the vessel wall through transporters, including ABCA1, ABCG1 and SR-B1, although passive diffusion through the plasma membrane also occurs.

ABCA1 promotes cholesterol efflux to lipid-poor apolipoprotein A-1 (apoA-1), which is the building block of HDL, whereas ABCG1 promotes efflux to mature HDL particles [6]. The balance of cholesterol influx, esterification and release is necessary to avoid lipid overload within the macrophages, and ultimately, atheroma development.

Under atherogenic conditions, the efflux of cholesterol is decreased due to reduced expression of ABCA1, ABCG1 and SR-B1; whereas, its uptake is increased due to

excessive esterification of cholesterol caused by higher ACAT1 level and lower nCEH level.

This leads to excessive CE accumulation as lipid droplets in the macrophages, thereby contributing to the formation of foam cells (Fig. 3) [5].

Such dysregulation in lipid metabolism contributes to ER stress in macrophages, which, if prolonged and combined with other insults, can ultimately result in apoptotic cell death and the release of cellular components and lipids form the necrotic core of the atheroma [6].

The maintenance of foam cells and the subsequent progression of plaque build-up is caused by the secretion of chemokines and cytokines from macrophages and foam cells. Foam cells secrete pro-inflammatory cytokines such as interleukins (IL-1, IL-6), TNF, chemokines, as well as macrophage retention factors [6].

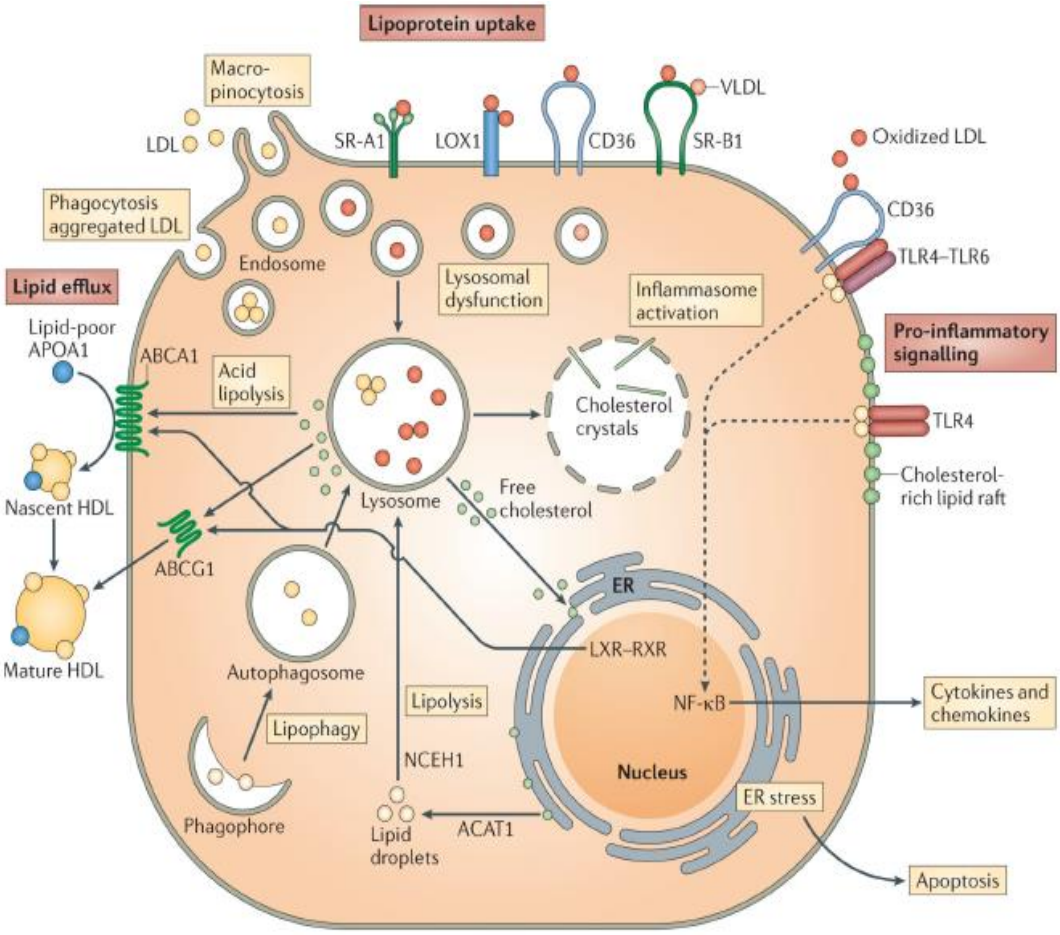

Fig. 3: Mechanisms governing macrophage lipoprotein uptake and efflux.

Macrophages, within the atherosclerotic lesion, have a decreased ability to migrate, which further promotes plaque formation as they are able to secrete cytokines, chemokines, ROS and growth factors that stimulate modified lipoprotein uptake and vascular smooth muscle cell (VSMC) proliferation [4].

VSMCs are highly specialized cells that adjust the diameter of the blood vessels and local blood pressure, thereby controlling blood flow [3]. By contraction and relaxation, they alter the luminal diameter, enabling the blood vessels to maintain an appropriate blood pressure. However, VSMCs also perform other functions, which become progressively more important during vessel remodelling under physiological conditions such as pregnancy and exercise, or after vascular injury. In these cases, VSMCs synthesize large amounts of extracellular matrix (ECM) components and increase their proliferation and migration.

The different functions that VSMCs can exert translate into a diversity of VSMC phenotypes, ranging from contractile to synthetic. The diversity becomes apparent in morphology, expression levels of VSMC marker genes, proliferative potential and migration properties (Fig. 4) [7].

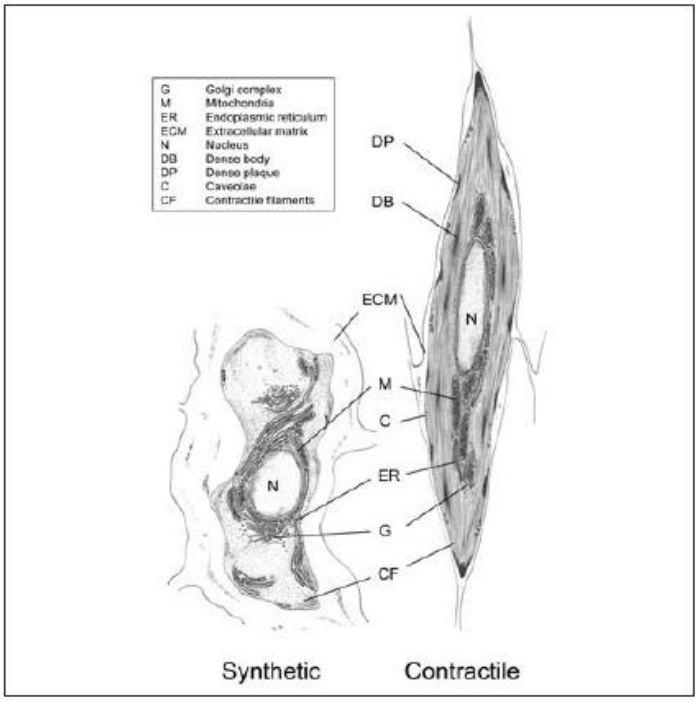

Fig. 4: Ultrastructural characteristics of contractile and synthetic VSMCs.

In the case of vessel damage, VSMCs are able to switch from “normalcontractile” to the ‘proinflammatory-synthetic’ phenotype. This adjustment results in reduction of the expression of markers responsible for VSMCs contraction and in the production of proinflammatory mediators, which trigger proliferation and migration, main processes in the vascular wall repair.

Moreover cytokines, shear stress, reactive oxygen species, and accumulated lipids, which are present in the formation of atherosclerotic plaque, can not only alter VSMCs to proinflammatory phenotype, but also cause abnormal regulation, which leads to additional VSMC de-differentiation and increased extracellular matrix formation, such as collagen, elastin and proteoglycans [3].

This results in the formation of a fibrous cap, a layer of connective tissue that forms an atherosclerotic plaque, which shields the lesion from the lumen. The fibrous cap encloses a lipid-rich necrotic core composed of oxLDLs, cholesterol and apoptotic or necrotic cells that are unable to obtain sufficient nutrients for survival [8].

Atherosclerotic plaques can be classified into two types: stable and vulnerable plaques (Fig. 5).

Stable atherosclerotic plaques are characterized by a thicker layer of fibrous cap, which protects the plaque from rupture.

Vulnerable atherosclerotic plaques are characterized by a lipid core covered by a relatively thin fibrous cap containing less extracellular matrix and vascular smooth muscle cells, often with inflammatory cells and secretion of proteinases. This may lead to rupture or fissure of the surface of the plaque, thus exposing the lipid core to the bloodstream causing thrombosis (local clotting of the blood) and many cardiovascular diseases [8].

An important factor, which can cause disturbances in the stability of atherosclerotic lesions, is also the possible calcification and neovascularization, common features of advanced lesions. Intimal calcification is associated with matrix components secreted by pericyte-like cells, which are subsequently subjected to calcification. This process, similar to bone formation, is regulated by oxysterols and cytokines [3].

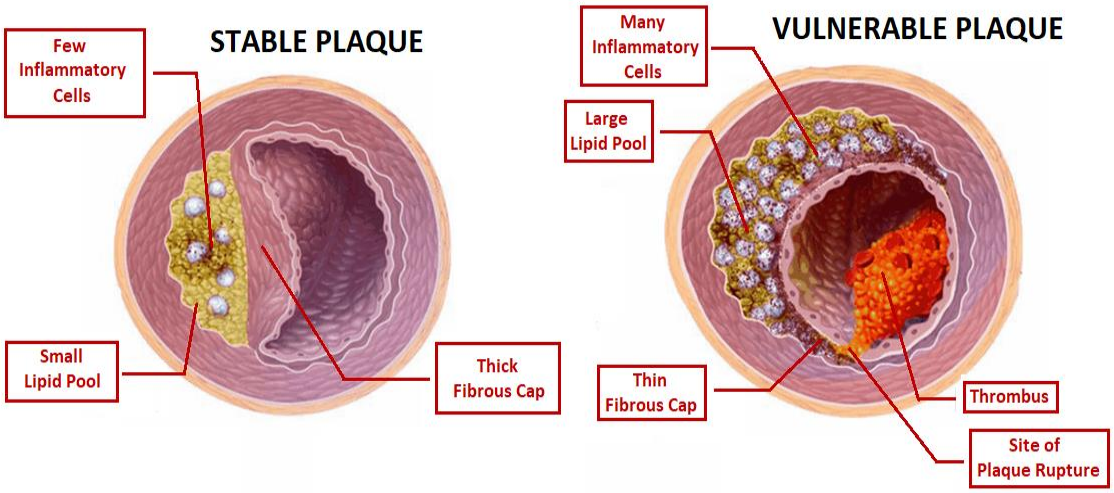

Fig. 5: Stable and vulnerable atherosclerotic plaques.

Angiogenesis is frequent in advanced atherosclerosis. Endothelial proliferation and sprouting usually originates from vasa vasorum in adventitia and extends through media into the base of the plaque, where neovascularization is most conspicuous. The new microvessels are fragile, are leaky, and express cellular adhesion molecules, resulting in local extravasation of plasma proteins, erythrocytes, and inflammatory cells [9].

Thrombosis, the ultimate complication of atherosclerosis, is associated with the eruption of the plaque, which causes blood coagulation components to interact with tissue factors of the plaque, triggering the thrombus that may extend into the vessel lumen, where it will interfere with or block the blood flow.

Furthermore, the thrombus can shear off and block important capillary vessels causing a lack of blood flow and ischemia of cells or important tissues [3].

1.2 Vulnerable plaque

Originally, the term “vulnerable plaque” was specifically used to define a plaque prone to rupture. Although plaque rupture remains a major cause of plaque destabilization, other mechanisms can lead to thrombus formation: plaque erosion and, less frequently, calcified nodules protruding into the artery lumen (Fig. 6) [10].

The plaque prone to rupture is characterized by a large lipid core composed of foam cells, apoptotic and necrotic cells, and debris, and is separated from the lumen by a fibrous cap which is actively weakened by both a lytic process and a lack of repair. This could result in the plaque fissuring at one point, ultimately bringing the platelets in contact with the content of the lipid core.

The so-called "plaque rupture" has been extensively considered by pathologists as the process underlying thrombus formation [10]. The mechanisms of plaque rupture is based on the degradation of the extracellular matrix by MMPs, which are locally overexpressed by the macrophages.

In the weakened plaque the number of macrophages producing MMP is increased and the number of smooth muscle cells repairing the extracellular matrix is decreased. This imbalance between extracellular matrix synthesis and degradation is a solid basis for plaque rupture [10].

Plaque erosion consists in the association of a thrombus with erosion of the endothelial cells at the site of occlusion with a lack of plaque rupture. In contrast with the ruptured plaque, the eroded plaque is rich in smooth muscle cells and proteoglycans, and contains fewer macrophages and T lymphocytes, and fewer calcifications.

Plaque erosion seems to concern a distinct group of patients (young, smokers, females), and there is increasing evidence that vulnerable plaque may not represent a unique disease, but is the result of different causes including plaque rupture and plaque erosion [10].

Apoptosis of the endothelium results in plaque erosion. It is well known that endothelial dysfunction is the initial event of atherogenesis and in part results in loss of nitric oxide (NO) bioavailability. Among the mechanisms of endothelial protection provided by NO are the inhibition of platelet aggregation, of spasm, and particularly of endothelial apoptosis. There is no proof yet that preventing endothelial cell apoptosis would be sufficient to control plaque erosion, and prevention strategies remain to be defined, even if the population at risk is grossly identified.

Like plaque rupture, plaque erosion could be caused by a mechanical process. Indeed, it can be hypothesised that repeated spasm at the same site provoked by smoking may alter endothelial cells, thereby facilitating endothelial detachment from the artery wall.

Moreover, flow turbulence may increase endothelial apoptosis, and facilitate plaque erosion [10].

The least common of all lesions giving rise to acute coronary thrombosis is the calcified nodule, recognized by calcified plates with superimposed calcified bony nodules that result in discontinuity of the fibrous cap, with an irregular luminal surface devoid of endothelial cells and overlying luminal thrombus [11]. Plaque calcification is associated with coronary thrombosis in the absence of eroded or ruptured plaque, although more rarely. The calcified nodules protrude into the lumen and are not associated with the lipid core [10].

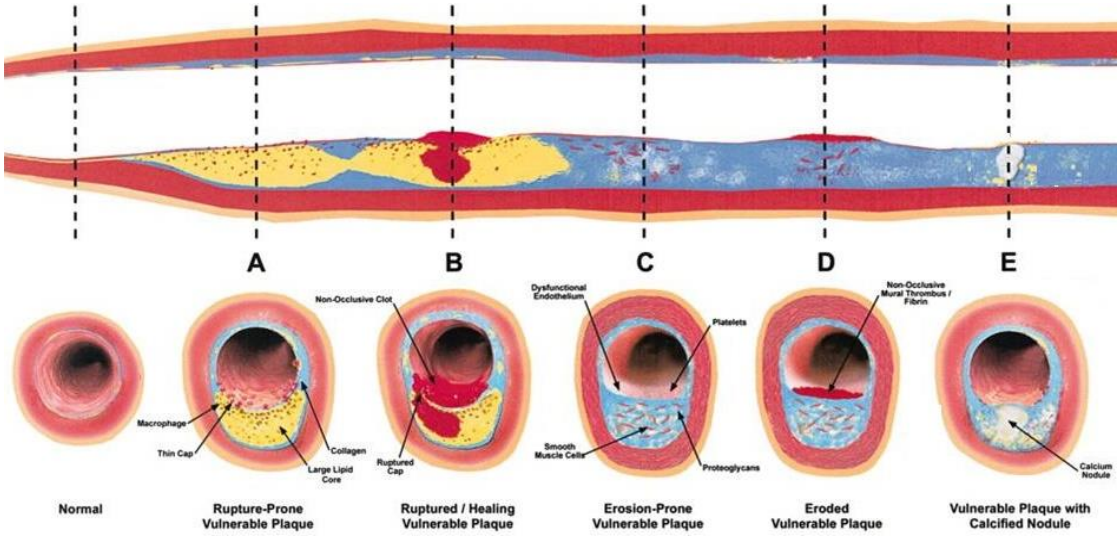

Fig. 6: Different types of vulnerable plaques. A) Rupture-prone plaque containing large lipid core with thin fibrous cap and infiltrated by macrophages. B) Plaque that has ruptured with subocclusive thrombus and early organization. C) Erosion-prone plaque with proteoglycan matrix in a smooth muscle cell rich plaque. D) Plaque that has ruptured with subocclusive thrombus. E) Calcific nodule protruding into the vessel lumen.

1.3 Imaging of atherosclerosis

Invasive and non-invasive techniques

Atherosclerosis is the most common form of vascular disease and constitutes the major cause of death, with 17.5 million related deaths annually (31% of global mortality) [12]. Atherosclerosis begins in childhood, as an accumulation of fatty streaks-lipid-engorged macrophages and T lymphocytes in the intima of the arteries.

During a life-time, most atherosclerotic plaques remain asymptomatic (sub-clinical disease), some become obstructive and might cause symptoms because of impaired maximal blood flow (stable angina, intermittent claudication, or mesenteric ischaemia are examples), and a small percentage, in some individuals, become thrombosis-prone (vulnerable) and lead to atherothrombotic events such as acute coronary syndromes (ACS), stroke, critical limb ischemia and sudden death [13,14].

Despite recent advances in medical and interventional percutaneous or surgical therapies, coronary artery disease (CAD) continues to be a major cause of morbidity and mortality throughout the world.

Modern cardiology is focused on developing techniques designed to restore blood flow in arteries possessing hemodynamically significant lesions causing cardiac ischemia and infarction. This reactive strategy, however, does little to prevent future coronary events. Although pharmacotherapy with agents such as aspirin and statins has proved to lower the risk of future coronary events, it does not represent an effective solution [11].

Prevention – rather than treatment – of acute events seems to be the only effective strategy to reduce the epidemiological burden of cardiovascular disease (CVD) and significantly improve mortality and morbidity [15].

Anatomic imaging modalities, such as X-ray contrast angiography, can detect the severity of coronary luminal stenosis and carotid intima-media thickening, and can guide interventions such as surgical coronary revascularization and primary percutaneous coronary intervention (PPCI) [16].

Although coronary angiography is still the gold standard for the assessment of CAD, it simply shows the coronary lumen, and is unable to address plaque vulnerability or provide information on the extent and severity of atherosclerosis. This approach can relieve ischemia but only prevents events or prolongs life in selected subsets of patients.

Indeed, autopsy studies show that most fatal myocardial infarctions (MI) are due to atherosclerotic lesions that do not cause flow-limiting stenosis and therefore would not be detectable using standard X-ray angiography [16,17].

Efforts have been done in the past few years to overcome such limitations of angiography by developing invasive imaging modalities capable of imaging coronary atherosclerosis and of providing a better understanding of coronary pathology [15].

These techniques currently employ IVUS, OCT and NIR spectroscopy.

Intravascular ultrasound (IVUS) is one of the most widely used invasive coronary atherosclerotic plaque imaging modalities. It provides real-time, high resolution, tomographic images of the lumen, as well as atherosclerotic changes in the vessel wall. This imaging technique requires a selective investigation of the vessel with an imaging catheter that incorporates a transducer emitting high-frequency (20–45 MHz) ultrasounds. Detection of the contours of the lumen and of the media–adventitia interface permits a direct measurement of the lumen and of the total cross-sectional vessel area, and therefore allows calculation of the absolute and percent plaque area. In addition, morphology, severity, and composition of coronary atherosclerotic plaques can be determined [15].

Gray-scale IVUS has limited ability to differentiate individual plaque components, but spectral analysis of the backscattered radiofrequency data with, for example, virtual histology (VH)-IVUS can be used to detect necrotic core, dense calcium, fibrous, and fibrofatty plaques with reasonable accuracy. However, because of increased noise and artefacts, image interpretation can be difficult; furthermore, IVUS has insufficient spatial resolution to reliably and reproducibly detect thin fibrous cap [18].

Optical coherence tomography (OCT) is the second major coronary plaque invasive imaging modality. It is based on infrared light and is able to study atherosclerotic plaques and stented segments with extreme spatial accuracy. The light reflected from plaque structures provides image data whereas the background effect of scattered light is negated through the use of interferometric techniques. Bright or dark areas occur as a result of constructive or destructive interference between reflected and reference beams. Given the much smaller wavelength of light in comparison to ultrasound, OCT allows for proper visualization of fibrous caps, collagen content (polarization-sensitive OCT), macrophages (related to inflammation), neovessels (appearing as microchannels), ruptures, and thrombi [12].

OCT has a resolution much higher than IVUS (10–15 μm versus 100–150 μm), but its limited tissue penetration (1–3 mm) makes the assessment of vessel dimensions and of the overall plaque volume impossible [15,18].

Another invasive imaging modality is Near Infrared Spectroscopy (NIR), which allows to determine the chemical composition of the artery wall *in vivo*, and potentially to detect lipid-rich atheroma. NIRS utilizes characteristic emission spectra produced by plaque contents when interacting with photons (wavelength area, 700–2500 nm).

The NIRS system, consisting of a pullback and rotation device, a console and a catheter, utilizes changes in the reflection of emitted light to map the vessel wall in the form of a chemogram, where yellow regions are those with a higher probability of the presence of a lipid pool, while red regions have a lower probability.

The chemogram enables the measurement of the lipid core burden index (LCBI), as the fraction of yellow pixels within a region; culprit lesions are associated with significantly higher LCBI than non-culprit segments [15].

Although NIRS can identify lipid content underlying high-risk plaques in human arteries through the blood, its major limitation is that it does not provide any structural information on the plaque. This limitation can, in part, be overcome by NIRS–IVUS hybrid imaging, although this hybrid catheter still cannot robustly assess cap thickness [18].

IVUS and OCT may play a key role in interventional cardiology, but their utilization for the identification of vulnerable plaques usually makes barely 1% in daily clinical practice and their application is limited by their invasive nature [13].

Non-invasive imaging techniques include: ultrasounds (US), electron beam computed tomography (EBCT), multi-detector CT (MDCT), magnetic resonance imaging (MRI) and nuclear imaging, including single photon emission computed tomography (SPECT) and positron emission tomography (PET).

Non-invasive ultrasound imaging represents a safe, fast, and comparatively cheap method of assessing atherosclerosis, although its use is largely confined to the carotid and peripheral vasculature. Even before the development of significant atherosclerosis, the high temporal and spatial resolution of carotid ultrasound allows accurate measurement of the distance from the luminal surface to the intima-media boundary, termed carotid

intima-media thickness (CIMT). Prospective data have shown that CIMT correlates with cardiovascular risk, even in asymptomatic individuals [14].

Ultrasound remains limited in its ability to distinguish plaque constituents and morphology. More recent developments could overcome this limitation. Delayed imaging using microbubble contrast agents (contrast-enhanced ultrasound) can demonstrate, for example, the degree of inflammation and neovascularization in the arterial wall. Furthermore, such agents can be conjugated with ligands that target specific pathological processes (e.g. the expression of VCAM-1 on surface endothelium), thus offering the possibility of molecular imaging using currently available ultrasound technology [14].

The rationale behind the use of EBCT is in the assumption that coronary artery calcium (CAC) detected by CT may correlate with plaque burden. Because medial calcification is rare in normal coronary arteries, CAC could reflect coronary atherosclerosis [13]. Coronary artery calcium score (CACS) is a parameter that allows a better stratification of asymptomatic subjects classified in the uncertain category of intermediate risk for future events by the traditional clinical risk score.

However, coronary calcium fails to detect non-calcified plaques, which are considered more prone to complication and adverse events than calcified plaques [15].

MDCT-coronary angiography (MDCT-CA) utilizes a multi-detector CT scanner in combination with iodine intravenous dye to visualize the coronary arteries. Significant advantages stem from its very nature: noninvasiveness, ability for imaging the whole coronary vasculature, and potential for assessing both vessel wall in addition to the lumen. MDCT-CA is currently the only non-invasive diagnostic modality capable of imaging the coronary wall, of evaluating and quantifying the plaque, and of effectively monitoring the progression and/or regression of atherosclerosis following statin therapy [15].

From a clinical perspective, the most important advantage of MDCT-CA is the high negative predictive value that allows to exclude the presence of disease in intermediate high risk patients. Nevertheless, considering current radiation exposure data, the use of CT angiography as a screening modality for asymptomatic patients is unjustified [13].

MRI has been extensively validated for the detection and characterization of atherosclerotic plaques, and the monitoring of their possible change under pharmacological treatment [15]. MRI differentiates plaque components on the basis of

biophysical and biochemical properties such as chemical composition, water content, physical state, molecular motion, or diffusion.

Magnetic resonance coronary angiography (MRCA) is a promising technology for the imaging of vulnerable plaques, but its application has always been limited to larger arteries (aorta and carotid arteries) due to its low spatial resolution. Major strengths of MR are the capability to visualize both the lumen and the wall of large vessels, the absence of radiation exposure – ensuring serial repeatability – and the excellent contrast resolution, useful to evaluate compositional and morphological features of atherosclerotic plaques [15].

The use of Gadolinium (Gd) contrast agents can improve the detection and quantification of the lipid core, and in particular the presence of a thin fibrous cap. Direct comparison of endarterectomy specimens with MRI findings suggested that Gd retention primarily occurs in regions with thin fibrous caps (<60 μm). As a thin fibrous cap characterizes a plaque that has ruptured, this finding may have clinical relevance. The underlying mechanism of enhanced Gd uptake in atherosclerotic plaques may relate to inflammation and/or endothelial dysfunction or fibrosis [13].

A promising approach for imaging plaque macrophages involves the intravenous injection of ultra-small super-paramagnetic iron oxide nanoparticles.

The capability of MR to detect the presence of macrophages in the context of atherosclerotic plaques by using the ultra-small particles of iron oxide might play a significant role in the detection and characterization of human vulnerable plaques, and be used in the serial assessment of the effects of statin therapy, but such imaging modality has been so far limited to human carotid plaques, devoid of motion artifacts [15].

Nuclear imaging, with SPECT and PET, can assess perfusion and tissue metabolic activity, providing functional information on plaque activity and potentially assessing plaque stability.

Currently, new hardware designs combining nuclear imaging techniques with others with better spatial resolution, such as SPECT–CT, PET-CT, and PET-MR dual-modality systems, and dedicated cardiac gamma cameras with optimal detector geometric arrays, linear count statistics and count rate response, allow for lower-radiation imaging, reduced scan time and improved image quality. The high sensitivity of both SPECT and PET nuclear imaging techniques, together with the ability of CT to identify the anatomical

burden of CAD, hold the promise to increase the low positive value of CT imaging alone, distinguishing vulnerable from stable plaques [15].

Metastable Technetium-99 (^{99m}Tc), which represents nearly 80% of all nuclear medicine procedures, and Indium-111 (^{111}In) have been widely used in SPECT imaging of atherosclerotic lesions [19]. ^{99m}Tc radiotracers – such as ^{99m}Tc-sestamibi and ^{99m}Tc-tetrofosmin – are widely used in clinical practice for the investigation of myocardial perfusion and viability. However, despite initial promising results for the identification of vulnerable atherosclerotic plaques, most current studies using integrated SPECT/CT focus on myocardial perfusion imaging, while plaque imaging is still limited because of resolution limits and insufficient specificity of the tracer.

PET imaging may also be a powerful tool to detect vulnerable plaques. PET imaging has several technical advantages over SPECT, including a better spatial resolution. Therefore, with the dual PET-CT systems, investigation of both morphology and activity of the plaque could be easier to achieve.

^{18}F-fluorodeoxyglucose (^{18}F-FDG) is the mainstay radioligand in PET imaging and consequently has been the most common radioligand used in imaging studies of atherosclerosis. ^{18}F-FDG is a radionucleotide analogue of glucose that accumulates intracellularly in proportion to cellular demand for glucose. It is taken up into cells via facilitated glucose transporter member (GLUT) 1 and 3, which are upregulated during atherogenesis due to hypoxia within the atheroma core, and once inside the cytoplasm undergoes phosphorylation by hexokinase to become ^{18}F-FDG-6-phosphate.

^{18}F-FDG-6-phosphate lacks a 2′ hydroxyl group and consequently is unable to enter the Krebs cycle and undergo glycolysis, subsequently diffusing slowly out of the cell. This resulting accumulation is readily quantifiable and can be used as a sensitive measure of metabolic activity, particularly given its very high signal-to-noise ratios in tissues without high metabolic activity (such as normal vessel wall and blood) [20].

^{18}F-FDG has shown to accumulate in macrophage-rich atherosclerotic plaques. Macrophages are dependent on external glucose for their metabolism because they are unable to store glycogen and have a glycolytic activity 5- to 20-fold higher than background tissues, increasing up to 50-fold when activated [15].

However, recent *in vitro* studies suggest that FDG accumulation may reflect hypoxia-stimulated macrophages rather than inflammation [16].

1.4 VCAM-1 and diagnostic imaging: state of the art

Endothelial activation is a key event in early atherogenesis, characterised by the up-regulation of adhesion molecules, vascular cell adhesion molecule-1 (VCAM-1), intercellular adhesion molecule-1 (ICAM-1), P- and E-selectin, promoting monocyte recruitment to the vascular wall and subsequent lesion development.

Initial monocyte rolling along activated endothelium is mediated by P-selectin and its interaction with integrin P-selectin glycoprotein ligand-1 (PSGL-1) expressed on monocytes, while firm adhesion of monocytes is mediated by VCAM-1 (CD106) and engagement of the integrin very late antigen-4, VLA-4 (also known as α4β1 integrin) expressed on monocytes [16].

VCAM-1 is an immunoglobulin(Ig)–like transmembrane adhesion molecule, highly conserved in evolution, and participates in a variety of cellular functions in health and disease. Human VCAM-1 has 2 isoforms, the predominant 7 Ig-domain isoforms and a minor, alternatively spliced isoform with 6 Ig domains, whereas in mice the second isoform consists of the first 3 domains attached to the cell membrane through a glycosylphosphatidylinositol (GPI) anchor.

VCAM-1 is minimally expressed on most resting vascular endothelial cells and is inducible in many tissue vascular beds following injury or stress. Because of this activation, VCAM-1 has been implicated in the pathophysiology of certain autoimmune diseases, atherosclerosis, and allograft rejection.

VCAM-1 is constitutively expressed in bone marrow stromal/endothelial cells and certain classes of hematopoietic cells (B cells, follicular dendritic cells, and macrophages).

Its major ligand is the integrin VLA-4, with binding sites located in the first and fourth Ig domains, whereas other ligands bind with less affinity and include α4β7, α9β1 and $\alpha_D\beta2$ [21].

VCAM-1 is a promising marker for molecular imaging of vascular inflammation in atherosclerosis, since it is not constitutively expressed in normal vessels but is rapidly up-regulated on vascular endothelial cells in both early and advanced lesions and is readily accessible to blood-borne, targeted contrast agents. VCAM-1 is also up-regulated by macrophages and smooth muscle cells in atherosclerotic plaques [16].

For molecular imaging of vascular inflammation, Tsourkas et al. conjugated cross-linked dextran-coated iron oxide (CLIO) nanoparticles, labeled with the near-infrared fluorochrome Cy5.5, with an anti-VCAM-1 antibody [22]. The VCAM-1-targeted nanoparticles could detect VCAM-1 expression on the endothelial cells by magnetic resonance and optical imaging.

Besides antibodies, different VCAM-1-targeting peptides have been selected using the phage display or other approaches [23,24]. VHSPNKK-modified magnetofluorescent nanoparticles (VNP) had 12-fold higher binding affinity to VCAM-1 than VCAM-1 monoclonal antibodies and, importantly, had low binding affinity to macrophages [23]. The same research group identified another peptide, VHPKQHR, that had a sequence homology to VLA-4, the natural ligand of VCAM-1, and a binding affinity of 33.7 ± 8 nM [24,25]. It was conjugated to magnetofluorescent nanoparticles through a GGSK(FITC)C linker (VINP-28). *In vitro* experiments revealed a 20-fold higher cellular binding and internalization of VINP-28 by VCAM-1-expressing cells than the previous nanoparticles. VINP-28 had high binding affinity to endothelial cells, but low binding affinity to macrophages and smooth muscle cells, and was also able to detect endothelial cells and other VCAM-1 expressing cells in resected human carotid artery lesions *ex vivo* [24].

The same peptide sequence has been utilized by Nahrendorf et al. to develop a VCAM-1 targeting peptide-based radiotracer, called ^{18}F-4V, which is internalised by endothelial cells and can detect VCAM-1 expression in murine atherosclerotic plaques by *in vivo* hybrid PET–CT [26].

A SPECT radiotracer has been also developed, in which the residue 75–84 (B2702-p) of the major histocompatibility complex-1 (MHC-1) molecule B2702 was radiolabeled with ^{99m}Tc, for *in vivo* molecular imaging of VCAM-1 expression in atherosclerotic plaques [27].

Recently, nanobodies recognising both human and mouse VCAM-1 have been investigated as potential targeting ligands for SPECT. Nanobodies are single-domain antibody fragments that occur naturally in sharks and camelids. Using non-invasive SPECT–CT imaging, ^{99m}Tc-radiolabeled VCAM-1 nanobodies enabled *in vivo* detection of VCAM-1 expression in aortic arch atherosclerosis in apolipoprotein E deficient (apoE$^{-/-}$) mice [28].

1.5 Aims and objectives

Atherosclerosis develops over decades and is often silent until an acute event occurs in later life. Despite huge efforts of research on both diagnosis and therapy, atherosclerosis-related cardiovascular disease (CVD) remains one of the leading causes of mortality.

The most effective way of preventing and intervening CVD is to be able to diagnose first signs of CVD.

Vascular cell adhesion molecule-1 (VCAM-1) plays a cardinal role in atherosclerotic plaque progression. The early induction, confinement of expression to atherosclerotic lesions, and accessible position in proximity to the blood pool render VCAM-1 an attractive imaging biomarker.

Therefore, my PhD project aimed to develop a diagnostic system to reveal early atherosclerotic lesions, using VCAM-1 as target.

In order to exploit this marker, it was planned to conjugate a well-characterized peptide mentioned above, [24,25,26] that shows high affinity for VCAM-1 with a radiopharmaceutical, detectable by PET.

Two different molecules have been synthesized.

The first one, named NAMP, is a derivative of biotin conjugated with the VCAM-1 binding peptide through a linker. After binding a molecule of avidin, NAMP can be traced using a biotin derivative carrying two macrocycles complexing radionuclides (BisDOTA).

The second molecule, named MacroP, is a derivative of the chelating agent DOTA directly conjugated with the VCAM-1 biding peptide.

The idea was to compare these two diagnostic systems, in order to identify which had the best properties for the detection of early atherosclerotic lesions.

2.CHAPTER 1

Synthesis and characterization of NAMP

INTRODUCTION

Radiolabeled derivatives of biotin are being developed for application to "pretargeting" usually employed in tumor therapy with radiolabeled monoclonal antibodies (MoAbs) [29-32].

The concept of pretargeting has been exploited in attempt to overcome the low uptake of MoAbs by the tumor and improve the tumor-to-blood ratio [29].

The strategy is based on the separate administration of a modified monoclonal antibody that permits a second radiolabeled component to bind specifically to it [30]. Conceptually, the modified MoAb is injected first and allowed to distribute throughout the body, to bind the cells expressing the antigen and to clear substantially from the other tissues. Then, the radiolabeled second component is administered and, ideally, it localises at sites where the modified MoAb has accumulated. If the second component has higher permeation, clearance and diffusion rates than those of the MoAb, more rapid radionuclide localisation to the tumor and higher tumor selectivity are possible, thus resulting in higher tumor to non-tumor ratios [29].

The extraordinary affinity of avidin for biotin ($K_a = 10^{15}\ M^{-1}$) is the strongest known non-covalent interaction of a protein and ligand. This specific binding and their fast blood clearance make the avidin–biotin system applicable for pretargeting [30].

Briefly, avidin is a 66-kDa glycoprotein found in egg white, made of four identical subunits, each bearing a single binding site for biotin. One mole of protein can therefore bind up to four moles of biotin [29].

Strong hydrogen bonding interactions within the binding site of biotin due to the presence of the ureido group, and its polarization owing to charged aspartate results in remarkable avidity in the femtomolar range. This high affinity of biotin for avidin and fast blood clearance gives the advantage of better tumor to non-tumor ratio over conventionally used radiolabeled monoclonal antibodies and long peptides which have slow blood clearance and moderate tumor to muscle ratio.

This makes the avidin−biotin system an ideal method for delivering diagnostic or therapeutic radionuclides to cancer cells [33].

An important property for radiolabeled biotin derivatives used *in vivo* for pretargeting, must be the stability towards degradation by the enzyme biotinidase. Biotinidase is present in serum and tissues of animals and humans in nanomolar concentrations. A primary function of this enzyme is to cleave the biotinamide bond linking biotin (vitamin H) and lysine in biocytin, so that the essential vitamin can be recycled. Biocytin is released after peptidase degradation of carboxylase enzymes containing biotin (Fig. 7). In order to block the biotinamide cleaving action of biotinidase, many biotin derivatives have been developed [34, 35, 36].

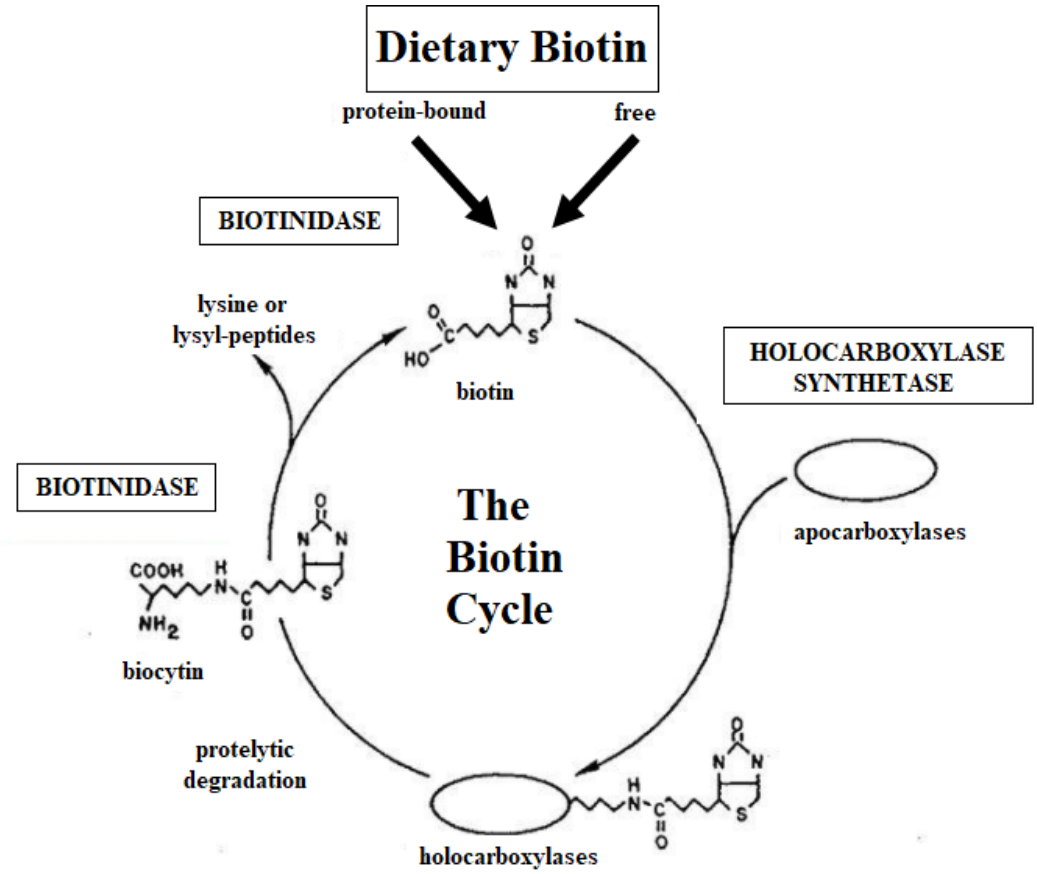

Fig. 7: Scheme of the biotin cycle.

The structural elements of biotin involved in binding with avidin are the urea moiety and the nonoxidized thioether, thus leaving the carboxylic group available for modification. For this reason, radiolabeled biotin derivatives generally have been prepared by direct functionalization, generally with an amide, of the carboxyl group of the vitamin [36].

Wilbur and colleagues [37-40] published a series of articles describing modifications of this amide bond by introducing close steric hindrance to stabilize it.
Szalecki [35] synthesized norbiotinamine, a biotin derivative with a terminal amino group in place of the carboxylic acid and developed its derivatives.
Norbiotinamine is an interesting compound because it is exploitable for conjugation reactions with the carboxylic group of aminoacids or other molecules used for targeting and the resulting reversed amide bond is stable to biotinidase cleavage [36].

During my PhD, NAMP was the first molecule to be synthesized. It is a norbiotinamine conjugated with a VCAM-1 binding peptide, through a linker (Fig. 8).

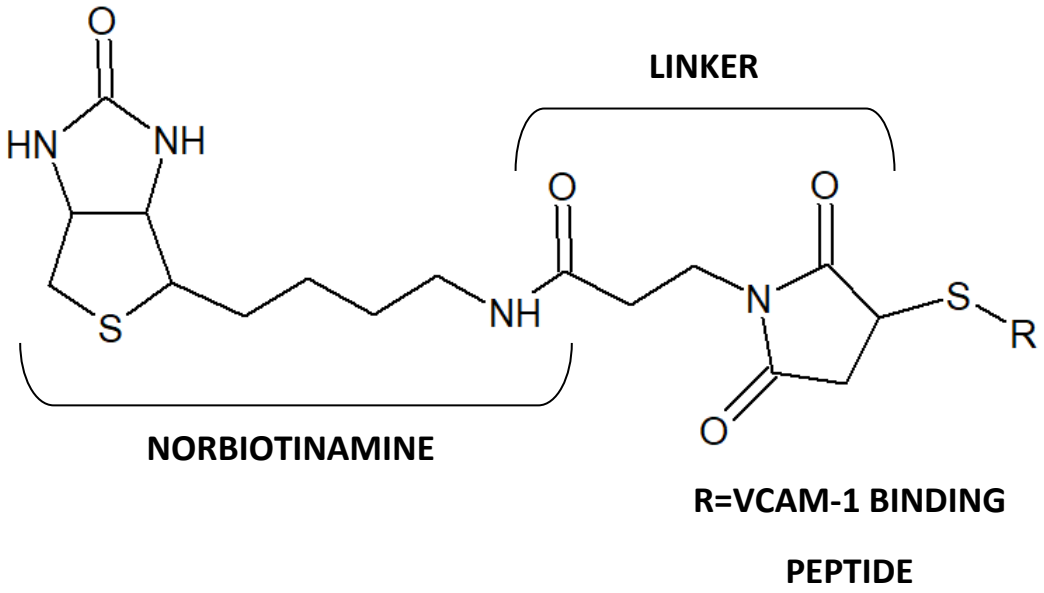

Fig. 8: Structure of NAMP.

In order to link the amine derivative of biotin with the thiol group of a cysteine within the VCAM-1 binding peptide, an activated linker, N-hydroxysuccinimidyl-3-maleimido propionic acid (ASAM), has been synthesized. This linker has a carboxylic group, activated by N-hydroxysuccinimide, able to bind the amino group of norbiotinamine, and a maleimide group that can react selectively with the thiol group in the peptide (Fig. 9).

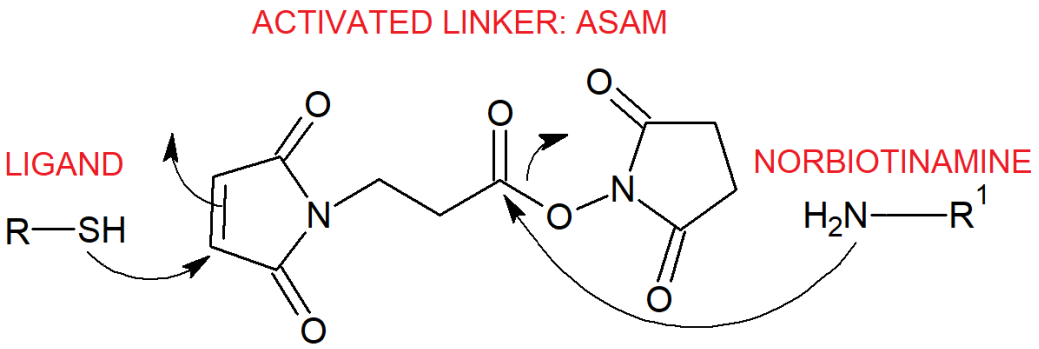

Fig. 9: Scheme of the reaction between norbiotinamine and the thiol group of the ligand through the linker.

This chapter reports: the synthesis and characterization of ASAM; the conversion of biotin into norbiotinamine and the characterization of the synthetic intermediate, N-Boc norbiotinamine; the reaction between ASAM and norbiotinamine, to form N-norbiotinyl-β-maleimidopropionylamide (NAM) and its characterization; finally, the reaction between NAM and the VCAM-1 binding peptide (Fig. 10).

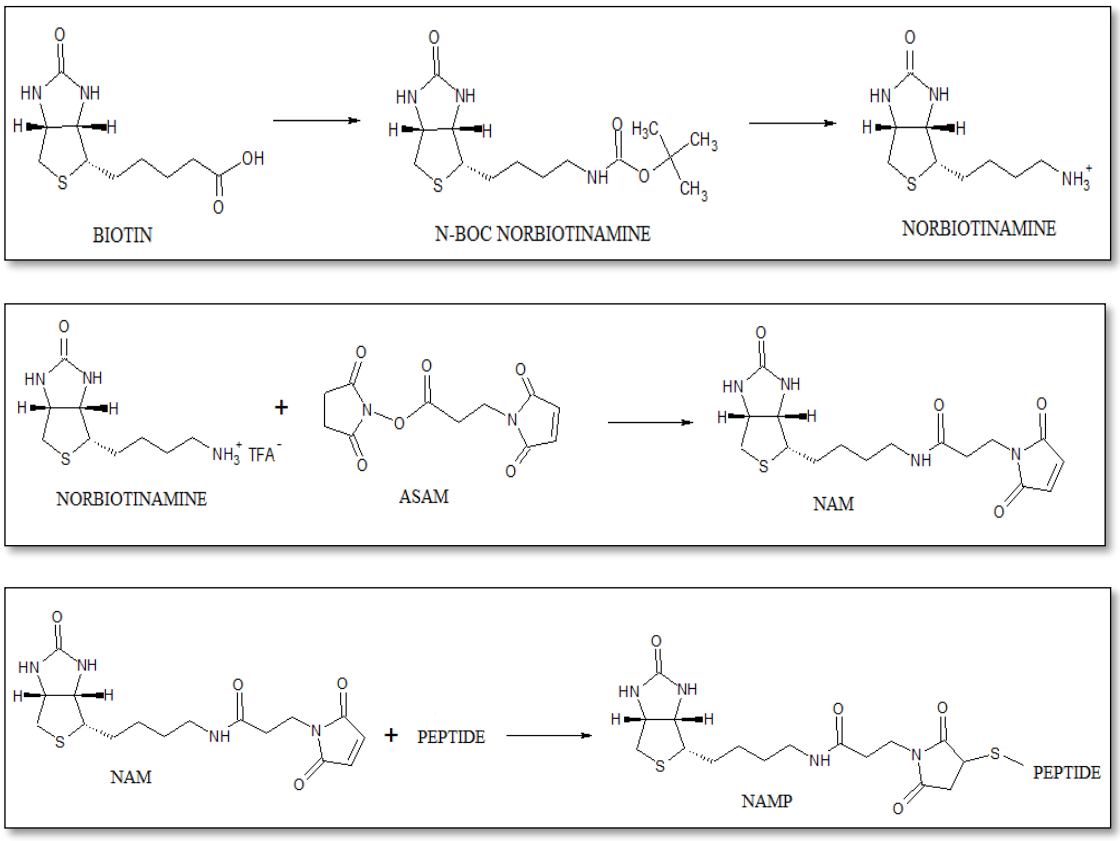

Fig. 10: Main reaction steps to produce NAMP.

MATERIALS AND METHODS

Materials

Acetic acid glacial 100% (AcOH) (Merck); aluminium sheet silica gel 60 F254 plates (Merk); β-alanine 98% (Alfa Aesar); biotin (Amresco); diphenylphosphorylazide (DPPA) (Alfa Aesar); maleic anhydride 98+% (Alfa Aesar); N-hydroxysuccinimide 98+% (Alfa Aesar); N,N'-dicyclohexylcarbodiimide 99% (DCC) (Alfa Aesar); N,N'-dimethylformamide for peptide synthesis (DMF) (Merk); tert-butanol (t-BuOH) (Alfa Aesar); triethylamine (TEA) (Sigma Aldrich); trifluoroacetic acid (TFA) (Merck); tris-(2-carboxyethyl)phosphine hydrochloride (TCEP-HCl) (Sigma-Aldrich); VCAM-1 binding peptide (Innovagen). All chemicals were used as received, without further purification. The water used was purified with a Milli-Q system (Millipore).

Instruments

ALC PK 120 centrifuge; Bruker Avance DPX 300 NMR spectrometer; Buchi Rotavapor RE128; Camag Linomat 5 and TLC scanner 3; De Lama SteriPlus bench steam sterilizer; EchoTherm™ SC25XT Torrey-Pines Scientific orbital mixing dry bath Hewlett Packard HP 8453 UV-Vis spectrophotometer; Hewlett Packard Series II 1090 liquid chromatograph; LTQ Orbitrap Velos Pro; Mettler Toledo Quattro MP220 Basic pHmeter; Mettler Toledo XS3DU electronic microbalance; Nikon Alphaphot-2 YS2 microscope, provided with a Mettler Toledo FP82HT electrical furnace, controlled by a Mettler Toledo FP90 central processor; Perkin Elmer DSC 7; Perkin Elmer Sample Pan Aluminium 6.7 mm 900786.901/0219-0041; Perkin Elmer 2000 FT-IR System; Scaltec SBC 21, electronic analytical balance; Thermo Fisher Scientific FLASH 2000 OEA CHNS/O + MAS200R- SN 2015.F0227; Waters 1525 binary pump HPLC; Waters 2992 photodiode array detector; Waters fraction collector III.

Methods

Synthesis of N-hydroxysuccinimidyl-3-maleimido propionic acid (ASAM)

This product was prepared as described by Hong Y. Song et al. [41].

β-alanine (22.4 mmol) and a solution of maleic anhydride (22.4 mmol) in 25 mL of DMF were mixed and stirred at room temperature up to complete dissolution.

To the resulting solution, cooled to 0°C in an ice bath, N-hydroxysuccinimide (28 mmol) was added, followed by DCC (47.7 mmol), and the mixture was stirred o/n at room temperature.

The precipitated N,N'-dicyclohexylurea (DCU), formed during the reaction, was removed by centrifugation at 2170 rpm for 10 minutes, followed by paper filtration.

The filtrate was poured in ice to obtain the product as a white precipitate.

After centrifugation at 2170 rpm for 10 minutes and Buchner filtration, the solid was washed with water and dried under vacuum. The yield obtained was 54% w/w.

Synthesis of N-(tert-butoxycarbonyl)-norbiotinamine (NBA-BOC)

In a flask, 500 mg of biotin (2.05 mmol) were dissolved in 37.5 mL of DMF, at room temperature. After complete dissolution, 620 µL of TEA (4.4 mmol) were added and stirred at room temperature for 10 minutes, followed by the addition of 620 µL of DPPA (2.9 mmol). After stirring at room temperature for 30 minutes, 90 mL of t-BuOH were added. Gradual heating (20°C/h) was carried out up to 90°C and the reaction was refluxed for 24h. After purification in semi-preparative RP-HPLC and drying by Rotavapor, NBA-BOC was obtained as a flocculated solid with a yield of 50% w/w.

Synthesis of norbiotinamine (NBA)

NBA-BOC was hydrolyzed to NBA with TFA:dichloromethane 1:1, at 0°C for 2h. Solvents were removed with Rotavapor and the obtained product was utilized for the next reaction without further purification.

Synthesis of N-norbiotinyl-β-maleimidopropionylamide (NAM)

NBA (about 0.15 mmol) and TEA (0.15 mmol) were dissolved in 25 mL of acetonitrile, by sonication. 0.24 mmol of ASAM were added to the dispersion, and the reaction mixture was stirred in glycerine bath at 80°C for 24h, under reflux. The product was collected by precipitation at -20°C after 48h and obtained pure after four washings with diethylether. The yield obtained was 60 % w/w.

Synthesis of NAMP

A stock solution of NAM was prepared by dissolving 0.6 mg of NAM in 1.5 mL of ultrapure water, in a 1.5 mL polypropylene tube. The peptide solution was prepared by solubilising 1 mg in 500 µL of ultrapure water. 1.05 mL of NAM stock solution (1.3 µmol) and 450 µL of peptide solution (0.65 µmol) were mixed in a 1.5 mL polypropylene tube, and heated at 37°C, under orbital shaking at 400 rpm for 24h, under nitrogen.

Sterilization of reaction materials

The sterilization of the materials used for the reactions of NAMP was performed in autoclave at 120°C under saturated steam pressure of 98 kPa over atmospheric pressure, for 30 minutes.

Thermal analysis

The thermal analyses of ASAM and NBA-BOC were performed by differential scanning calorimetry (DSC).

For ASAM, carefully weighted samples of approx. 3.5 mg were subjected to a thermal gradient of 10°C/min under nitrogen flow, in a covered but not crimped aluminium pan. The scanning was carried out from 30°C to 185° C.

For NBA-BOC, carefully weighted samples of approx. 2 mg in a covered but not crimped aluminium pan were heated under nitrogen flow from 40°C to 200°C at 10°C/min.

The DSC thermal analyses were supported by hot stage microscopy analysis, performed at the same conditions.

Infrared analysis (IR analysis)

IR spectra were collected on a Perkin Elmer 2000 FT-IR spectrometer from samples prepared as KBr pellets.

NMR analysis

NMR spectra were recorded on a Bruker Avance DPX 300 spectrometer at 300 MHz. Coupling constants (J) are expressed in Hertz; chemical shifts (δ) are reported in parts per million (ppm) relative to tetramethylsilane (TMS). The following abbreviations are used to explain the multiplicities: s = singlet, d = doublet, dd = doublet of doublets, t = triplet, m = multiplet.

^{1}H- and ^{13}C-NMR spectra of ASAM and NBA-BOC were recorded in $CDCl_3$; ^{1}H-NMR spectrum of NAM and ^{13}C-NMR spectrum of NBA I2a in DMSO-d_6.

Thin-layer chromatography (TLC)

Thin-layer chromatography was carried out on TLC aluminum sheet silica gel 60 F_{254}, 8x12 cm, layer thickness 0.2 mm, without activation. Sample and standard solutions were deposited by means of Linomat 5, using the following settings: band length 3 mm, distance from left plate edge 14 mm and from the lower plate edge 15 mm.

The sample application volumes were 5 µL for 5 mg/mL standard solutions of β–alanine in ultrapure water, maleic anhydride and N-hydroxysuccinimide in methanol and 5 µL for 5 mg/mL sample solution in dichloromethane. Considering one blank track for detector calibration, 5 tracks for plate were deposited. Chromatography was performed in a 20 cm × 10 cm twin trough chamber (CAMAG) up to a migration distance of 95 mm (from the lower plate edge) using ethyl acetate/methanol 85:15 (v/v) as mobile phase. Then, the plate was dried for 5 minutes in a stream of warm air.

The detection was performed by TLC Scanner 3 with a slit dimension of 3mm × 0.45mm, a scanning speed of 20 mm/s and a data resolution of 100 µm / step.

In UV-absorbance mode, standards and sample were measured at 216 nm wavelength. All instruments were controlled via the software platform winCats 1.4.1 Planar Chromatography Manager (CAMAG).

Analytical reversed-phase high-performance liquid chromatography (Analytical RP-HPLC)

Analytical RP-HPLC was performed on Hewlett Packard Series II 1090 with a UV-visible detector.

The analysis of HPLC data was conducted on Hewlett-Packard HPLC ChemStation software. Reverse-phase HPLC chromatography was carried out using a RP 18, Waters X-Bridge C18, 3.5 µm, 4.6 x 150 mm and a Waters X-Bridge BEH C18 Sentry Guard Cartridge 3.5 µm, 4.6 x 20 mm.

Analysis of ASAM, NBA-BOC and NBA

For the determination of ASAM, NBA-BOC and NBA purity, a RP- HPLC method was performed using a gradient solvent system at a flow rate of 1 mL/min. The gradient mixture was composed of 0.1% aqueous AcOH (solvent A) and methanol gradient grade (solvent B). Gradient elution: 0-2 min 40% B; 2-12 min linear gradient from 40% to 100% B; 12-16 min 100% B. Post run to 40% B: 3 min.

The chromatograms were acquired at 200, 254 and 340 nm wavelengths.

The injection volume was 10 µL. ASAM was dissolved in methanol; the other analytes were dissolved in the mobile phase.

Analysis of NAM

The analysis of the reaction mixture and the determination of NAM purity were carried out by performing two different RP-HPLC methods:

Method H-NAM1: it was performed using a gradient solvent system at a flow rate of 1 mL/min.

The gradient mixture was composed of 0.1% aqueous AcOH (solvent A) and methanol gradient grade (solvent B). Gradient elution: 0-2 min 40% B; 2-7 min linear gradient from 40% to 100% B; 7-11 min 100% B. Post run to 40% B: 3 min. The chromatograms were acquired at 200, 254 and 340 nm wavelengths. The injection volume was 10 µL and the solutions were prepared using the mobile phase as solvent.

Method H-NAM2: it was performed using a gradient solvent system at a flow rate of 1 mL/min.

The gradient mixture was composed of ultrapure water (solvent A) and acetonitrile gradient grade (solvent B). Linear gradient from 20% to 100% B in 10 min. Post run to 20% B: 3 min. The chromatograms were acquired at 200, 254 and 340 nm wavelengths. The injection volume was 10 µL and the mobile phase was used as solvent.

Analysis of NAMP

For the analysis of the reaction mixture and the determination of NAMP purity, two RP-HPLC methods were performed, using a mobile phase composed by 0.1% aqueous TFA (solvent A) and acetonitrile gradient grade (solvent B).

Method H-NAMP1: 10 minutes isocratic method at a flow rate of 1 mL/min. The mobile phase was composed of 85% A and 15% B.

Method H-NAMP2: this method was suggested by the peptide manufacturer Innovagen. Gradient solvent system at a flow rate of 1 mL/min. Linear gradient from 6% to 31% B in 25 min. Post run to 6% B: 3 min.

The chromatograms were acquired at 198, 210, 225 and 254 nm wavelengths. The injection volume was 10 µL and samples were dissolved in ultrapure water.

Semi-preparative reversed-phase high-performance liquid chromatography (Semi-preparative RP-HPLC)

Semi-preparative RP-HPLC was performed on a Waters 1525 binary pump HPLC with a Waters 2992 photodiode array detector. The analysis of HPLC data was conducted on Waters Empower™ 3 software. Reversed-phase HPLC chromatography was carried out using a RP18, Waters X-Bridge C18, 5 µm, 10 x 150 mm and a Waters X Bridge Prep C18, 5 µm, 10 x 10 mm Guard Cartridge. The pure product collections were performed using a Waters fraction collector III.

Purification of NBA-BOC

The purification of NBA-BOC was performed by semi-preparative RP-HPLC, using a gradient solvent system at a flow rate of 5 mL/min.

The gradient mixture was composed of 0.1% aqueous AcOH (solvent A) and methanol gradient grade (solvent B). Gradient elution: 0-2 min 40% B; 2-12 min linear gradient from 40% to 100% B. Post run to 40% B: 2 min.

The chromatograms were acquired at 200, 254 and 340 nm wavelengths. The injections were performed using a 1 mL loop.

Purification of NAMP

The purification of NAMP was performed by semi-preparative RP-HPLC, using a 10 minutes isocratic method, at a flow rate of 3 mL/min

The mobile phase was composed of 85% 0.1% aqueous TFA and 15% acetonitrile gradient grade. The chromatograms were acquired at 198, 210, 225 and 254 nm wavelengths. The injections were performed with a 500 µL loop, using the partial loop-fill injection method.

Mass spectrometry

The characterization of NAMP was performed by mass spectrometry.

The mass spectrometer LTQ-Orbitrap Velos Pro was operated in positive ionization mode. Single MS survey scans were performed in the Orbitrap, recording a mass window between 150 and 2000 m/z. The Full Scan resolution was set to 120000. Sample were diluted 1:100 with a water/acetonitrile (50:50, v/v) solution containing 1% AcOH and introduced into the mass spectrometer by means of direct infusion at a flow rate of 5 µL/min with a syringe pump.

RESULTS AND DISCUSSION

Synthesis and characterization of ASAM

ASAM (Fig. 11) has been synthesized by a reaction reported in the literature [41]. The yield obtained was 54% w/w (see "Definition and terminology").

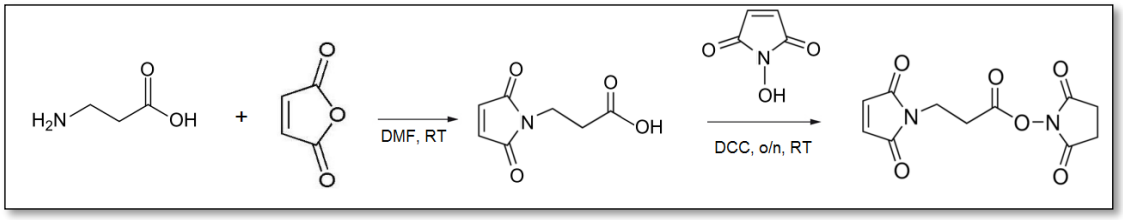

Fig. 11: Synthesis of ASAM.

The product was characterized by elemental analysis, thermal analysis, FT-IR, ^{1}H-NMR, ^{13}C-NMR and TLC. Purity was evaluated by RP-HPLC.

Elemental analysis

Elemental analysis on carbon, hydrogen and nitrogen was carried out in order to confirm the composition of the product.

Table 1 shows the comparison between the theoretical percentage composition of ASAM and the measured one.

The deviation of the elemental analysis from the theoretical composition is lower than 0.3%.

Table 1: Theoretical and actual percentage composition of ASAM.

	% C	% H	% N
Theoretical	49.63	3.79	10.52
Actual	49.45	3.80	10.35

Thermal analysis

A single endotherm at 163°C (extrapolated onset) was observed, corresponding to the melting point of ASAM in accordance to the hot stage microscopy analysis.

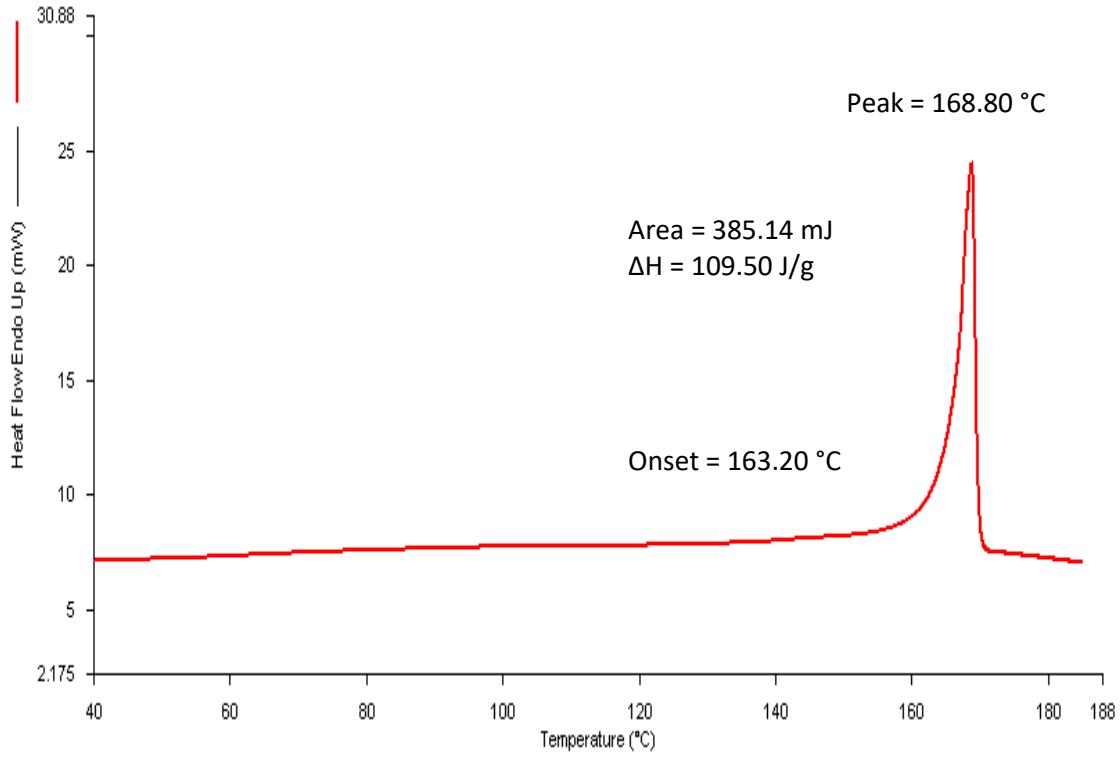

Fig. 12: DSC of ASAM, heating from 30°C to 185°C at 10°C/min.

IR Analysis

Fig. 13 shows the infrared spectrum of ASAM. At the high frequency portion of the spectrum, it is possible to observe maleimide C-H stretching vibrations (3108 cm^{-1}) and asymmetrical and symmetrical methylene stretching vibrations (2929 cm^{-1}, 2851 cm^{-1}). The most intense band occurs at 1720 cm^{-1}, corresponding to the C=O stretching vibration; the asymmetric and symmetric bands due to the ester C-O-C stretching vibrations occur at 1213 and 1072 cm^{-1} respectively.

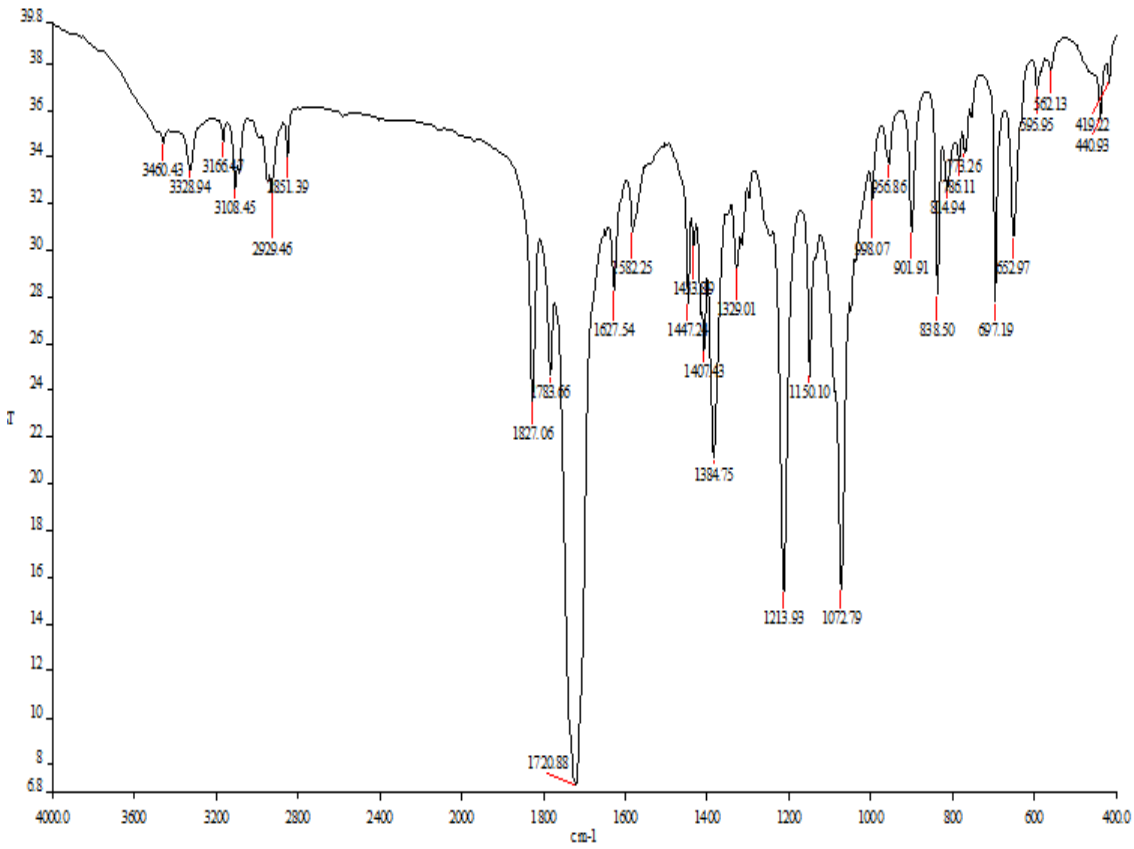

Fig. 13: IR spectrum of ASAM.

[1]H-NMR and [13]C-NMR spectroscopy

^{1}H-NMR (300 MHz, $CDCl_3$): 2.83 (4H, s, -C**H**$_2$C**H**$_2$-), 3.02 (2H, t, J = 7 Hz, -C**H**$_2$-N-), 3.93 (2H, t, J = 7 Hz, -C**H**$_2$-COO-), 6.74 (2H, s, -C**H**=C**H**-).

^{13}C-NMR (300 MHz, $CDCl_3$): 25.6 (-**C**H_2**C**H_2-), 29.7 (**C**H_2-COO-), 33.0 (-**C**H_2-N-), 134.3 (-**C**H=**C**H-), 166.0, 168.8, 170.1 (3 **C**=O).

A small amount of impurity is visible in both NMR spectra.

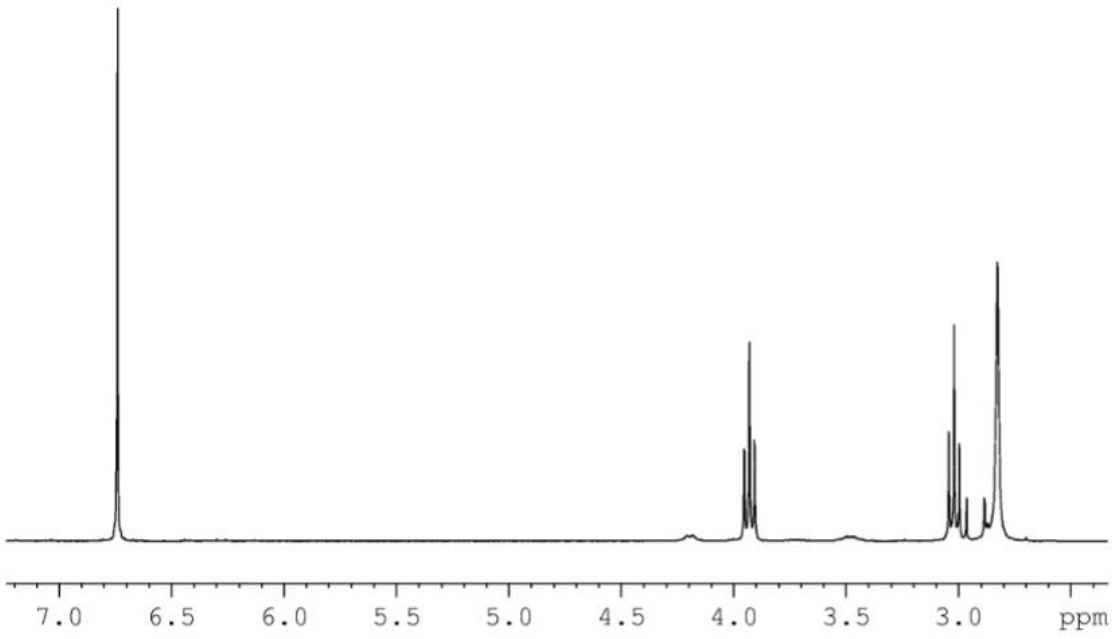

Fig. 14: [1]H-NMR of ASAM.

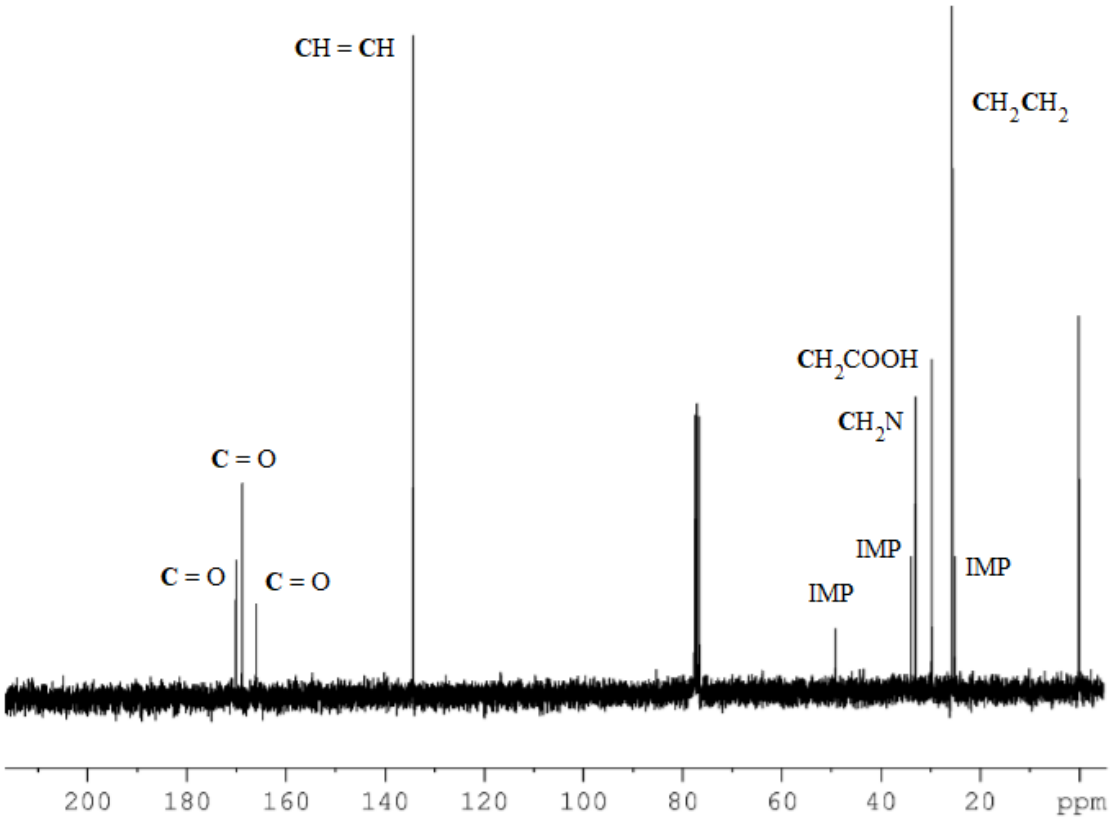

Fig. 15: [13]C-NMR of ASAM.

TLC

TLC analysis was performed using different solvent systems, and in the end, ethyl acetate/methanol 85:15 (v/v) were found to be the suitable mobile phase for proper separation (Fig. 16). β-alanine remains at the application line; maleic anhydride has a higher affinity with the stationary phase; N-hydroxysuccinimide forms a tailed peak on the plate and has a retention factor (R_f) of 0.55. Within the method detection limits, the product is sufficiently pure: the peak attributable to the product has an R_f of 0.85.

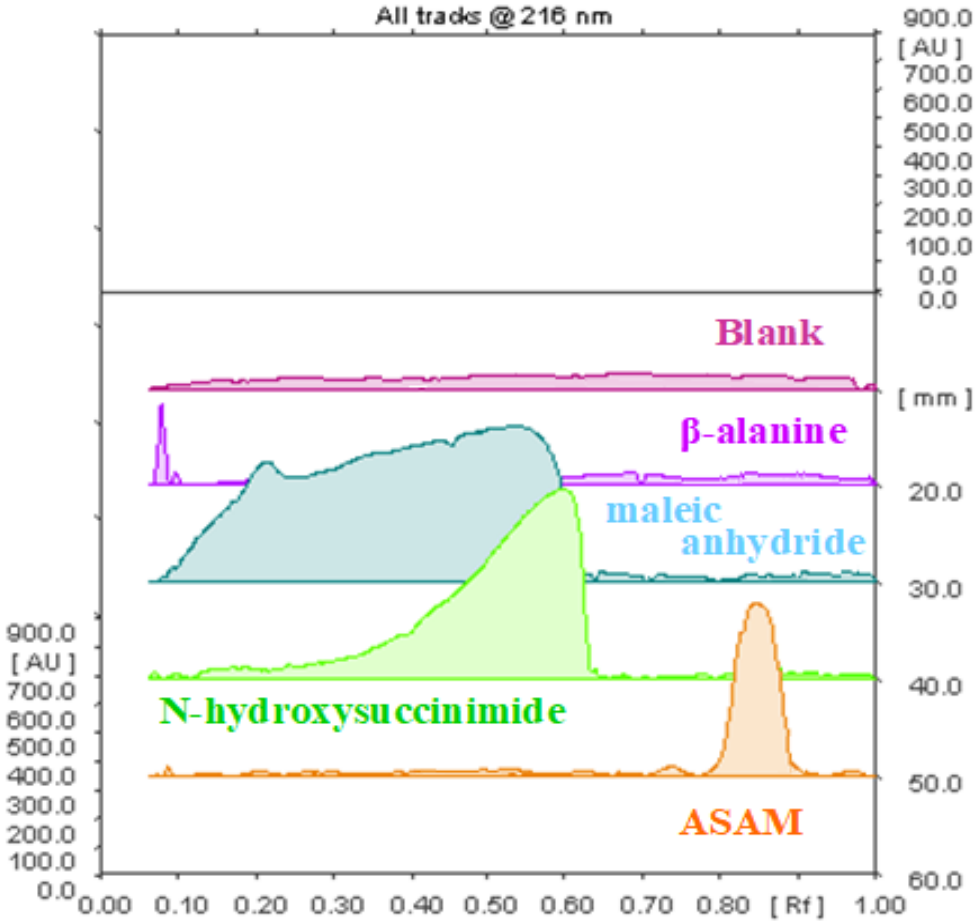

Fig. 16: TLC analysis of ASAM and standard solutions of β-alanine, maleic anhydride and N-hydroxysuccinimide.

RP-HPLC

In the selected mobile phase, ASAM has a retention time (t_R) of 2.4 minutes, but shows a small amount of impurity with t_R = 10.2 minutes (Fig. 17).

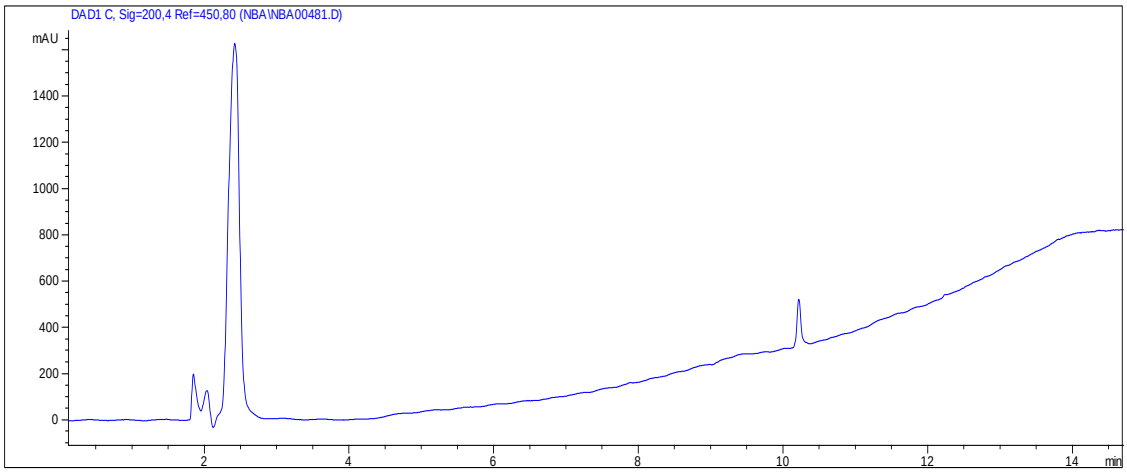

Fig. 17: RP-HPLC of ASAM in methanol conc. 1 mg/mL.

In accordance to the ^{1}H-NMR and ^{13}C-NMR analyses, and from the RP-HPLC of standard solutions, it was assumed that this impurity could be a residue of N,N′-dicyclohexylurea (DCU), which forms by the reaction between N-N'-dicyclohexylcarbodiimide (DCC) and a generic carboxylic compound (Fig. 18).

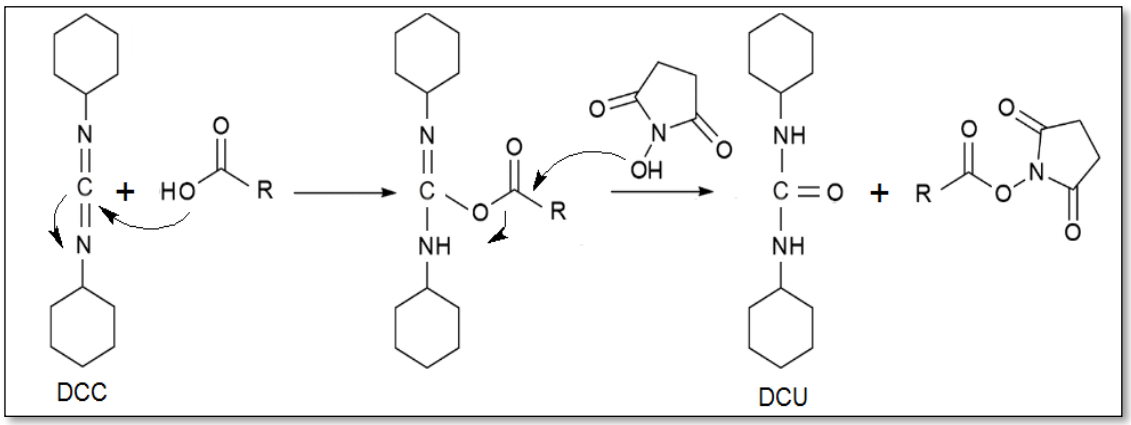

Fig. 18: Mechanism of reaction of DCC with a generic carboxylic compound and formation of DCU.

Fig. 19 shows the comparison between ASAM and a DCC aqueous solution, which was heated to 60°C for 1h to form DCU. The peak with t_R = 13.8 min is DCC, while the peak at 10.2 min is the impurity that forms when heating.

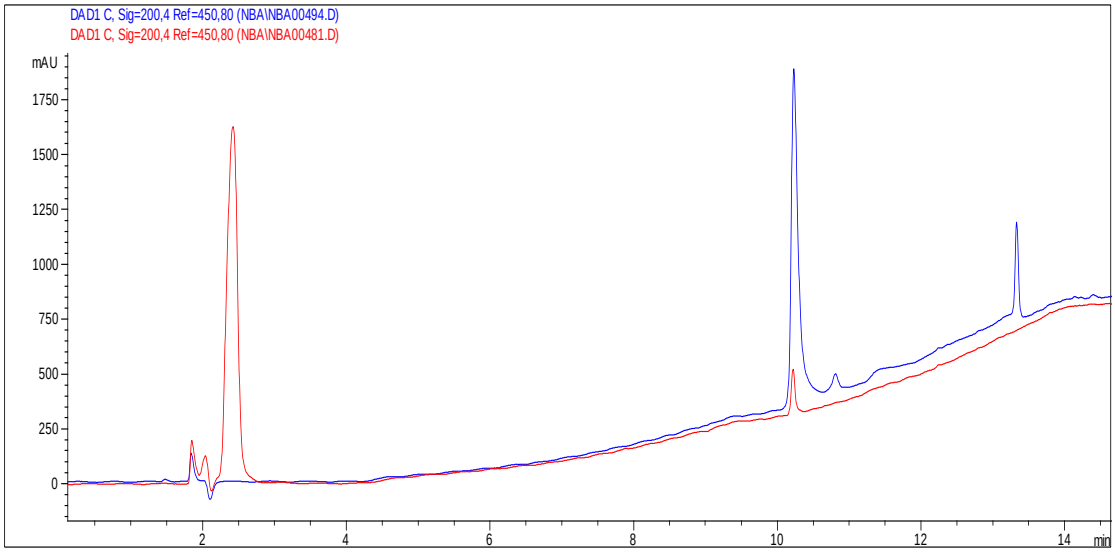

Fig. 19: Comparison between ASAM and a DCC aqueous solution heated at 60°C for 1h.

Synthesis of N-Boc-norbiotinamine

Most norbiotinamine syntheses reported in the literature refer to a work published by Szalecki [35]. It consists in a one-pot reaction wherein biotin is added in equimolar amounts to TEA and DPPA, in t-BuOH at reflux for 18h, to form the derivate N-Boc norbiotinamine. Norbiotinamine is then obtained by acidic hydrolysis (Fig. 20).

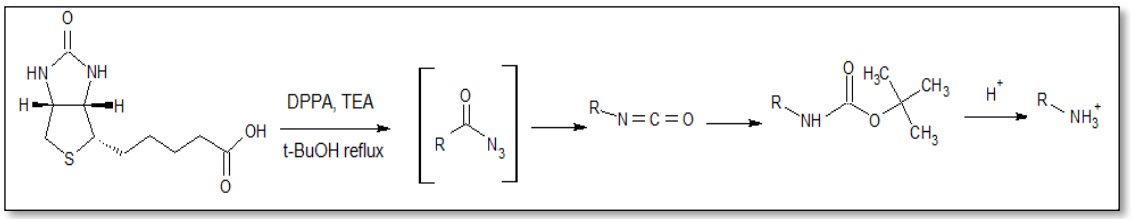

Fig. 20: One-pot reaction and N-Boc hydrolysis for the synthesis of norbiotinamine.

Initially, the reaction was carried out under the reported conditions, but it gave low reaction yield and purity. Also purification steps appeared more complicated also in term of cost, time and purity results.

Consequently, it was decided to study the mechanism of the one-pot reaction in order to find out its criticalities.

The reaction mechanism involves: TEA salification of biotin, which in its ionic form is able to attack the DPPA phosphate group; the formation of an acylazide that, by Curtius rearrangement, leads to nitrogen expulsion by heating and to the formation of isocyanate; nucleophilic attack of tert-butoxide on the isocyanate to produce the tert-butyl carbamate (Fig. 21).

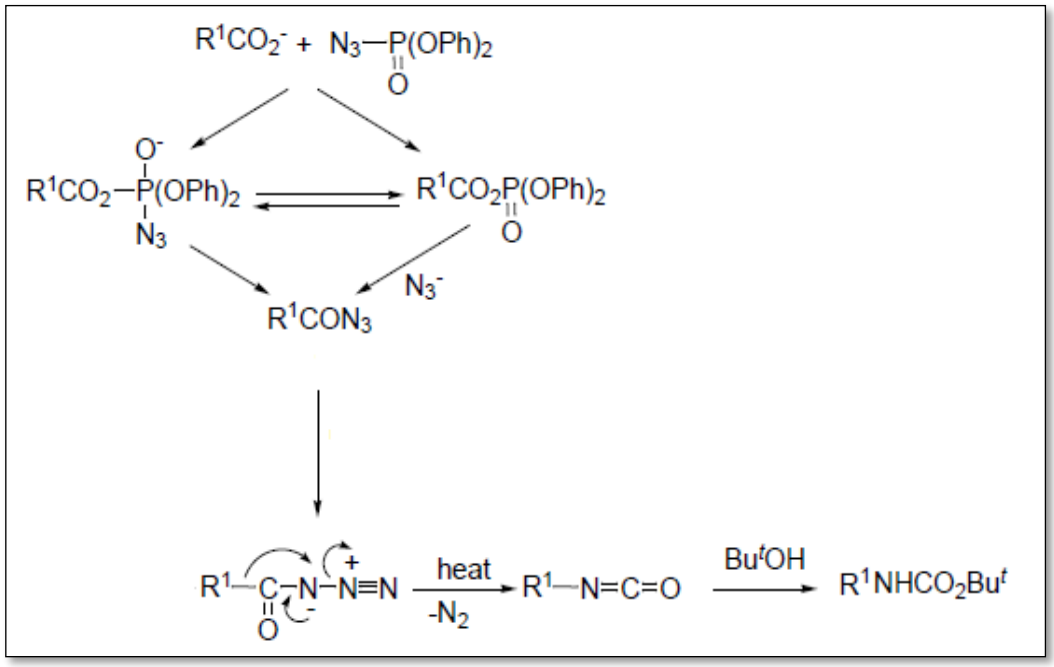

Fig. 21: One-pot reaction mechanism.

Since biotin is very slightly soluble in t-BuOH, even in the presence of TEA, t-BuOH was replaced with a high dielectric constant and aprotic solvent, DMF, which had shown to dissolve biotin better than t-BuOH.

Furthermore, the reaction temperature was modified, applying gradual heating in order to study the optimal thermal conditions for the isocyanate formation.

For this reason and for obtaining norbiotinamine by thermal degradation of the isocyanate, t-BuOH was not used.

The reaction was carried out by solubilizing biotin in DMF and then adding TEA and, after 10 minutes, DPPA at room temperature. After 1h the mixture was heated gradually (20°C/h) up to 120°C and refluxed under stirring overnight.

Enduring the reaction a white precipitate formed (NBA I2a), that increased by adding water or keeping the suspension at -20°C.

From RP-HPLC analysis, a study of the solubility of NBA I2a in different solvents showed that it is insoluble in apolar solvents and slightly soluble in water, methanol and t-BuOH, but under acidic condition the solubility improves.

Moreover, the shape of the peak and the t_R change depending on the injection solvents (Fig. 22): in water and t-BuOH NBA I2a showed one peak at 3.65 and 2.60 min respectively, while in methanol a peak splitting with t_R of 3.5 min was observed.

These considerations led to the hypothesis that NBA I2a might have an ionisable group, as an amine group, so a spectroscopic analysis was carried out.

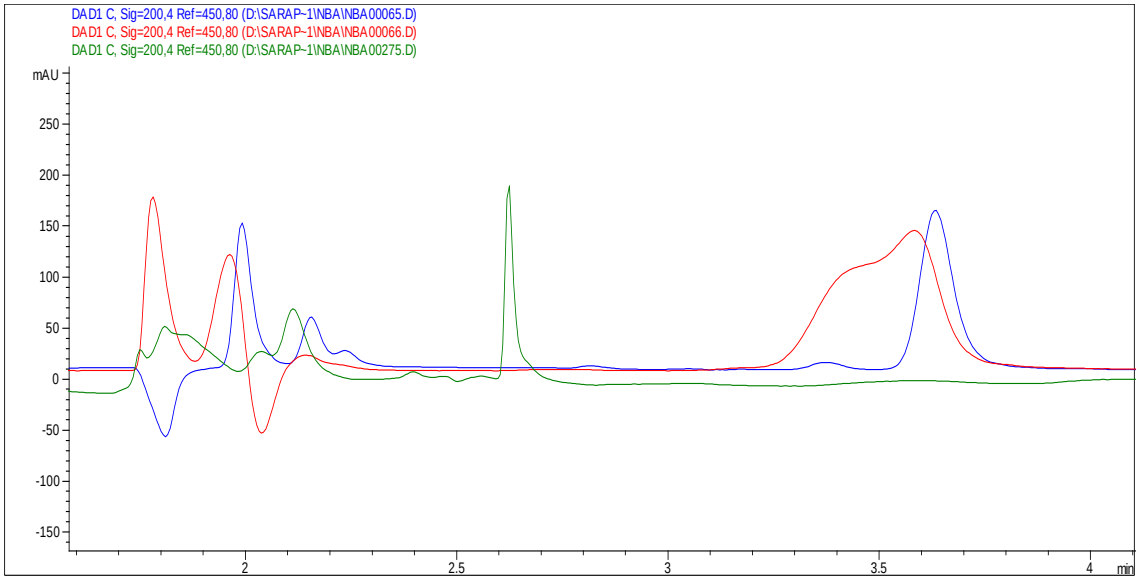

Fig. 22: NBA I2a in t-BuOH (green), methanol (red) and water (blue).

The ^{1}H-NMR and ^{13}C-NMR analyses suggested the formation of a norbiotinamine urea. The supposed mechanism (Fig. 23) involves the formation of the carbamic acid, from the isocyanate in presence of water, which, losing CO_2 by heating, converts into an amine. Afterwards, the nucleophilic attack of the amine on the isocyanate would lead to the formation of the ureic derivative.

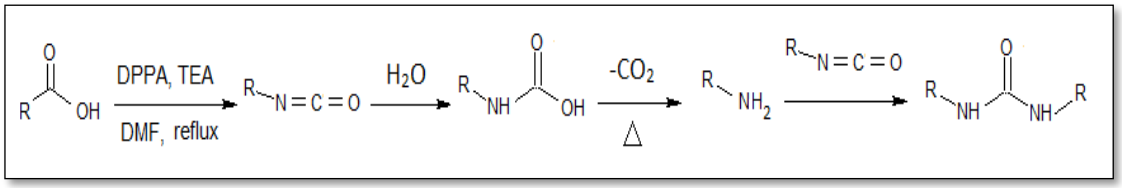

Fig. 23: Supposed mechanism of formation of norbiotinamine urea.

Fig. 24 shows the ^{13}C-NMR (300 MHz, DMSO-d_6) of NBA I2a and the supposed assignment of signals: δ 162.6, 158.1, 60.9, 59.1, 55.4, 30.0, 27.9, 25.9.

Using distortionless enhancement by polarization transfer (DEPT), a technique used for determining the presence of primary, secondary and tertiary carbon atoms, it was possible to identify also the signals of $^{6}CH_2$ (δ 39.8) and $^{7}CH_2$ (δ 38.9).

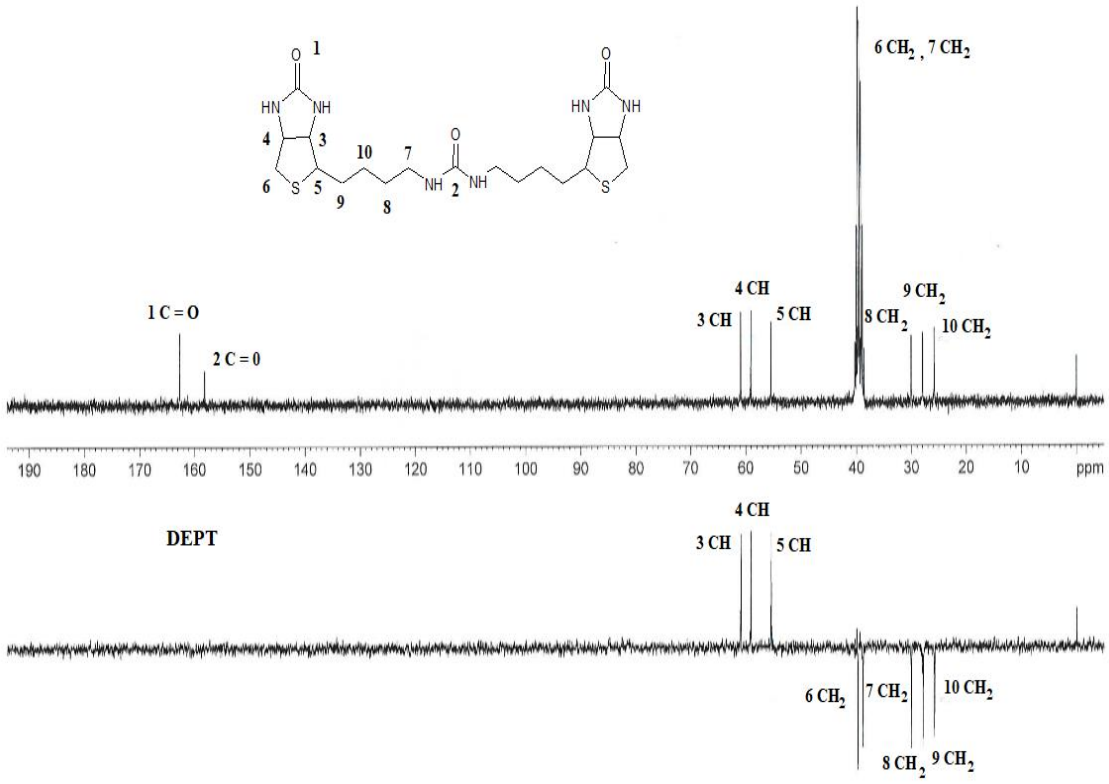

Fig. 24: ^{13}C-NMR of NBA I2a.

After in-depth bibliographic research, another hypothesis was formulated: NBA I2a could be a dimer or a trimer of norbiotinamine formed by heating because of the presence of a high-dielectric constant solvent (DMF) and a tertiary base (TEA) (Fig. 25) [42].

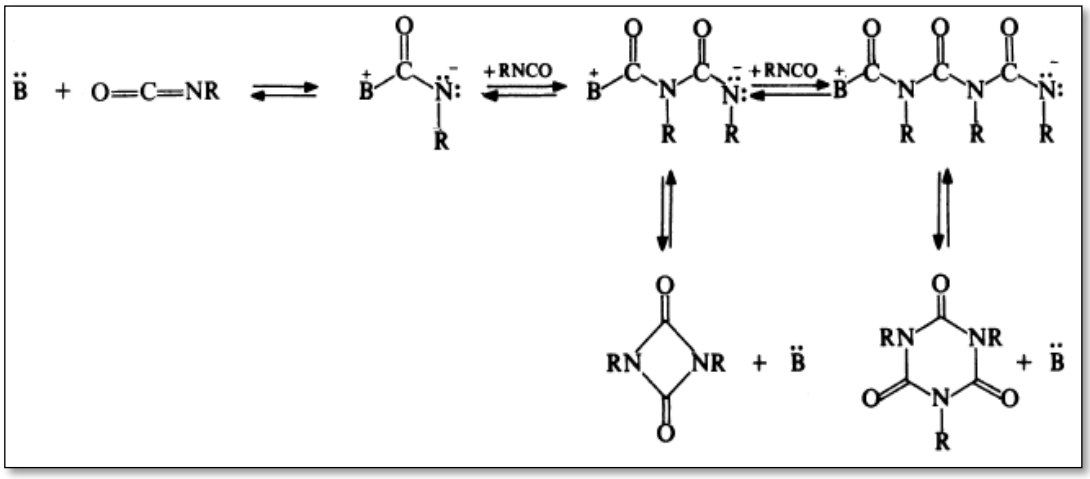

Fig. 25: Proposed mechanism for base-catalysed dimerization and trimerization.

Although more analysis should be carried out, since NBA I2a is a molecule not yet known in the literature, the applied reaction conditions did not lead to the formation of norbiotinamine.

For this reason, it was decided to analyse the role of t-BuOH in the reaction.

In the one-pot reaction, t-BuOH is solvent, but also reagent, since the reaction mechanism provides that the tertbutoxide forms the N-Boc-norbiotinamine by nucleophilic attack on the isocyanate.

Therefore, the reaction was repeated at the same modified conditions of the previous reaction, adding t-BuOH after gradual heating up to 90°C (rather than 120°C).

The reaction mixtures with and without t-BuOH addition were analysed by RP-HPLC, using a method already reported in the literature for the analysis of N-Boc-norbiotinamine [39] (Fig. 26).

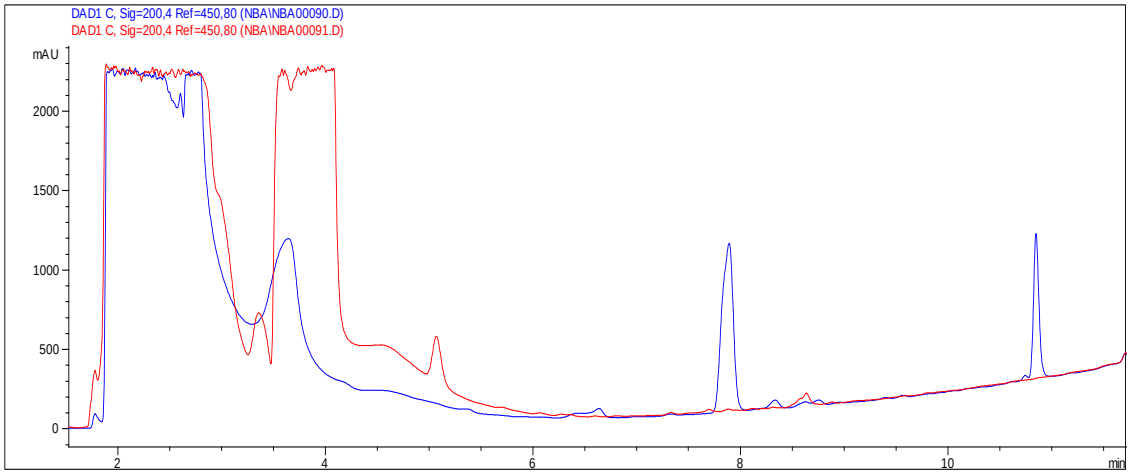

Fig. 26: RP-HPLC comparison between the reaction mixture without (red) and with the addition of t-BuOH (blue).

Besides the formation of NBA I2a, the reaction mixture including t-BuOH showed the presence of two more peaks compared to the previous reaction: one with a t_R of 7.8 minutes and the other with t_R of 10.7 minutes. In accordance with the previously cited work, N-Boc-norbiotinamine should have a t_R of 10.7 minutes, but, by analysing the UV spectrum of the second peak, it appeared to be a DPPA derivative, that disappeared by drying. For this reason, the peak at 7.8 minutes was considered more interesting and the reaction was repeated adding t-BuOH after heating at 40°C and monitoring the reaction at different conditions of time and temperature (Fig. 27).

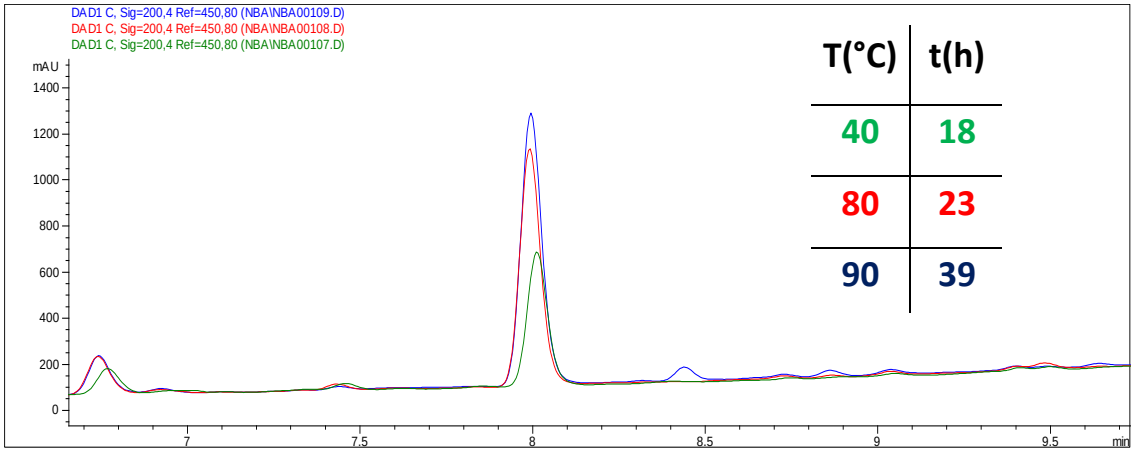

Fig. 27: Zoom of the reaction mixture chromatogram showing the effect of increasing time and temperature on peak at 7.8 min.

Fig. 27 shows that the area of the peak at 7.8 min increases with reaction time and temperature. The peak was subsequently isolated with semi-preparative RP-HPLC and characterized by ^{1}H-NMR, IR and DSC analysis.

The ^{1}H-NMR analysis confirmed the presence of the biotin nucleus, but, because of the small amount of obtained product, it was not possible to establish exactly the identity of the compound.

Furthermore, the isolated product was hydrolysed by TFA/dichloromethane 1:1, at 0°C for 2h, and after drying and solubilisation in the mobile phase, it was analysed in RP-HPLC.

The formation of a peak with t_R of 2.8 min was observed, compatible with the t_R of norbiotinamine as reported in the literature [39] at the same chromatographic conditions.

In order to reduce the formation of NBA I2a and increase the reaction yield, another modification of the reaction conditions was carried out: t-BuOH was added at room temperature, then gradually heated up to 90°C.

The chromatogram of the obtained reaction mixture, dried and dissolved in the mobile phase, is shown in Fig. 28.

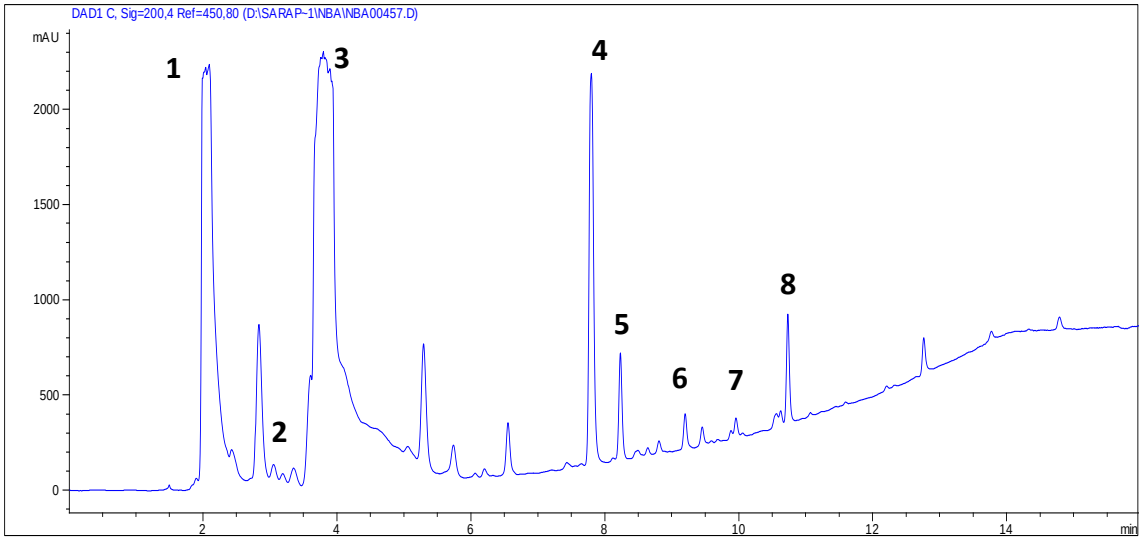

Fig. 28: Chromatogram of dry residue of reaction mixture performed under modified conditions.

Many of the peaks of the chromatogram have been characterized and compared with the peaks obtained analysing by RP-HPLC the dry residue of the one-pot reaction, carried out at the same conditions reported in literature (Fig. 29).

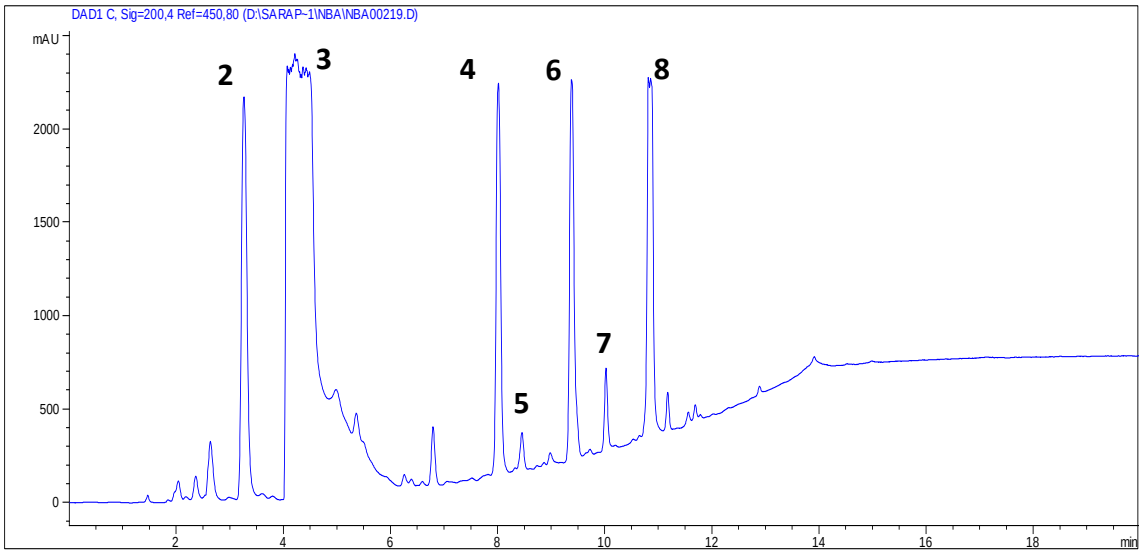

Fig. 29: Chromatogram of dry residue of the one-pot reaction in t-BuOH.

Peak 1 in Fig. 28 is the residue of DMF, still present in the mixture after drying due to its high boiling point.

In the chromatogram of the one-pot reaction it is possible to note the presence of unreacted biotin (peak 2), which is practically absent in the DMF reaction, probably because it precipitates from the reaction mixture as NBA I2a.

Compounds 3 and 8 were related to the addition of DPPA in the reaction mixture, while peak 7 probably formed by the reaction between t-BuOH and the mobile phase.

In fact, even after heating an acidic solution of t-BuOH for 1 hour at 90°C under stirring, the chromatogram of the resulting solution showed the formation of compounds 7 and a compound with t_R of 15 minutes (Fig. 30).

This substance is also presence in both the reaction mixtures, but its peak disappears from the chromatogram after drying. Therefore, it is very volatile and might be related to the formation of isobutylene from the dehydration of t-BuOH under acidic conditions.

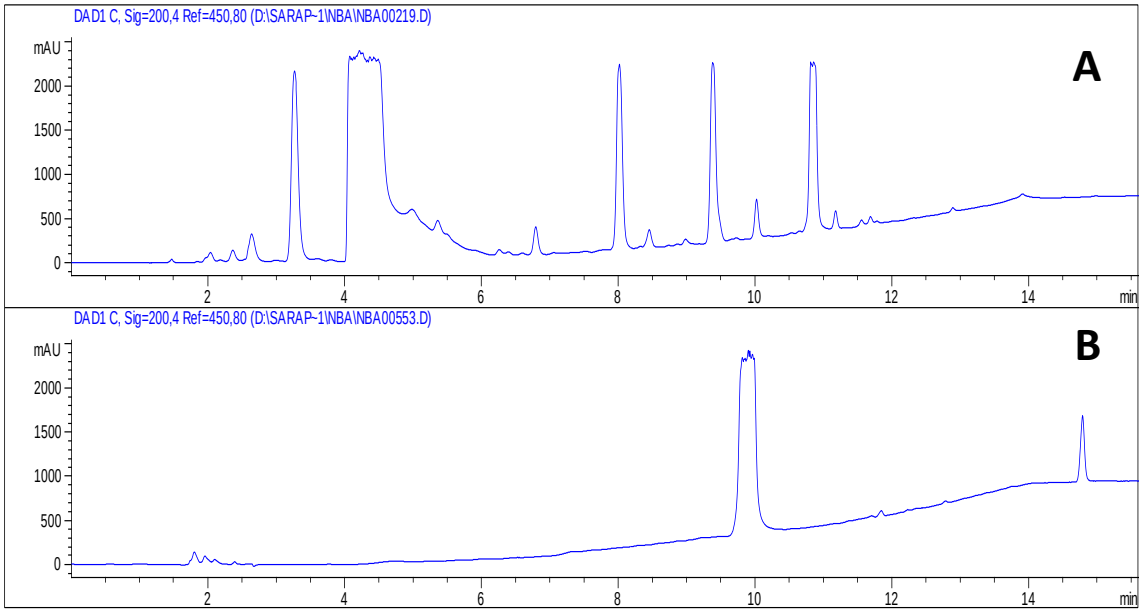

Fig. 30: RP-HPLC comparison between one-pot reaction (A) and an acidic solution of t-BuOH heated at 90°C (B).

In order to identify peaks related to the presence of biotin, the one-pot reaction and the reaction performed under modified conditions were compared to mixtures not containing biotin treated under the same reaction conditions (Fig. 31 and Fig. 32 respectively).

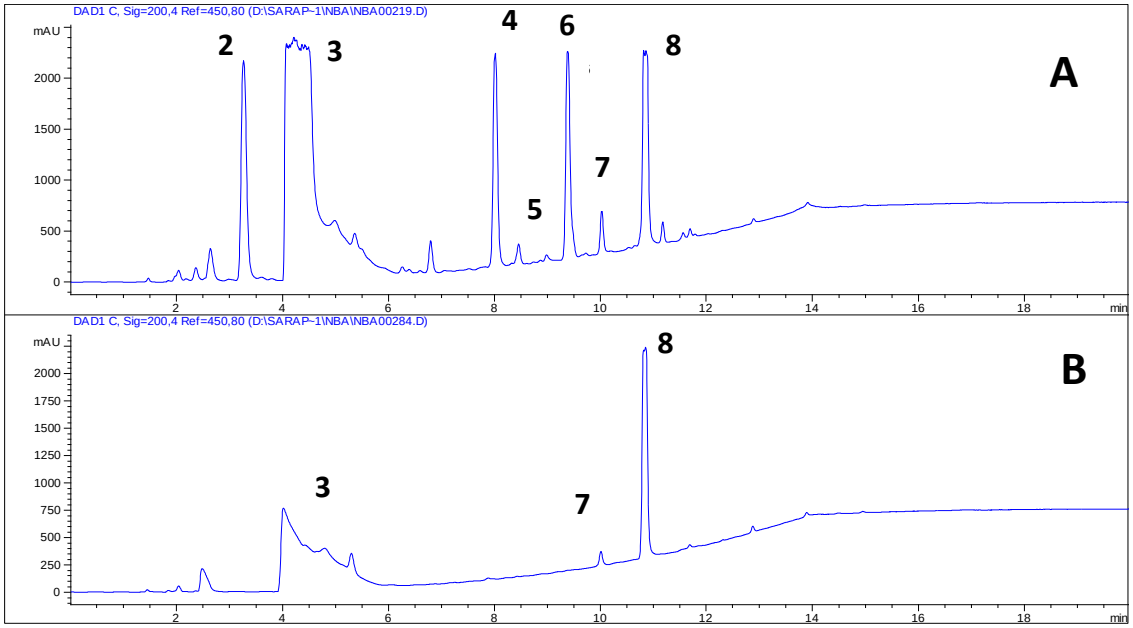

Fig. 31: RP-HPLC comparison between residues of one-pot reaction in presence of biotin (A) and without biotin (B).

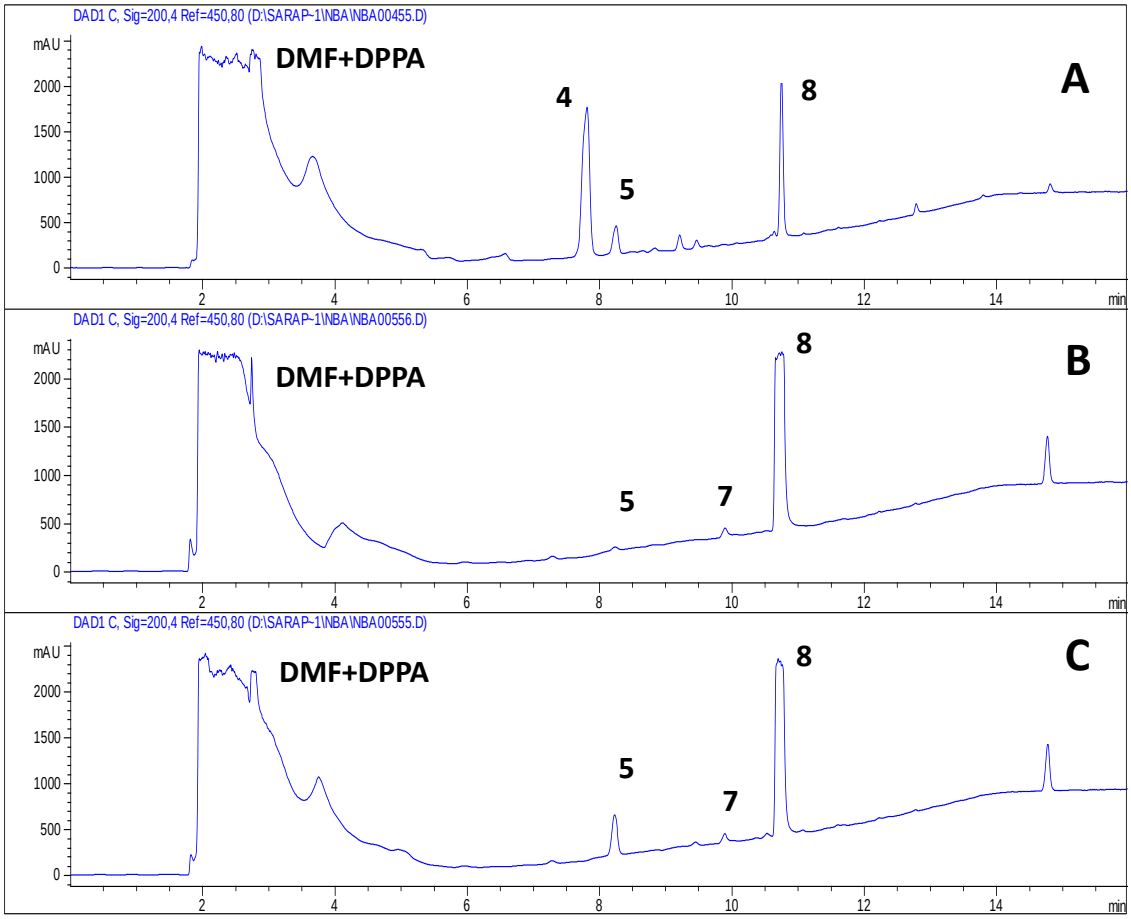

Fig. 32: RP-HPLC comparison of the reaction mixture performed under modified conditions in presence of biotin (A), without biotin at RT (B) and without biotin heating up to 120°C (C).

The comparisons revealed that peaks 4 and 6 are related to the presence of biotin in the reaction mixture: peak 4 is present in both reactions, while peak 6 is shown only in the one-pot reaction. Furthermore, peak 5 forms in DMF even without biotin and increases with heating.

A well-known secondary product of the one-pot reaction is the t-butyl ester of biotin.

In accordance with the literature [39] and by using software that allow to estimate the RP-HPLC t_R of the compounds by calculating the logP, the t_R of this compound was presumed to be higher than the one of N-Boc-norbiotinamine, applying the reported chromatographic conditions. So peak 4 was hypothesized to be N-Boc-norbiotinamine and peak 6 the t-butyl ester of biotin.

Furthermore, from the comparison of the chromatograms of the reactions performed in t-BuOH and DMF, the one-pot reaction resulted to generate more secondary products and yield a lower amount of desired product.

For this reason it was decided to synthesize the product in DMF and to set the best conditions of temperature and time for optimizing the yield.

The reaction was repeated twice, heating up to 90°C and 120°C. As shown in the comparison between the reaction chromatograms (Fig. 33), higher temperature gave a higher yield as well as the increase of peak 5 compound. So the reaction temperature was set to 90°C.

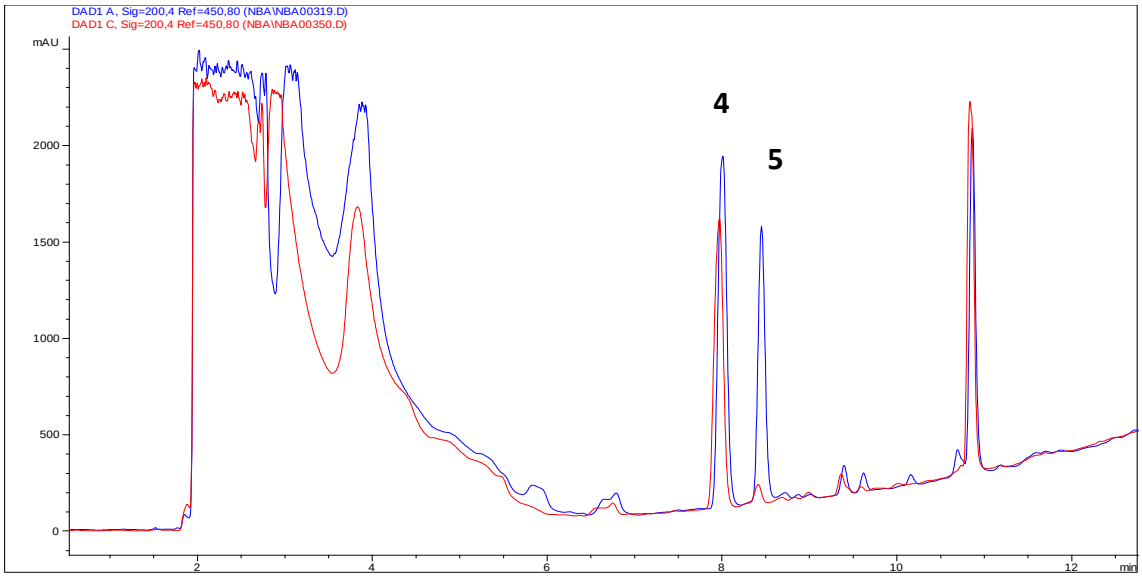

Fig. 33: RP-HPLC comparison between the reaction mixtures heated up to 90°C (red) and to 120°C (blue).

Finally, the reaction was carried out for 24h and 48h. From the chromatograms of the reaction mixtures (Fig. 34), a longer reaction time did not improve the yield significantly, so the reaction time was set to 24h.

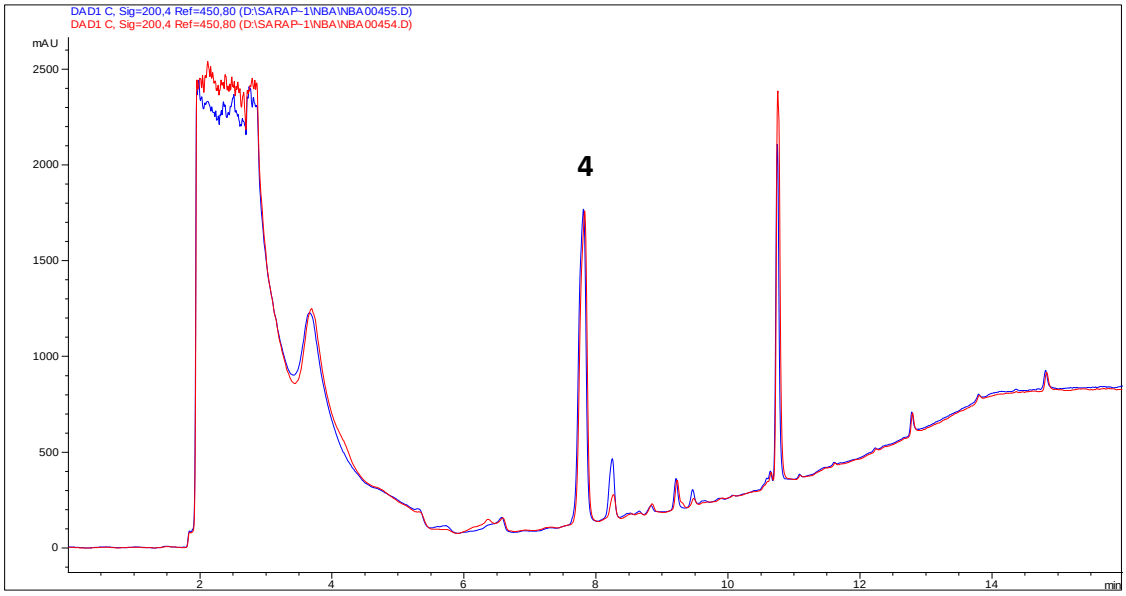

Fig. 34: Comparison between the reaction mixture after 24h (red) and 48h (blue).

The purification of N-Boc-norbiotinamine was initially performed by washings and solvent extractions.

After drying the reaction mixture, the residue was washed 3 times with a 0.5 N $NaHCO_3$ and 5 N NaCl solution, for removing the hydrophilic substances: $NaHCO_3$ basicity is functional to the elimination of acidic substances such as biotin and DPPA derivatives, while the presence of concentrate NaCl reduces the solubility of the product in water.

The dry residue was then washed with hexane to remove the hydrophobic fraction of the reaction mixture, and finally the product was obtained pure by repetitive extractions with chloroform.

For the low yields obtained, it was decided to perform the final purification by semipreparative RP-HPLC.

N-Boc-norbiotinamine was obtained highly pure with a yield of 50% (Fig. 35).

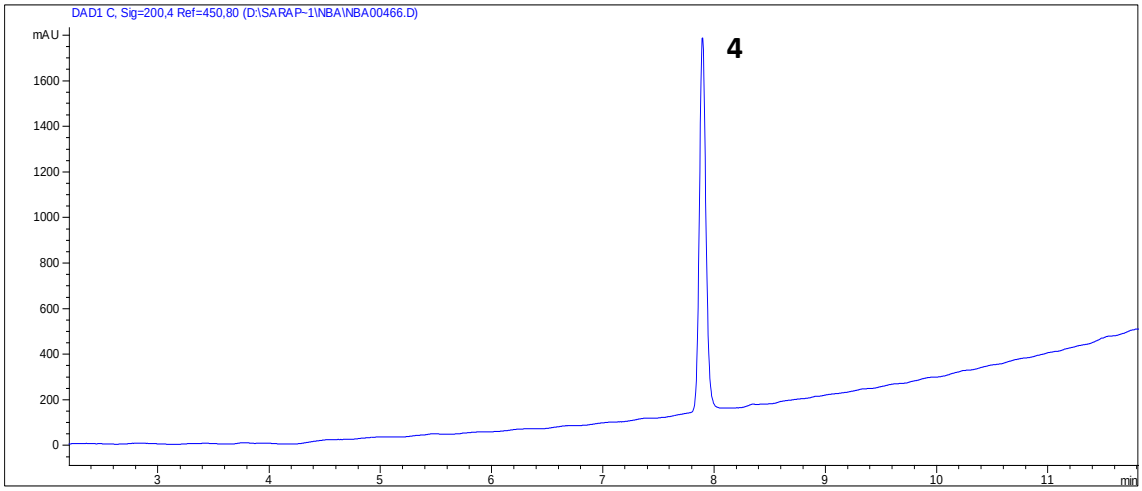

Fig. 35: HPLC purity assessment of isolated N-Boc-norbiotinamine.

Characterization of N-Boc-norbiotinamine

The product was characterized by elemental analysis, thermal analysis, FT-IR, ^{1}H-NMR and ^{13}C-NMR.

Elemental analysis

Elemental analysis on C, H, N and S was carried out in order to confirm the composition of the product.

Table 2 shows the comparison between the theoretical percentage composition of N-Boc-norbiotinamine and the experimental one.

The deviation of the elemental analysis from the theoretical composition is lower than 0.3%.

Table 2: Theoretical and actual percentage composition of N-Boc-norbiotinamine.

	%C	%H	%N	%S
Theoretical	53,31	7,99	13,32	10,16
Actual	53,35	8,13	13,62	10,04

Thermal analysis

The thermal profile of the substance shows a single endotherm at 168°C (extrapolated onset), which is the melting point of N-Boc-norbiotinamine, in accordance with the hot stage microscopy observation (Fig. 36).

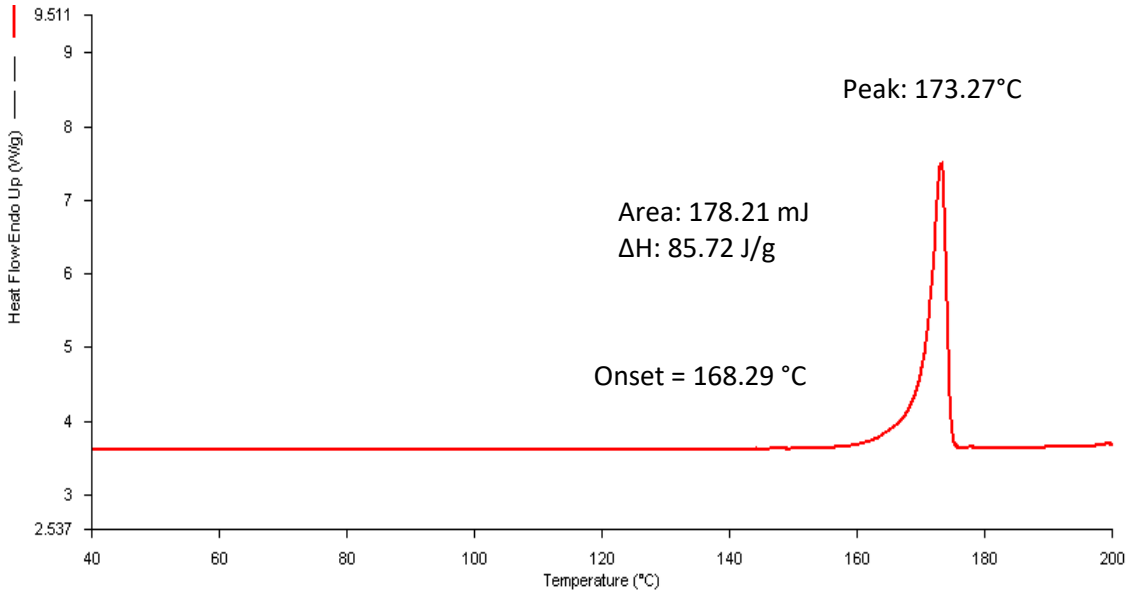

Fig. 36: DSC profile of N-Boc-norbiotinamine heating from 40°C to 200°C at 10°C/min

IR Analysis

The N-Boc-norbiotinamine infrared spectrum is shown in Fig. 37.

In the high frequency portion of the spectrum, it is possible to observe the N-H stretching (3535 cm^{-1}, 3296 cm^{-1}), followed by stretching of methyl and methylene groups (2978 cm^{-1}, 2930 cm^{-1} and 2865 cm^{-1}). The most intense signal corresponds to the stretching C=O of the carbamate group (1693 cm^{-1}), which has a shoulder probably related to the stretching C=O of the ureic group (1675 cm^{-1}).

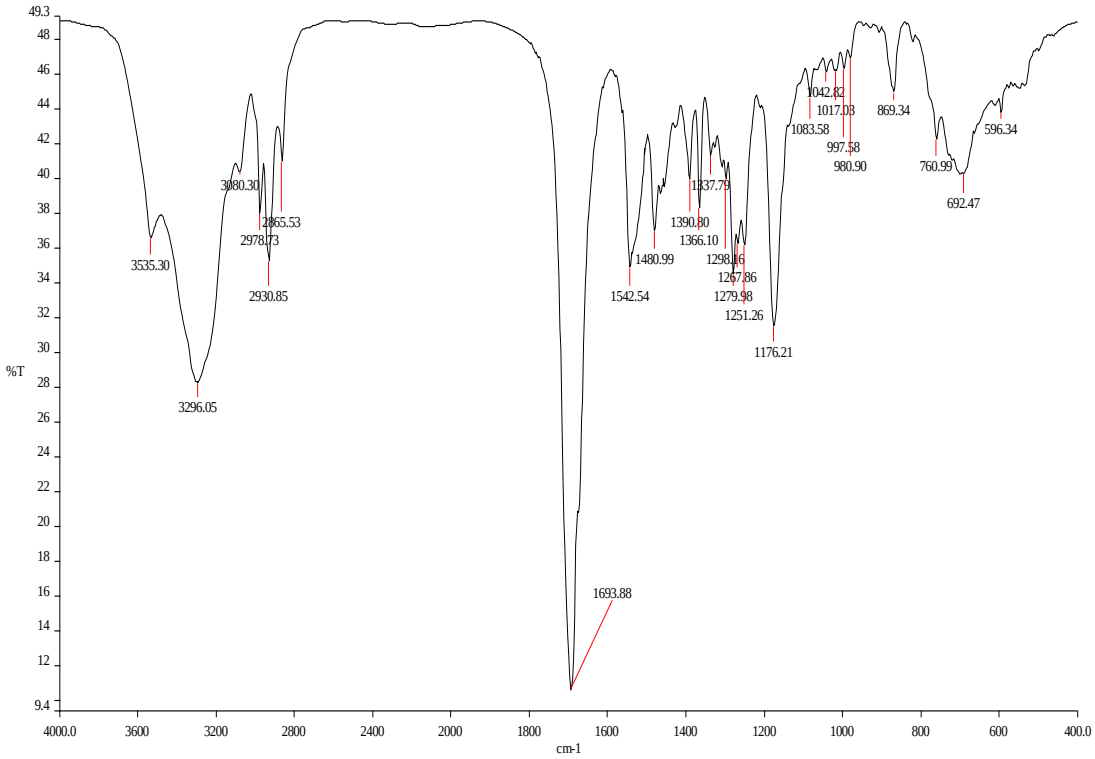

Fig. 37: IR analysis of N-Boc-norbiotinamine.

^{1}H-NMR and ^{13}C-NMR spectroscopy

^{1}H-NMR (Fig. 38) and ^{13}C-NMR (Fig. 39) spectra were acquired, obtaining results comparable with those found in the literature [43].

^{1}H-NMR (300 MHz, $CDCl_3$): 4.50 (1H, dd, **^{3}H**), 4.34 (1H, dd, J= 4.5, 7.5 Hz, **^{4}H**), 3.13 (1H, m, **^{5}H**), 2.99 (2H, m, **^{7}H**), 2.90 (1H, dd, J=5, 12.7 Hz, **^{6}H**), 2.73 (1H, d, J= 12.7 Hz, **^{6}H**), 1.70-1.52 (6H, m, **^{8}H**,**^{9}H**,**^{10}H**), 1.45 (9H, s, **^{11}H**).

^{13}C-NMR (300 MHz, $CDCl_3$): δ 164.9, 157.6, 79.1, 61.6, 60.5, 55.3, 40.7, 40.4, 29.7, 28.5, 28.3, 25.6.

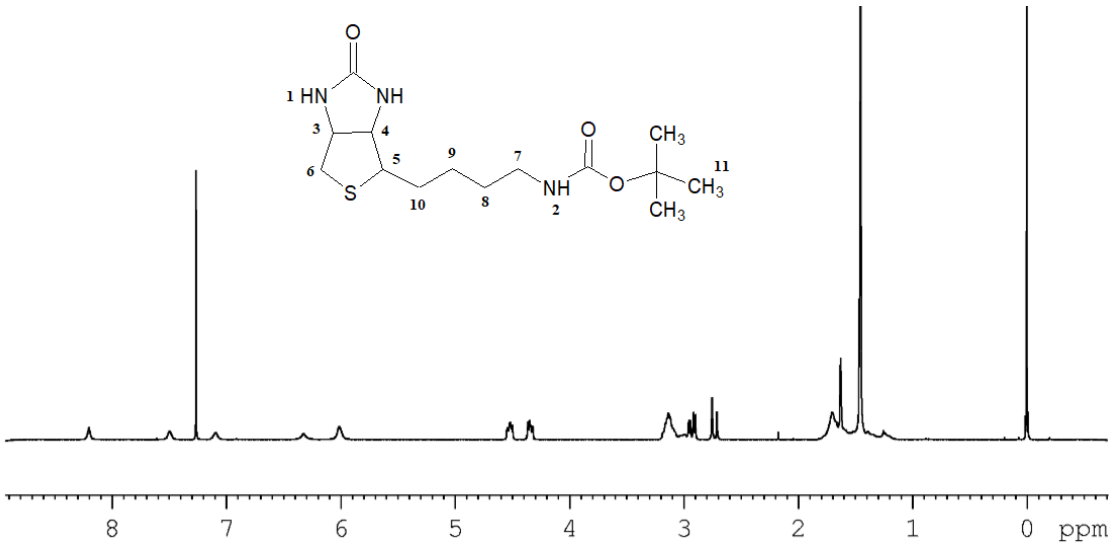

Fig. 38: [1]H-NMR of N-Boc-norbiotinamine in $CDCl_3$.

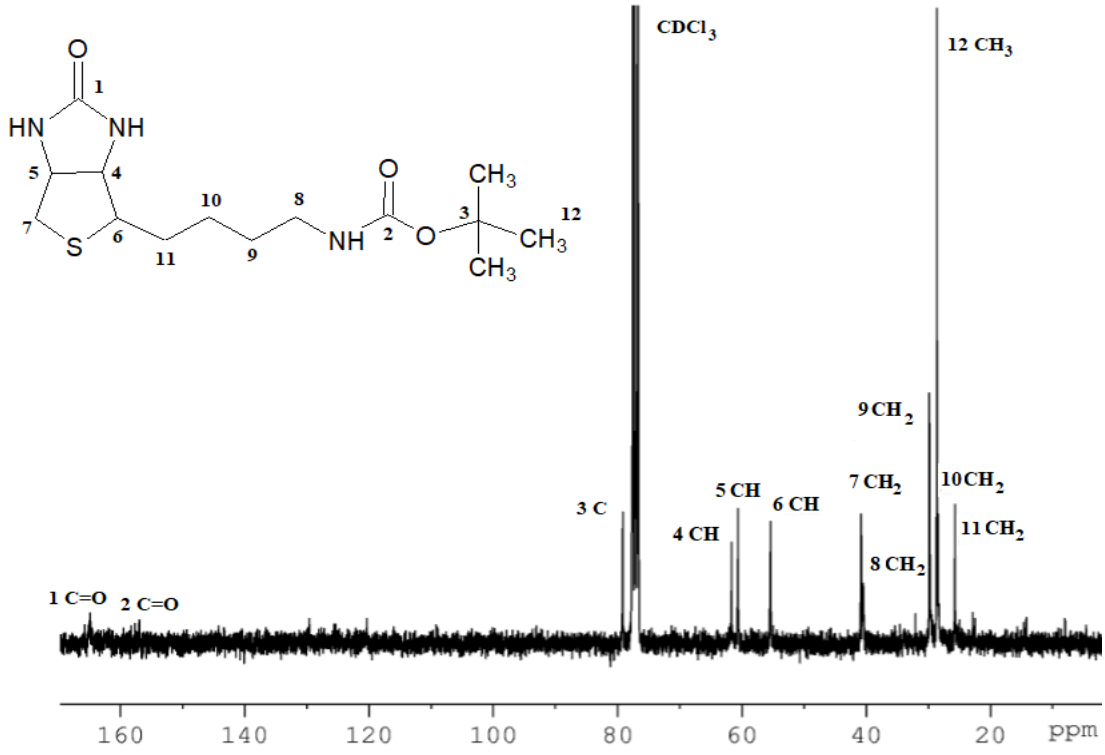

Fig. 39: [13]C-NMR of N-Boc-norbiotinamine in $CDCl_3$.

Synthesis of norbiotinamine

After identifying and characterizing N-Boc-norbiotinamine, the hydrolysis reaction was performed. The reaction was carried out at the condition reported in the literature and the obtained product was used for the following reaction without purification.

Fig. 40 shows the disappearance of N-Boc-norbiotinamine peak and the formation of a compound with a t_R compatible with norbiotinamine in accordance with the literature [39].

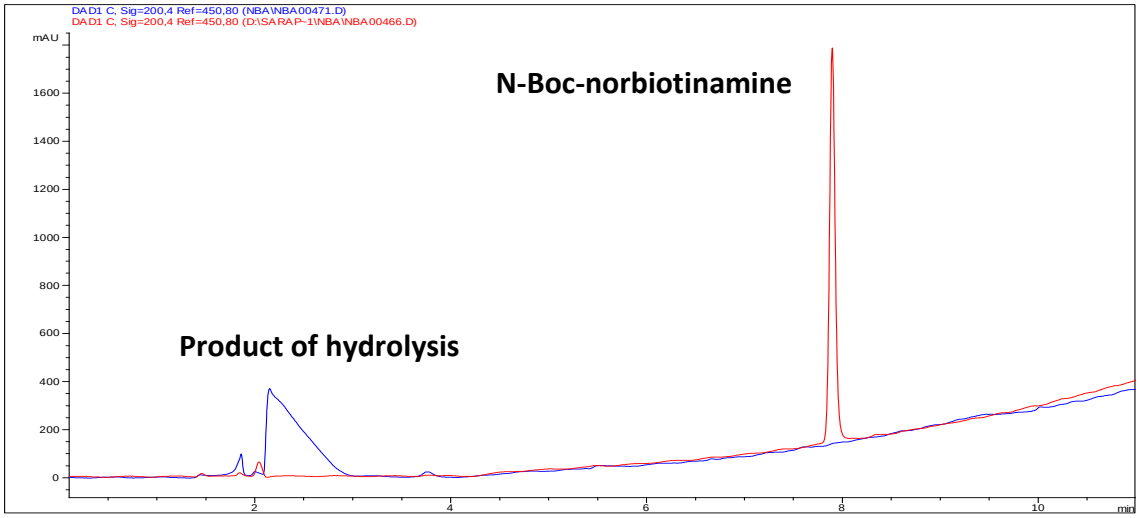

Fig. 40: RP-HPLC comparison between N-Boc-norbiotinamine and the hydrolysed product.

Synthesis of N-norbiotinyl-β-maleimidopropionylamide

One reaction is reported in the literature for the synthesis of N-norbiotynil-β-maleimido propionylamide [35]. Chloroform is used as solvent and the reaction conditions are room temperature for 18 hours, using a molar ratio of 1.5 between β-maleimidopropionate and norbiotinamine.

Initially, the reaction was performed applying the aforementioned conditions, adding TEA in molar ratio 1:1 with norbiotinamine, in order to favour the nucleophilic attack of the amine on the activated carboxyl group of ASAM (Fig. 41). At the end, the obtained reaction mixture dried and dissolved in the mobile phase, was analysed by RP-HPLC with *H-NAM1* method (Fig. 42).

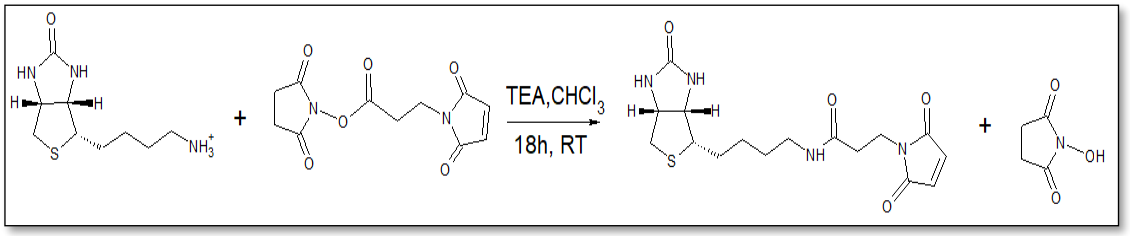

Fig. 41: Synthetic scheme of NAM at the reported conditions, with the addition of TEA.

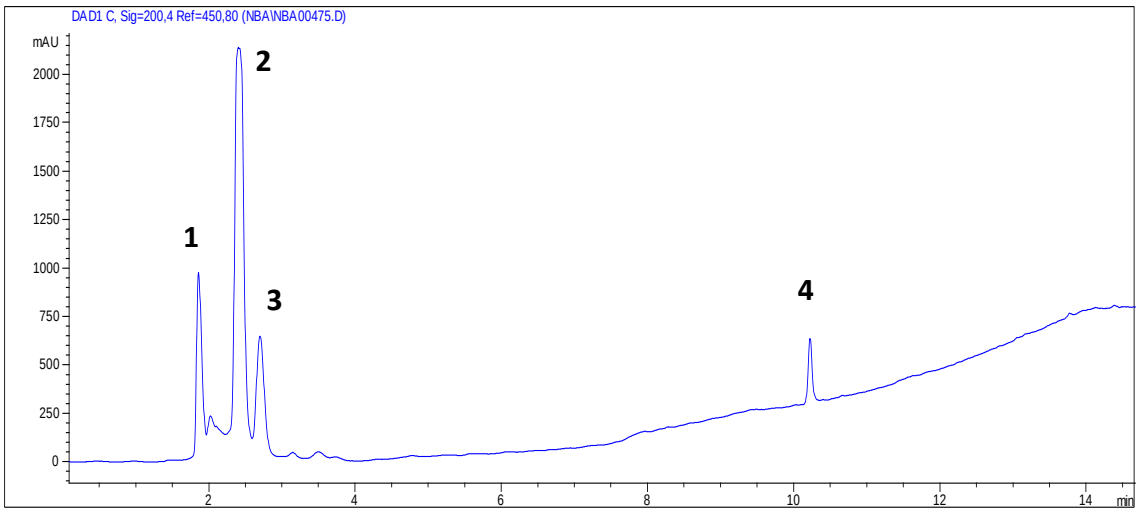

Fig. 42: RP-HPLC analysis of the reaction mixture.

The peak assignment of chromatogram in Fig. 42 was performed by the injections of standard solutions.

Peak 1 was identified as N-hydroxysuccinimide, which is cleaved from ASAM after the nucleophilic attack of the amine on the carboxylic group.

Peak 2 and peak 4 corresponds respectively to unreacted ASAM and its impurity.

Peak 3 was supposed to be the product, as suggested by further RP-HPLC analyses.

First, the reaction was carried out at room temperature and at 40°C: Fig. 43 shows the comparison of the two reaction mixtures.

The decrease of ASAM and the increases of N-hydroxysuccinimide and peak 3 compound at 40°C were considered indicative of the progression of the reaction.

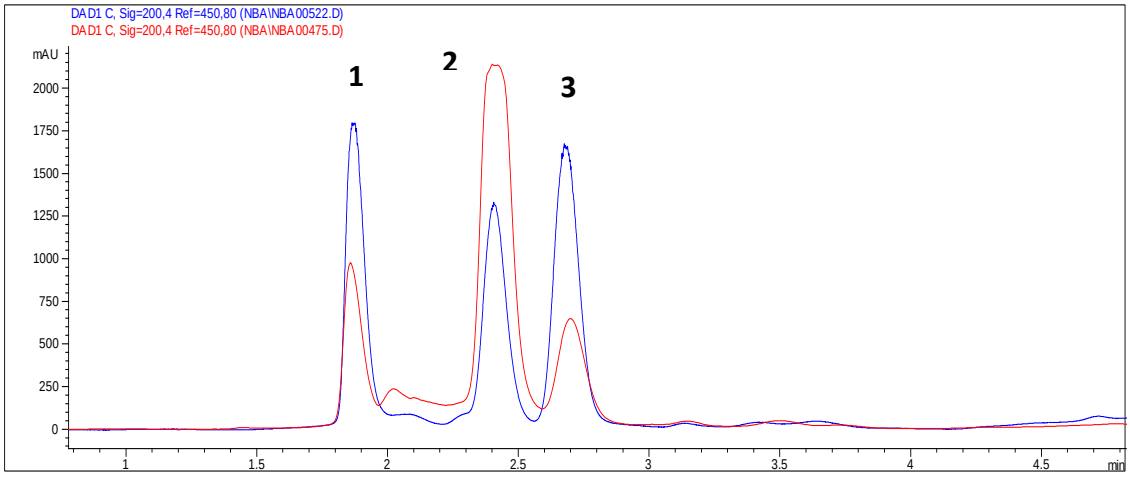

Fig. 43: RP-HPLC comparison between the reaction mixture at RT (red) and heating at 40°C (blue).

The hypothesis of the identity of peak 3 as NAM was also validated since a chloroform solution of TEA and ASAM, without norbiotinamine, heated at 40°C for 18h, did not show peak 3 (Fig. 44).

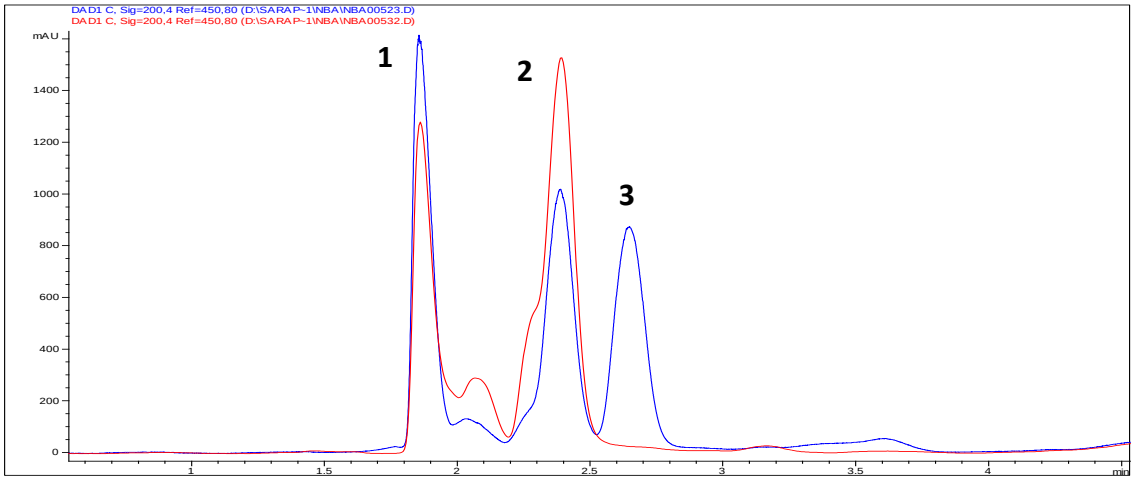

Fig. 44: Comparison between blank (red) and the reaction mixture in the presence of norbiotinamine (blue).

Finally, as shown in Fig. 45, the UV spectrum of peak 3 compound is very similar to the ASAM one.

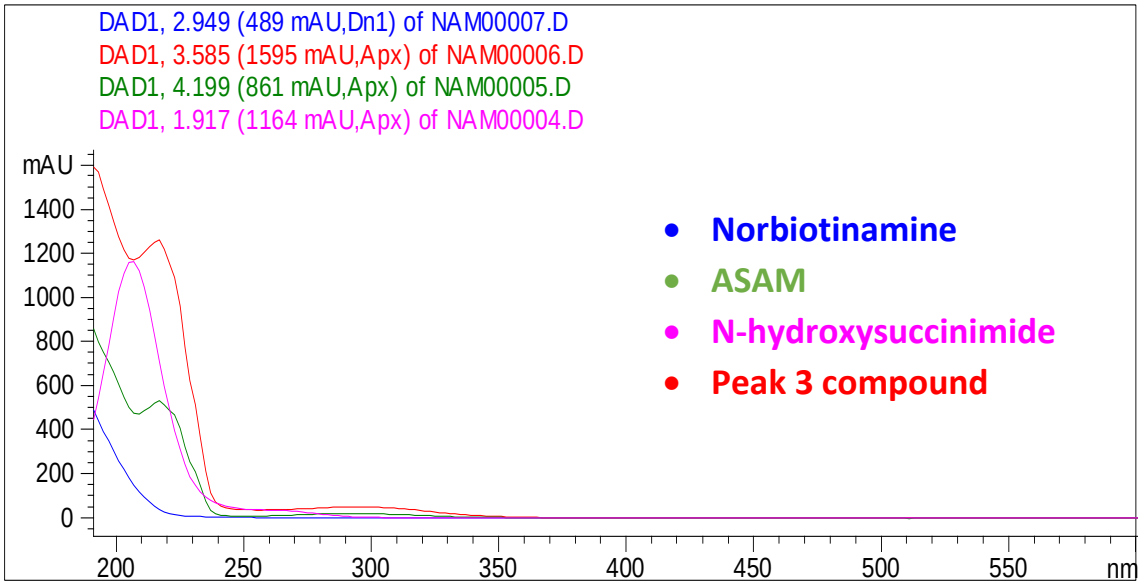

Fig. 45: Comparison between UV spectra of norbiotinamine, N-hydroxysuccinimide, ASAM and peak 3 compound.

For further evaluation, another RP-HPLC method, *H-NAM2*, was applied in order to improve peak resolution. Fig. 46 shows the analysis of the reaction mixture with the new RP-HPLC method and the peak assignment.

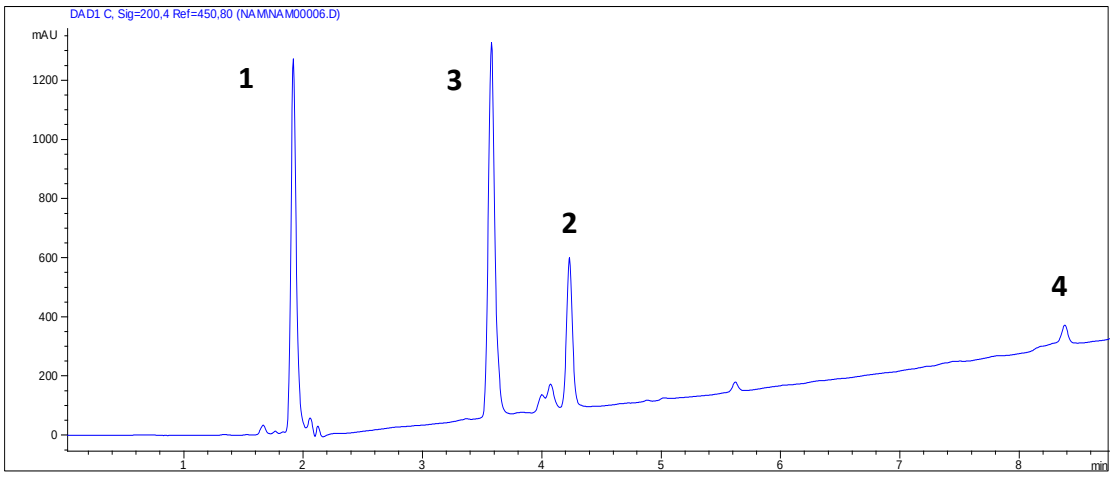

Fig. 46: Chromatogram of NAM reaction mixture analysed with H-NAM2 method.

For NAM purification, due to its solubility in water, 3 extractions with water/chloroform 1:1 were carried out to separate it from ASAM.

The aqueous phase containing N-hydroxysuccinimide and NAM was vacuum dried by Rotavapor and different solvents were tested to separate them.

Fig. 47 shows the comparison between the aqueous extract and the residues of washings, after drying and dissolution in the mobile phase.

Isopropanol and dichloromethane are able to solubilize both compounds, while toluene is too hydrophobic; N-hydroxysuccinimide has low solubility in diethylether, while NAM appears practically insoluble in this solvent.

Therefore, NAM was purified by repeated washings with ether and was obtained with a yield of 23% w/w. The elemental analysis confirmed its identity.

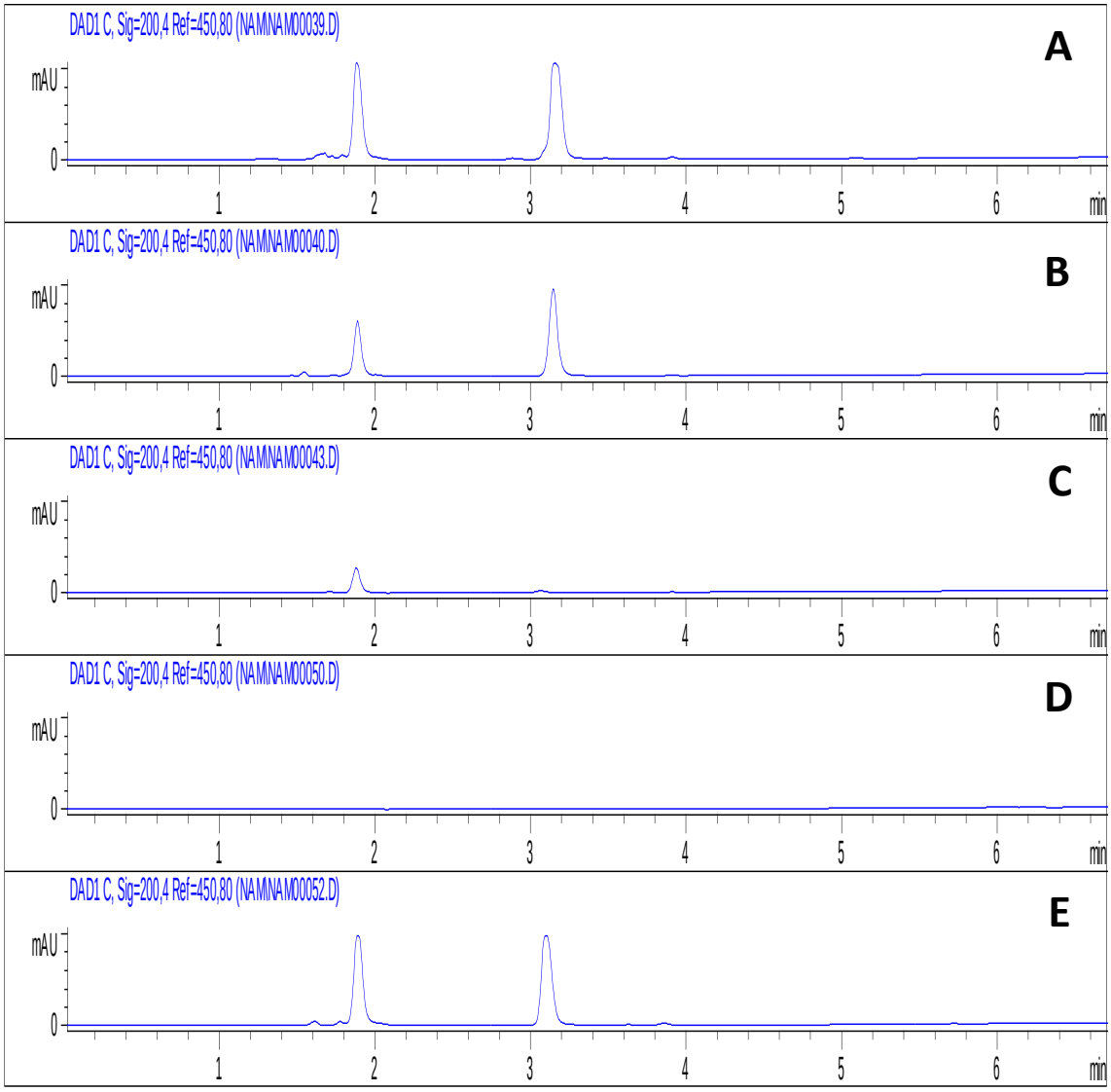

Fig. 47: RP-HPLC comparison between water extraction (A) and residues of washing with isopropanol (B), diethylether (C), toluene (D) and dichloromethane (E).

To improve the yield, the reactions conditions were modified.
Chloroform was replaced with acetonitrile, more able to solubilize norbiotinamine, and, after various attempts, the best yield was obtained by heating at 80°C for 24h.
In this case, the product precipitated by cooling the reaction mixture at -20°C for 48h and was purified from N-hydroxysuccinimide by four washings with diethylether.
The final yield was 60% w/w.

Characterization of NAM

The characterization was performed with elemental analysis, IR analysis, ^{1}H-NMR spectroscopy and RP-HPLC.

Elemental analysis

Elemental analysis on C, H, N and S was carried out in order to confirm the composition of the product. Table 3 shows the comparison between the theoretical percentage composition of NAM and the measured one.

Table 3: Theoretical and actual percentage composition of NAM.

	%C	%H	%N	%S
Theoretical	52.45	6.05	15.29	8.75
Actual	52.46	6.09	14.98	9.50

IR analysis

Fig. 48 shows the IR spectrum of NAM.
In the high frequency portion of the spectrum, it possible to observe the NH stretching of the secondary amides (3286 cm^{-1} and 3090 cm^{-1}), followed by methylene groups stretching (2928 $cm^{-1}$and 2856 cm^{-1}).
The most intense signal is the stretching C=O at 1703 cm^{-1}, which is related to the carbonyl of the maleimide.

This signal has a shoulder at 1680 cm^{-1}, which could be the signal of the C=O stretching of the biotin ureic cycle. The signal at 1638 cm^{-1} might be both C=O stretching and NH bending of the amide, since when these signals have similar frequencies they can turn out into one peak.

Finally, the IR spectrum of NAM shows peaks similar to the spectrum of ASAM, such as 828 cm^{-1} and 696 cm^{-1} signals, which may be related to the maleimidic CH.

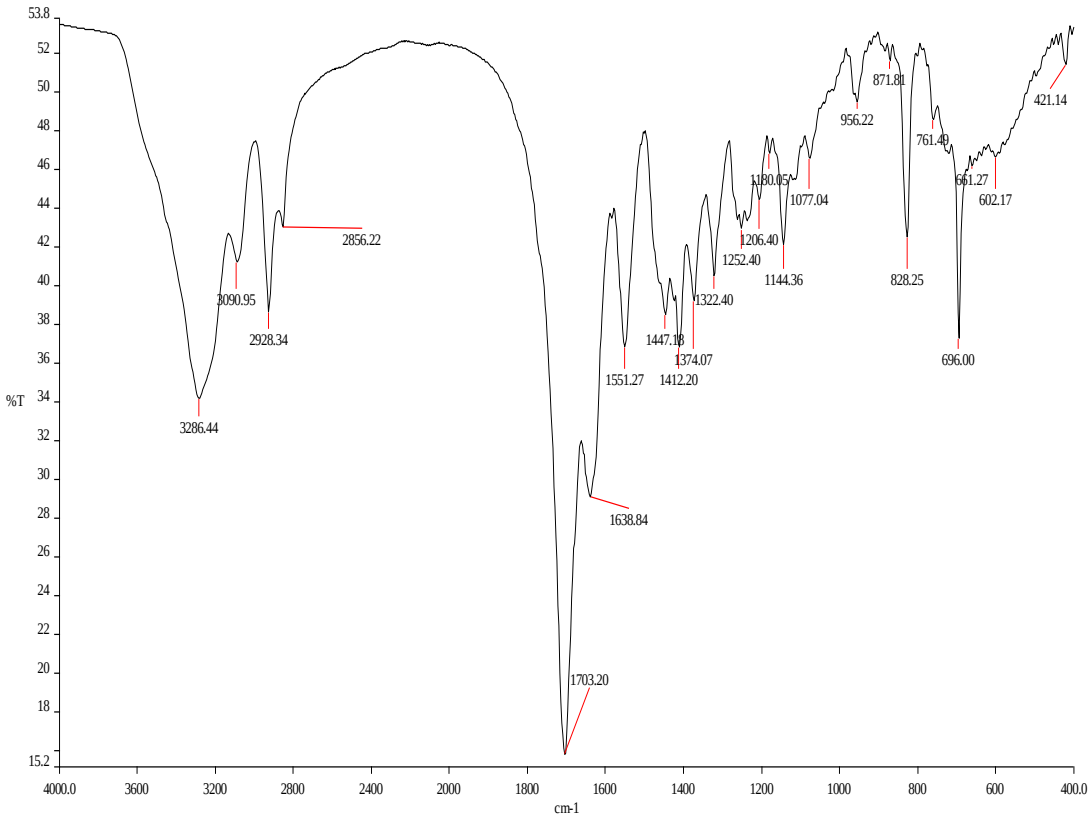

Fig. 48: IR spectrum of NAM.

^{1}H-NMR spectroscopy

^{1}H-NMR (Fig. 49) spectrum was acquired in DMSO-d_6 for the low solubility of NAM in chloroform, dichloromethane and methanol.

^{1}H-NMR (300 MHz, DMSO-d): δ 7.91 (1H, t, N**H**^{9}), 7.01 (2H, s, C**H**=C**H**^{12}), 6.40 (H, d, J=21.0 Hz, N**H**^{1}), 4.31 (1H, dd, C**H**^{2}), 4.13 (1H, dd, C**H**^{2}), 3.60 (2H, t, J=7.3 Hz, C**H**$_2^{11}$), 3.07 (1H, m, C**H**^{4}), 2.98 (2H, m, C**H**$_2^{8}$), 2.93 (1H,dd, J=5, 12.4 Hz, C**H**$_2^{3}$), 2.57 (1H, d, J=11.6 Hz, C**H**$_2^{3}$), 2.31 (2H, t, J=7.1 Hz, C**H**$_2^{10}$), 1.23-1.58 (6H, m, C**H**$_2^{5}$-C**H**$_2^{6}$- C**H**$_2^{7}$).

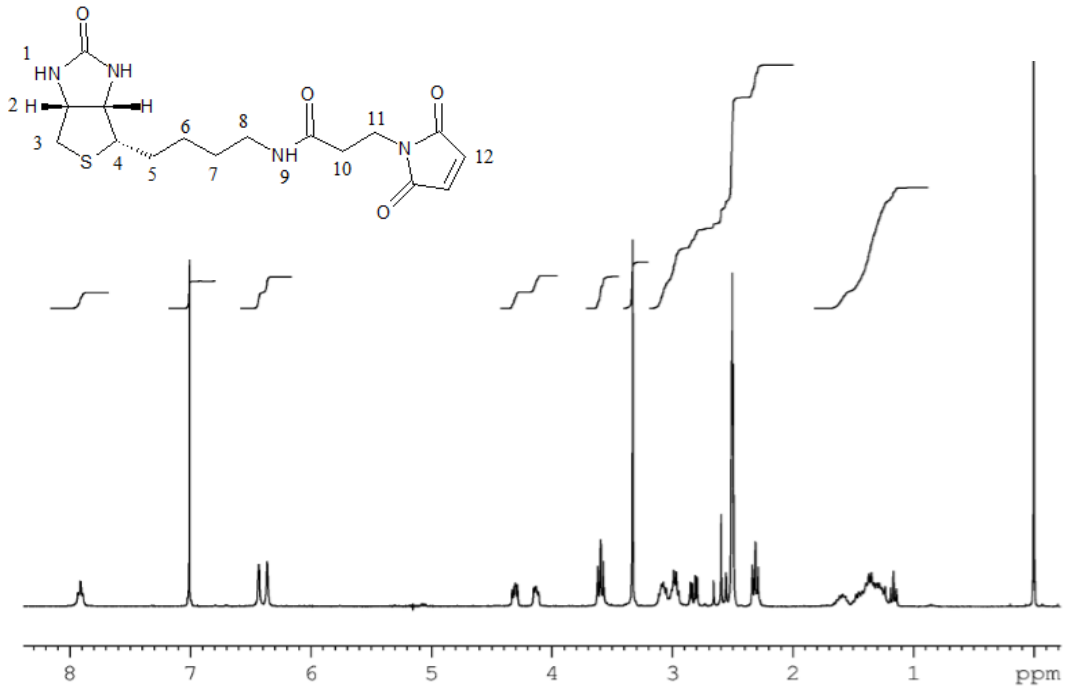

Fig. 49: ^{1}H-NMR spectrum of NAM.

The spin-spin decoupling was used for simplifying the spectrum and determining the positions of some protons in the molecule. The decoupling of the signal of the amidic NH proton (7.91 ppm) permitted to convert the multiplet at 2.98 ppm in a triplet, confirming the formation of the amide binding between ASAM and norbiotinamine.

The decoupling of the signal at 3.60 ppm, related to the CH_2^{11} protons, converted the triplet of CH_2^{10} into a singlet, showing the integrity of the structure of ASAM in the molecule.

Analytical RP-HPLC

NAM purity was analysed by RP-HPLC *H-NAM2* method (Fig. 50).

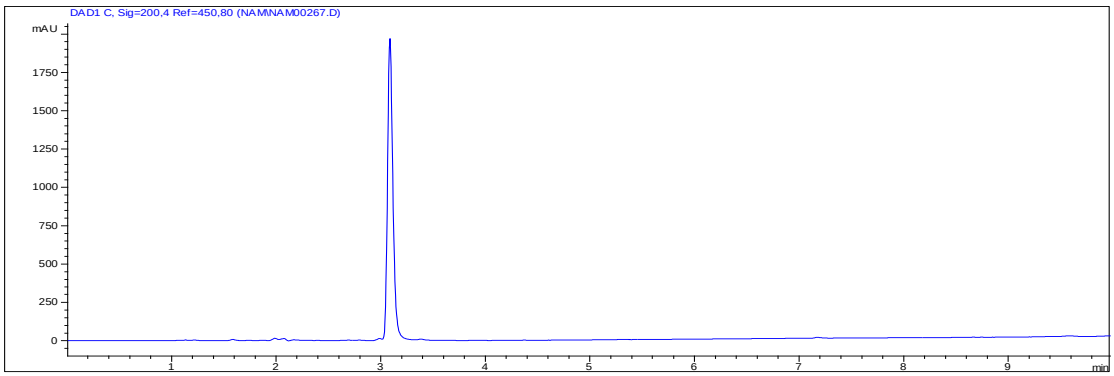

Fig. 50: RP-HPLC chromatogram of NAM after chromatographic purification.

Synthesis of NAMP

Most of the procedures reported in the literature for the conjugation of a maleimide with peptides by thioether linkage are carried out in a buffer at pH 7.0 - 7.5 (e.g. 10-100 mM phosphate, Tris or HEPES). In this pH range, the thiol group is sufficiently nucleophilic for reacting almost exclusively with the maleimide, even in the presence of a more prominent lysine amino group, which is protonated and relatively unreactive.

Usually, before coupling, the disulfide bonds of the peptide are reduced by a 10-fold molar excess of a reducing agent such as dithiothreitol (DTT) or tris-(2-carboxyethyl)phosphine hydrochloride (TCEP-HCl), for 2 hours, at room temperature.

Trialkylphosphines are powerful and selective reductants for disulfides, but, until recently, they have not been commonly used due to their being malodorous and/or water insoluble. The commercial availability of TCEP-HCl, which is odorless and water-soluble, makes this reagent safe and convenient to use [44].

TCEP-HCl is a strong reducing agent that reduces even very stable alkyl disulfides, rapidly and cleanly in water, at room temperature and pH 5 [45].

The TCEP-HCl pKa is 7−8, which is a common pH range for performing bioconjugations, and, as such, the trialkylphosphines are more-effective nucleophiles than thiol-based reducing agents to effect reduction within this pH range.

Furthermore, disulfide reduction utilizing alkylphosphines are irreversible and driven by phosphorus−oxygen bond formation, unlike the reversible mechanism of disulfide reduction observed with thiol-containing reducing agents [46].

In addition, TCEP has been advertised as being less reactive then DTT with thiol-reactive compounds, thereby eliminating the need to remove it before labeling [47].

For this reasons, initially it was decided to perform the reaction between the maleimide of NAM and the thiol group of the VCAM-1 binding peptide cysteine in phosphate buffer, at pH 7 and in the presence of TCEP, without removing it from the reaction mixture (Fig. 51).

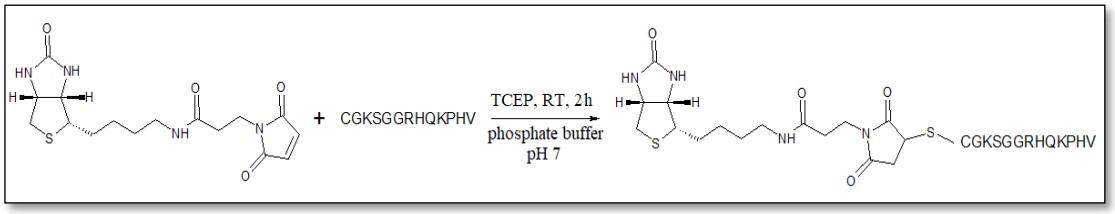

Fig. 51: Conditions for NAMP synthesis.

The reaction mixture was analysed by RP-HPLC, using the *H-NAMP1* method (Fig. 52).

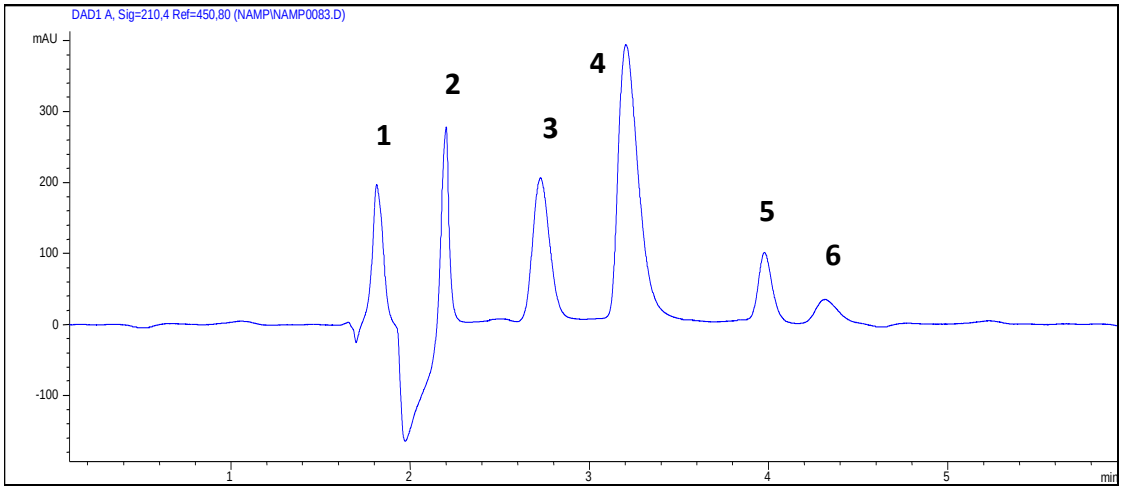

Fig. 52: Chromatogram of NAMP reaction mixture analysed by H-NAMP1 method.

Peaks 1-2 are related to the phosphate buffer, although traces of peptide could co-elute with peak 2, as shown in Fig. 53.

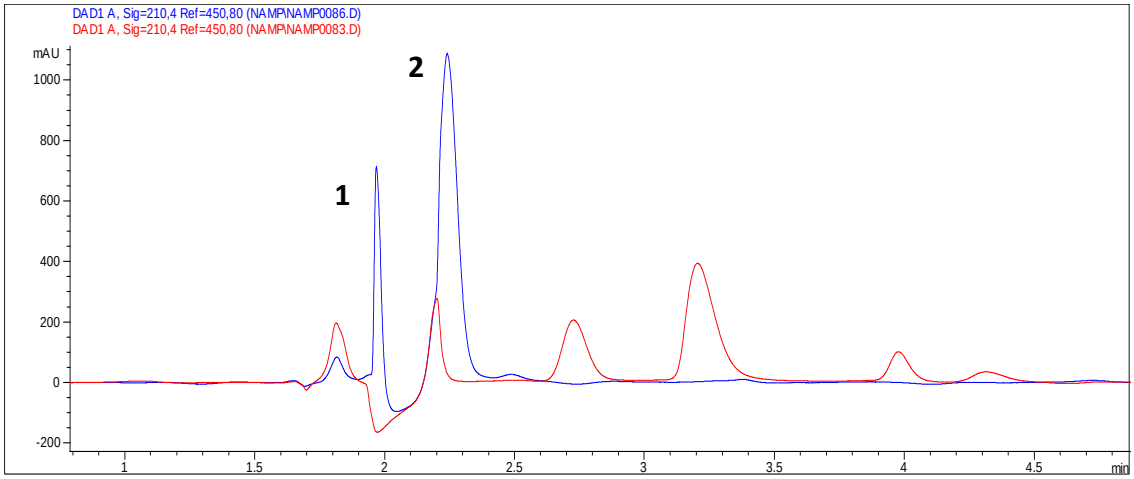

Fig. 53: RP-HPLC comparison between reaction mixture (red) and a solution of peptide in phosphate buffer (blue).

Peaks 5 and 6 are related to NAM, in particular the first peak forms also in a mixture including NAM and TCEP (Fig. 54), while the second peak is a NAM derivative that forms in phosphate buffer over time (Fig. 55).

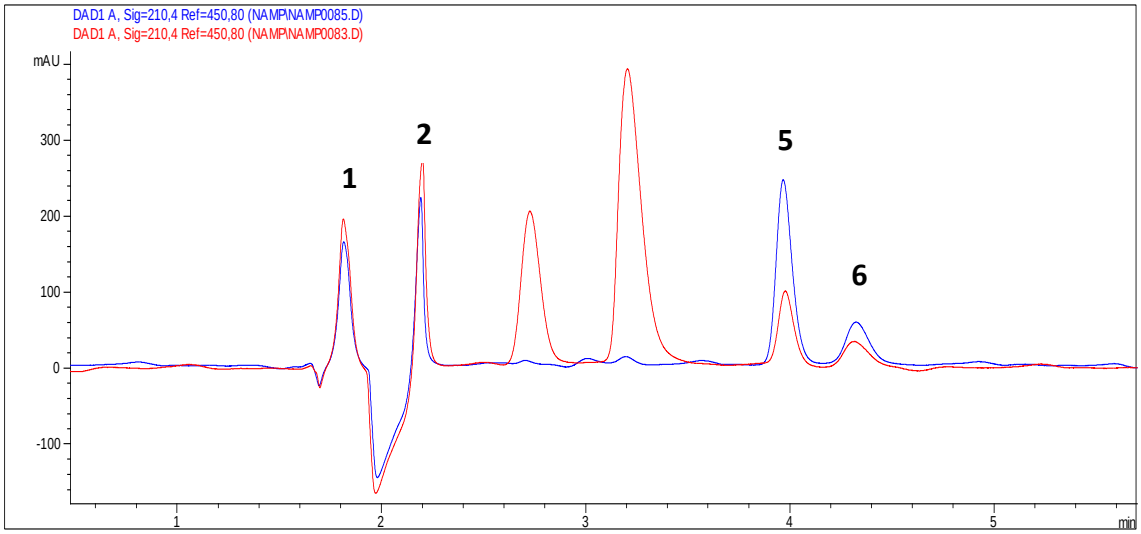

Fig. 54: RP-HPLC comparison between the reaction mixture (red) and a solution including NAM and TCEP (blue).

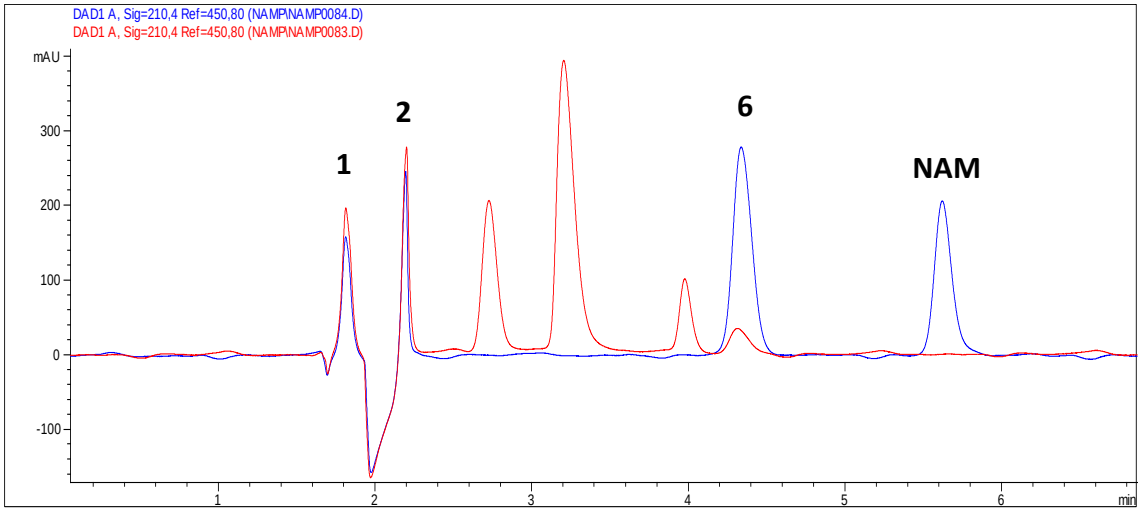

Fig. 55: RP-HPLC comparison between the reaction mixture (red) and NAM in phosphate buffer (blue).

Peak 3 shows a behaviour similar to peak 6 and seems to be related to peak 4: it increases over time in phosphate buffer, while peak 4 decreases.

Assuming that peak 4 could be NAMP, peaks 3 was supposed to be the hydrolysed maleimidic derivative of NAMP in accordance with a work published by D. Fontaine et al. in 2015 [48].

In this article, the mechanism of Michael-addition reaction of a thiol to a maleimide is explained (Fig. 56).
Briefly, maleimide−thiol conjugates form through Michael addition of a thiolate (RS^-) to the double bond of the maleimide to produce a succinimidyl thioether (SITE).
The retro-Michael reaction converts the thioether adduct back to the starting thiol and maleimide, but in the absence of excess thiols the dissociated products simply reconjugate and the adduct is, for practical purposes, considered stable.
However, in the presence of excess exogenous thiolate ($R'S^-$), as in most biological environments, a new conjugate forms with the exogenous thiol and, for practical purposes, the original SITE considered to be irreversibly cleaved.
In addition to the retro-Michael reaction, the succinimidyl moiety of a SITE undergoes irreversible hydrolysis to provide two isomeric succinamic acid thioethers (SATE). Thus, in the presence of excess thiol, a particular SITE is destined to undergo irreversible thiol exchange and/or hydrolysis to a SATE.
In contrast to SITEs, hydrolysed SATEs do not readily undergo thiol loss. Indeed, in contrast to the instability caused by thiol exchange, the stability of SITE adducts of certain cysteine residues of mAbs is due to ring opening.
Thus, one strategy to stabilize maleimide−thiol conjugates is to intentionally hydrolyse the conjugate prior to its exposure to exogenous thiol.

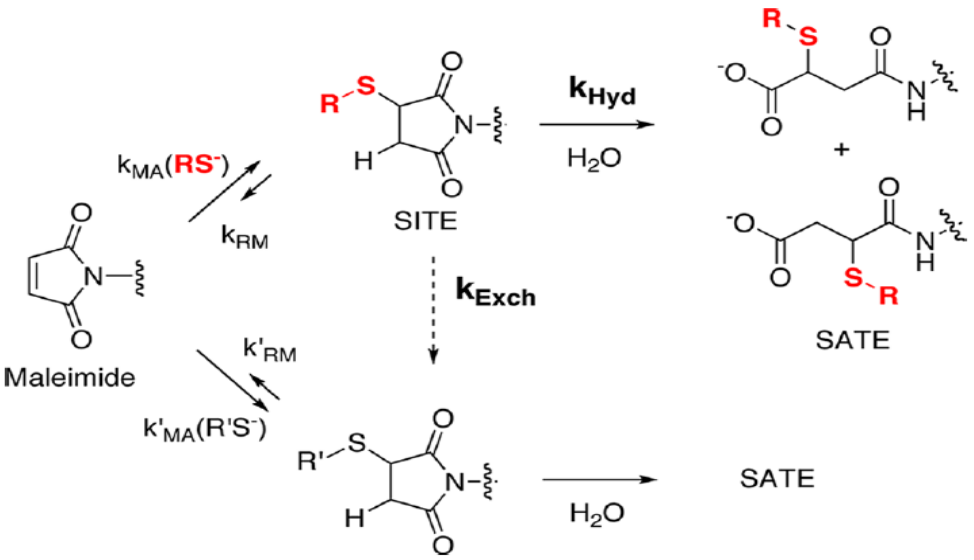

Fig. 56: Michael-addition mechanism scheme of a thiol to a maleimide.

Peaks 4 and 3 were isolated by semi-preparative RP-HPLC and characterized by mass spectrometry, which confirmed that they corresponded to NAMP and to its hydrolysed derivative respectively. It was not possible to calculate an accurate yield of the synthesis, because the reaction was carried out using a very small amount of peptide (about 1 mg at a time), for its prohibitive cost.

In fact, to avoid losses of material, the quantity of peptide used for the reaction was not weighed, but it was assumed on the basis of the amount dispensed by the producer.

For the same reason, it was not possible to calculate the amount of pure product by the weight difference with the vial in which the fractions collected by semi-preparative RP-HPLC were dried.

The reaction conditions were modified to improve the reaction yield as inferred by peak 4 area. The first possible change was not to incubate the peptide with TCEP before the coupling reaction with the maleimide. To verify the necessity of using a reducing agent to decompose the dipeptide possibly deriving from the formation of disulphide-bond between two cysteines, the peptide, dissolved in phosphate buffer, was analysed by RP-HPLC. Since applying *N-NAMP1* method the peptide co-elutes with the phosphate buffer, *N-NAMP2* method was used, as suggested by the manufacturer (Innovagen).

No dipeptide was detected, but when the analysis was repeated after 24h a second peak, with higher tR, appeared; this phenomenon did not occur when the peptide was dissolved in water.

Fig. 57 shows a comparison between the peptide dissolved in water and in phosphate buffer, analysed after 24h.

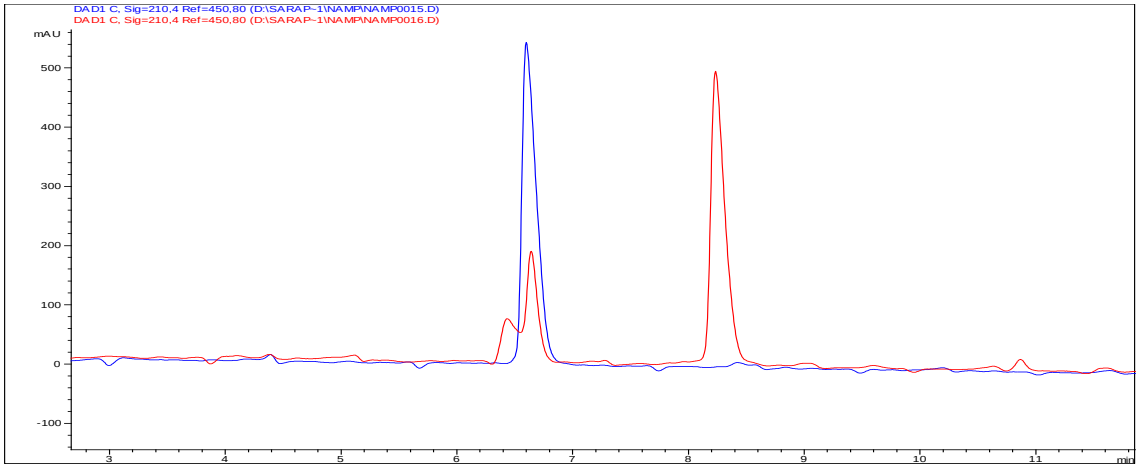

Fig. 57: RP-HPLC comparison between peptide solubilised in water (blue) and in phosphate buffer (red), after 24h.

For establishing that the second peak, forming in phosphate buffer, was the dipeptide, TCEP was added to the solution. In this condition, the second peak disappeared and the first peak increased (Fig. 58). Since the dipeptide forms only under specific conditions and is not detectable at the beginning of the reaction, TCEP resulted to be not strictly necessary.

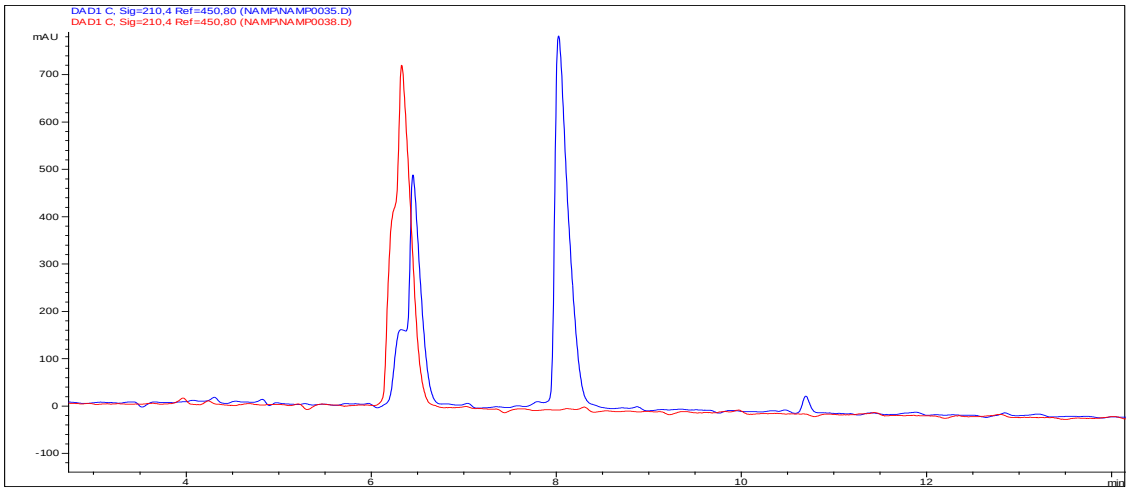

Fig. 58: RP-HPLC comparison between peptide in phosphate buffer before (blue) and after TCEP addition (red).

Furthermore, TCEP was not added to the reaction mixture in accordance to recent works that assert that it would lead to the formation of secondary products, by reacting with the maleimide [44, 46, 49, 50].

Many papers have reported decreased yields of conjugation when using maleimide in the presence of TCEP, suggesting a possible interaction between the two reagents [46].

Tyagarajan et al. [49] showed that protein alkylation by both iodoacetamide and maleimide dyes is reduced with increasing concentrations of TCEP and that the reactive dye molecule forms a new species by interaction with TCEP. So this work suggested to remove reducing agents prior to alkylation or to use enough dye to overcome the competition from the reducer.

In a work published by Kantner et al. [46], the treatment of TCEP with a solution of N-ethylmaleimide (pH 7, phosphate buffer) at room temperature resulted in the rapid formation of a TCEP−maleimide adduct, which can be represented in either the ylene or ylide resonance forms (Fig. 59).

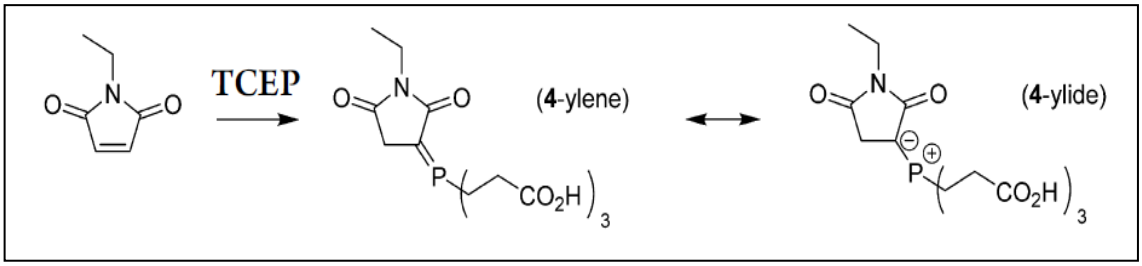

Fig. 59: Scheme of reaction of N-ethylmaleimide with TCEP.

For these reasons, the synthesis of NAMP was repeated without TCEP: as a result, the compound corresponding to peak 5 did not form and the area of NAMP peak increased (Fig. 60).

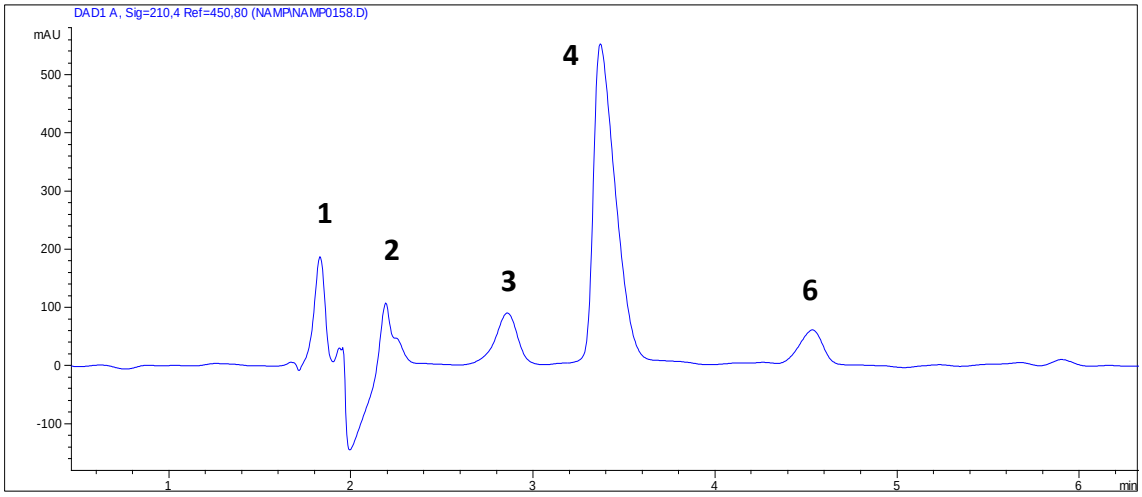

Fig. 60: RP-HPLC chromatogram of NAMP reaction mixture in phosphate buffer without TCEP.

Finally, in order to further increase the yield, the reaction was repeated in ultrapure water at pH 5-6 (this value allows to keep the selectivity of the nucleophilic attack of the thiol group on the maleimide), in presence of an excess of NAM. Furthermore, the reaction temperature was increased to 37°C and the time prolonged from 2h to 24h.

Under these conditions, a reaction mixture including only NAMP and NAM, with complete peptide consumption, was obtained (Fig. 61) and from the total moles of NAM used as reagent and by the amount of unreacted NAM in the final mixture, the moles of the product were estimated.

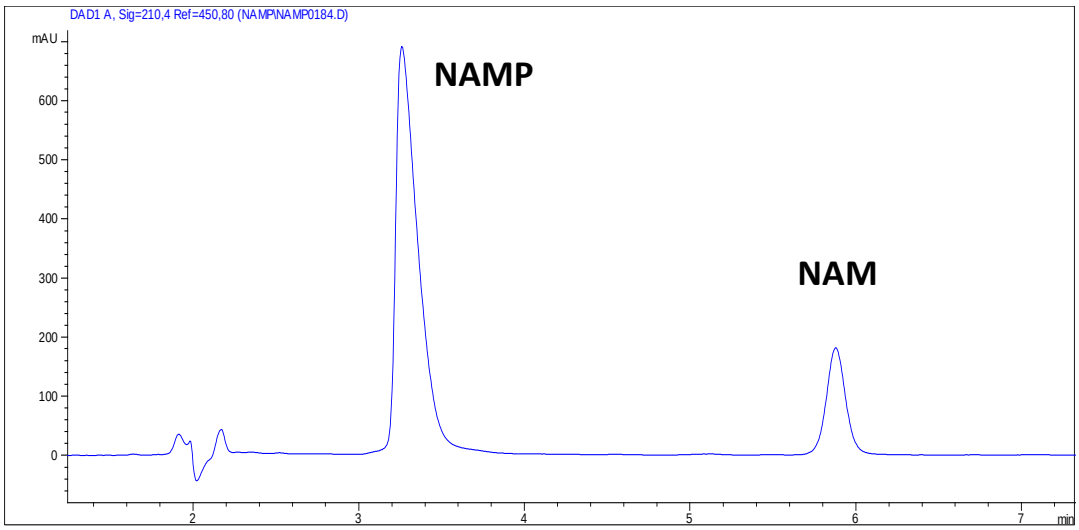

Fig. 61: RP-HPLC chromatogram of NAMP reaction mixture in ultrapure water.

Characterization of NAMP

NAMP characterization was performed by mass spectrometry, using the LTQ Orbitrap Velos Pro. The LTQ Orbitrap is a high-performance LC-MS and MSn system, combining rapid LTQ ion trap data acquisition with high mass accuracy Orbitrap mass analysis.

It permitted to confirm the structure of the new radiopharmaceutical, highlighting the formation of a thioether binding between the peptide and NAM.

Fig. 62 shows the mass spectrum of the purified molecule. The measured mass coincides with the calculated monoisotopic mass.

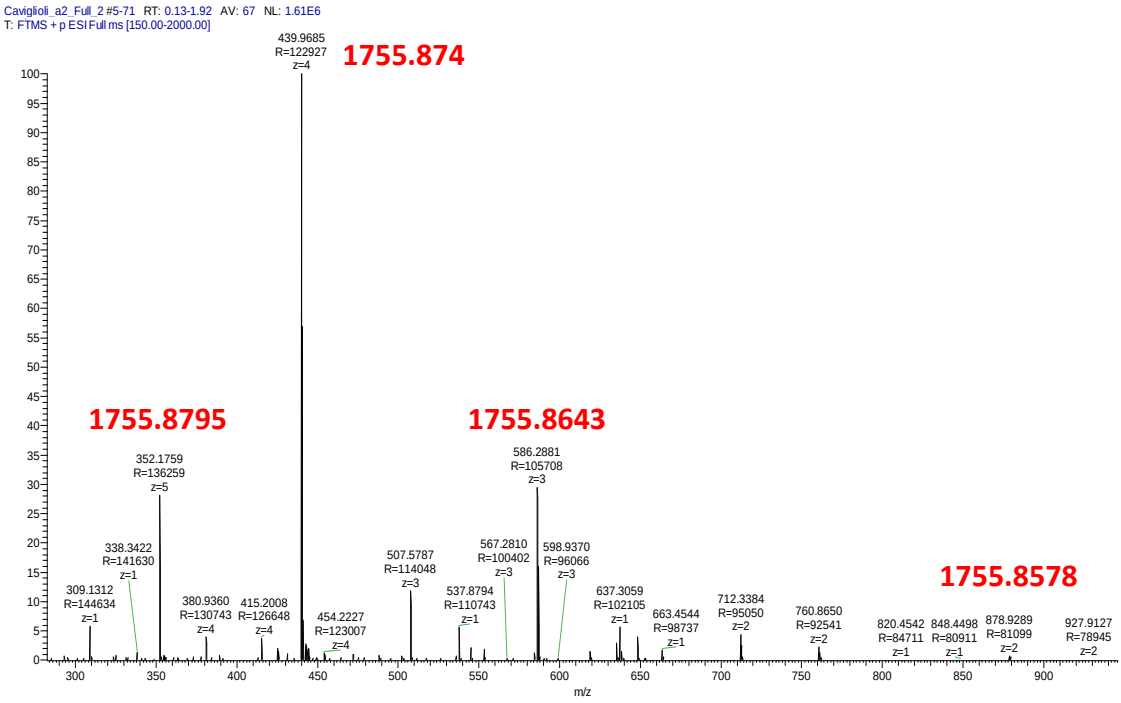

Fig. 62: Mass spectrum of NAMP.

By the fragmentation in MS^2 of the peak with m/z of 439.97 and the fragmentation in MS^3 of the peak with m/z of 507.58, it was possible to identify the fragment ion types that are produced by cleavage of different bonds along the peptide backbone.

The fragmentations are described following the specific nomenclature [51, 52]: cleavage of the backbone typically occurs at the peptide amide bond to produce b ions, if the amino terminal fragment retains the charge; y ions, if the carboxy-terminal fragment retains the charge.

The y series is sometimes accompanied by peaks formally corresponding to loss of NH_3 from the y ions if the fragment includes arginine, asparagine, lysine or glutamine as aminoacids, or loss of H_2O from y ions if the fragment includes serine, threonine, glutamic acid or aspartic acid.

In Fig. 63, the fragmentation in MS^3 shows the following ions:

- y10, related to the loss of valine, histidine and proline;
- y9, for the cleavage of the 4 terminal aminoacids and the related ions that lost NH_3 and successively H_2O;
- y8, related to the further loss of glutamine;
- y7, for the cleavage of the amidic binding between arginine and histidine;
- y2, in which only cystein and glycine remained. The y2 ion permitted to confirm that the peptide conjugated the maleimide by the thiol group of the cysteine.

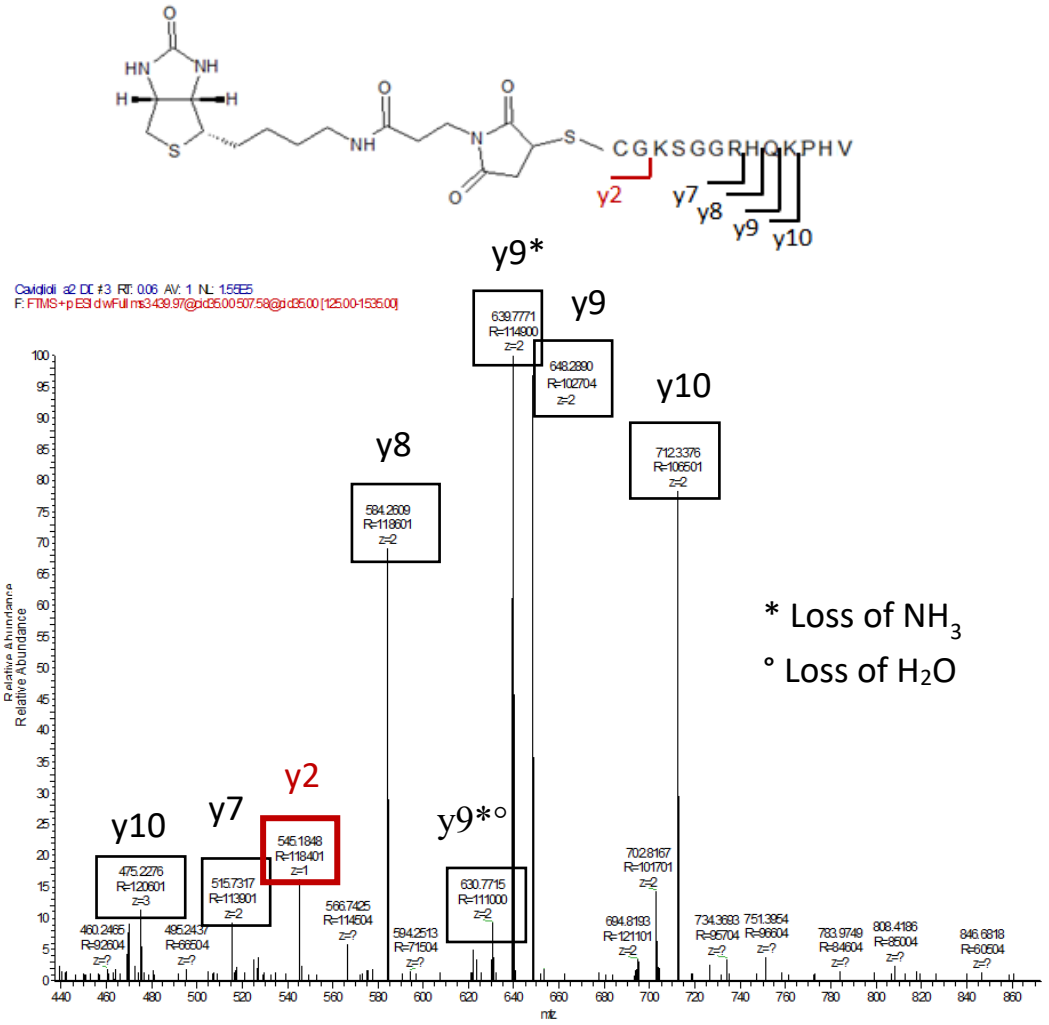

Fig. 63: MS^3 spectrum of the peak with m/z of 507.58.

By mass spectrometry, the two isomeric derivatives of NAMP got by hydrolysis of the maleimide have been identified (Fig. 64). In fact, the calculated monoisotopic mass of this substance (M_{mi} = 1773.8515) coincides with the measured value (Fig. 65). By fragmentation in MS^2 of the peak with m/z 592.29, it was possible to detect the y ions, deriving from the cleavage of different bonds along the peptide backbone.

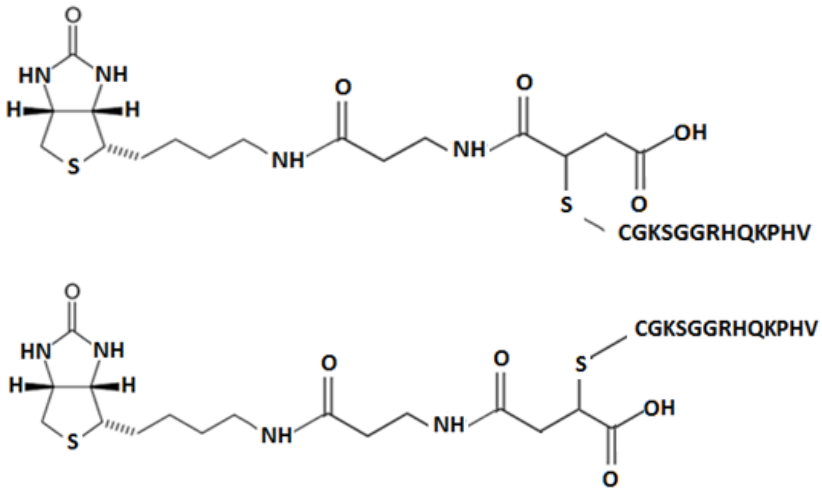

Fig. 64: The two isomeric forms of succinamic acid thioethers of NAMP.

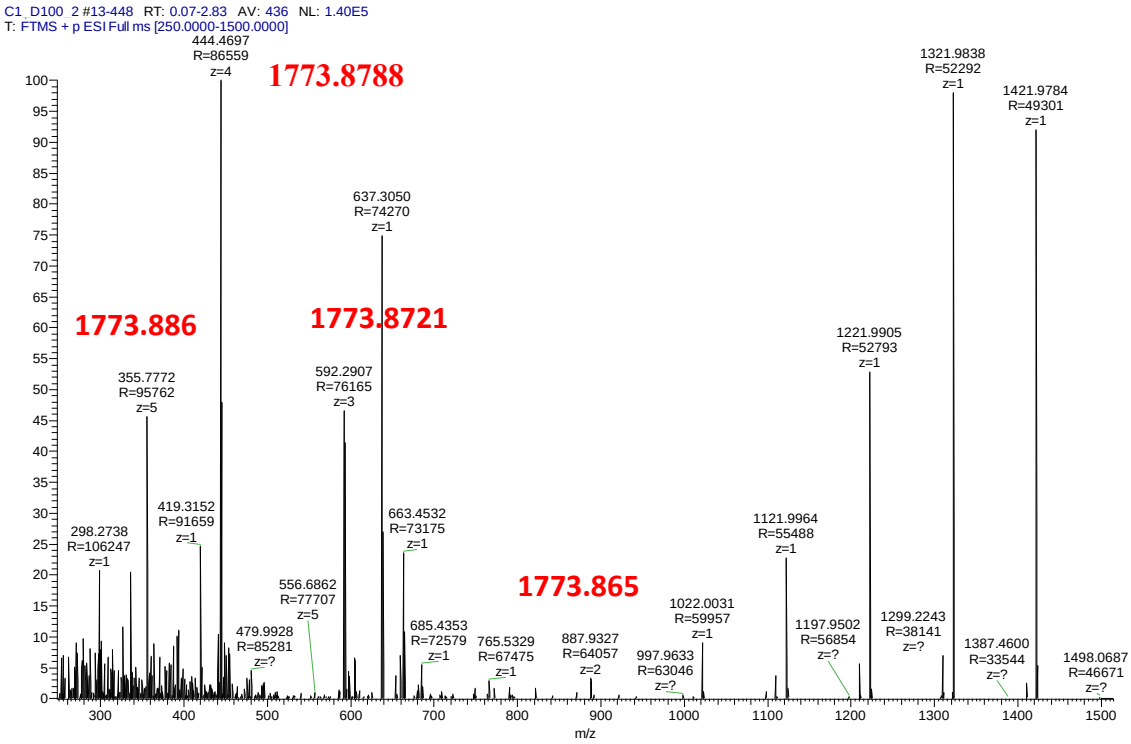

Fig. 65: Mass spectrum of NAMP derivative.

CONCLUSION

A biotin derivative potentially stable *in vivo* has been conjugated with a peptide able to bind VCAM-1, in order to exploit the avidin-biotin binding for the pretargeting of early stage atherosclerotic plaques.

While the synthesis of the linker between the peptide and the biotin derivative was performed by following a reported reaction, for the preparation of norbiotinamine the reaction conditions described in the literature were modified to increase the yield and reduce secondary products formation.

The product of conjugation between the linker and norbiotinamine was successfully obtained and purified and the final product, NAMP, was prepared in a sufficient amount with acceptable purity.

A biotin derivative (NBA I2a) has also been synthesized for which no articles have been published in the literature yet, therefore more in-depth analysis will be carried out in order to confirm its identity and to evaluate its possible innovative biological activity.

Finally, the hydrolysed maleimidic derivative of NAMP has been identified, which might potentially bind VCAM-1 better, including a longer spacer between the biotin derivative and the peptide and might be more stable *in vivo*. To explore these aspects, further analysis will be performed.

3.CHAPTER 2

Synthesis and characterization of MacroP

INTRODUCTION

Radiopharmaceuticals are drugs containing a radionuclide, used routinely in nuclear medicine for the diagnosis or therapy of various diseases.

In the last decades, the direction of research in this area has been shifted towards target-specific radiopharmaceuticals based on receptor binding of a radiolabeled receptor ligand in the diseased tissue [53].

A receptor ligand, often termed as ‘‘targeting biomolecule’’ (BM), serves as the ‘‘vehicle’’ to carry the radionuclide to the diseased tissue, which is known to contain a substantial concentration of the target receptor.

Accumulation of the radiotracer at diseased tissues relies on the localization of the radiolabeled receptor ligand that binds to receptors with high affinity and specificity.

The high specificity of receptor binding results in selective uptake and distribution of the radiolabeled receptor ligand at diseased tissues. This high receptor binding affinity and specificity makes receptor imaging (often called ‘‘molecular imaging’’) advantageous over traditional scintigraphic imaging using simple technetium complexing radiopharmaceuticals or other imaging modalities such as X-ray computed tomography (CT), ultrasound (US), and nuclear magnetic resonance imaging (MRI) [53].

The BMs can be small molecules, peptides, monoclonal antibodies (mAbs), or mAb fragments, and, ideally, their affinity for the biological target should be unchanged after radiometal labeling [54].

The most convenient approach to bind a radionuclide to a BM durably is to use a suitable bifunctional chelate (BFC), which is simply a chelator with reactive functional groups that can be covalently coupled to the BM, forming a stable conjugation [54,55] (Fig. 66).

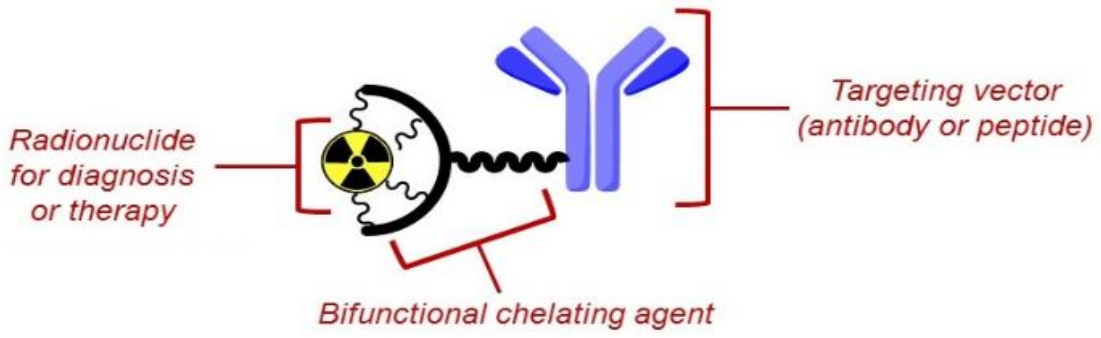

Fig. 66: Radiopharmaceutical scheme using the BFC approach.

Common bioconjugation techniques utilize functional groups such as carboxylic acids or activated esters (e.g. N-hydroxysuccinimide NHS-ester, tetrafluorophenyl TFP-ester) for amide couplings, isothiocyanates for thiourea couplings, and maleimides for thiol couplings [55]. Active groups are either naturally present (e.g., $–NH_2$, –SH, etc.) in BMs or are synthetically introduced (e.g., $–N_3$, –C≡CH, etc.) into them [54].

There are several requirements for an ideal BFC [53]. The choice of an appropriate BFC is largely determined by the oxidation state of the radiometal and its affinity for the chelator donor atoms in order to form a metal chelate with high thermodynamic stability and kinetic inertness, and consequently to keep the metal chelate intact under physiological conditions [53, 54]. Decomposition of the metal chelate produces free metal ions, which may deposit on the bone and cause bone marrow toxicity.

The uptake of a radiopharmaceutical depends not only on the receptor binding affinity of the biomolecule, but also on the pharmacokinetics, which are determined by the physical and chemical properties of both biomolecule and metal chelate.

In the blood stream, the concentration of radiopharmaceuticals may become so low that the natural chelators present in the blood (e.g., transferrin or other metal-binding enzymes) will cause the dissociation of the radiometal from its metal-chelate, resulting in the possible accumulation of radioactivity in non-target organs (radiation toxicity) [54].

The BFC should have high hydrophilicity to improve blood clearance and renal excretion of the labeled and unlabeled BFC–BM conjugate. Fast renal clearance of unlabeled BFC–BM will minimize its competition with the radiolabeled BFC–BM for receptors.

In addition, the BFC should withstand radiolysis, because a large dose of radiation can produce free radicals and result in a significant amount of decomposition of the metal chelate during the manufacturing process and transportation.

The most common way to increase the thermodynamic stability and kinetic inertness of a metal complex is to use a polydentate chelator [53].

The denticity requirement of a BFC is largely dependent on the size and coordination geometry preference of the metal ion, which must be thermodynamically stable to transchelation by these natural chelators.

Common bifunctional chelating groups for radiometals are illustrated in Fig. 67.

A linker is often used to keep the radiometal chelate away from the targeting BM to minimize structural variations (shape and size) of the latter.

Furthermore, a linker could facilitate radiopharmaceutical pharmacokinetics, including distribution and elimination [54].

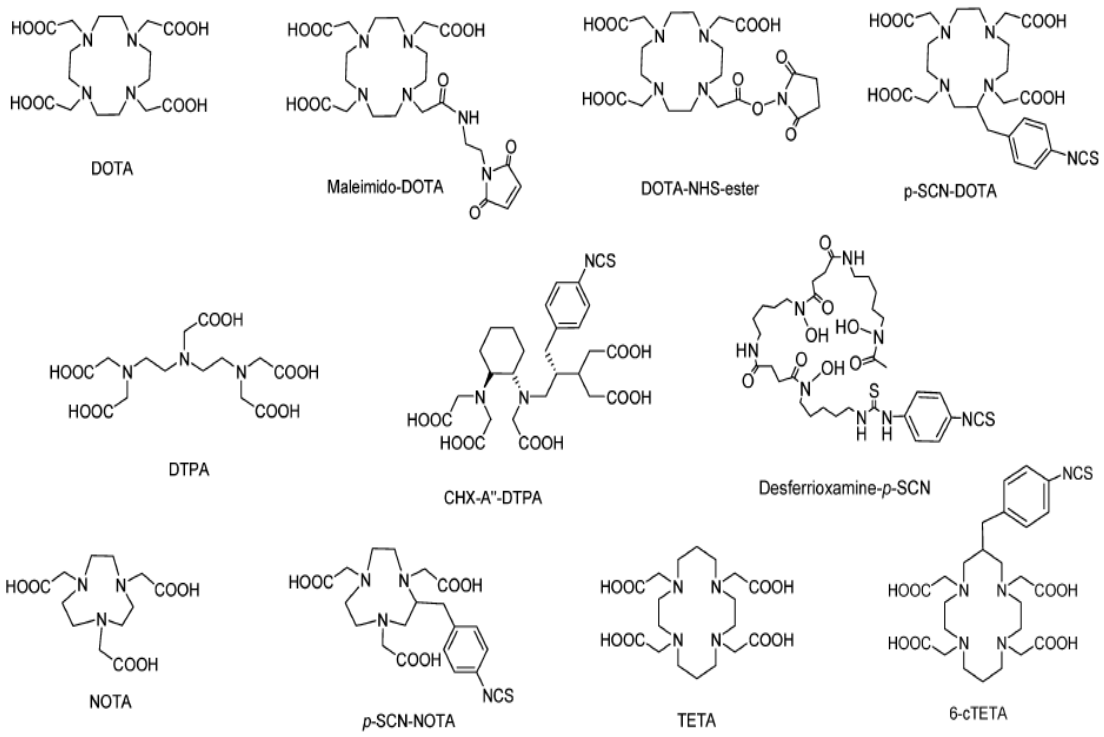

Fig. 67: Common bifunctional chelating agents for radiometals.

Macrocyclic BFC (as DOTA, NOTA and TETA) form metal complexes with high thermodynamic stability and kinetic inertness.

The pKa values of the carboxylic groups in these molecules are in the appropriate range 2–5, as lower pKa values result in less competition from the protons, high stability of the metal complex and minimum acid-assisted demetallation.

Besides, the acetate groups attached to the nitrogen donor atoms have low molecular weight, therefore the contribution of the BFC to the overall molecular weight of the BFC–BM conjugate is minimized.

The high hydrophilicity of acetate chelating arms will favour faster blood clearance and result in reduced competition between the labeled and unlabeled BFC–BM [53].

Furthermore, macrocyclic chelators require minimal physical manipulation during metal ion coordination, as they possess inherently constrained geometries and partially pre-organized metal ion binding sites, thereby decreasing the entropic loss experienced upon metal ion coordination. In contrast, acyclic chelators (as DTPA) must undergo a more drastic change in physical orientation and geometry in solution in order to arrange donor atoms to coordinate with a metal ion, and subsequently they suffer a more significant decrease in entropy (thermodynamically unfavourable) than macrocycles do. The entropic driving force for complex formation is therefore greater for macrocycles in general, a phenomenon referred to as the macrocycle effect [55].

In contrast, a major advantage of using DTPA analogues as BFCs is their extremely high radiolabeling efficiency (fast and high yield radiolabeling) under mild conditions.

The ability to quantitatively radiolabel/coordinate a radiometal in less than 15 minutes at room temperature is a common property of acyclic chelators, whereas the radiolabeling kinetics of DOTA-based BFCs is usually slow, and much more dependent on the radiolabeling conditions, including DOTA-conjugate concentration, pH, reaction temperature and heating time, buffer agent and buffer concentration, and presence of other metal ions, such as Fe^{3+} and Zn^{2+} [53, 55].

Heating at elevated temperatures is often needed for successful radiolabeling of DOTA-conjugated biomolecules. For small peptides, radiolabeling at elevated temperatures may not cause any significant degradation of radiolabeled DOTA-bioconjugates; for monoclonal antibodies, however, radiolabeling at elevated temperatures often causes a significant loss of immunoreactivity of the radiolabeled bioconjugates [53].

The advantage of using DOTA analogues as BFCs is the extremely high kinetic inertness of their metal chelates; conversely, the kinetic lability of metal acyclic chelates often results in dissociation of the radiometal from the metal chelate, and leads to radiation toxicity to non-target organs, such as bone marrow [53].

In this chapter, the synthesis and characterization of a radiopharmaceutical, MacroP, performed during the third year of my PhD will be discussed.

MacroP includes the maleimido-monoamide DOTA, a DOTA derivative with a maleimide moiety exploitable for conjugation reaction with thiol groups of peptides and proteins and able to chelate several radionuclides for the acquisition of diagnostic images.

It was directly conjugated with the cysteine of the VCAM-1 binding peptide, in order to detect early stage atherosclerotic lesions (Fig. 68).

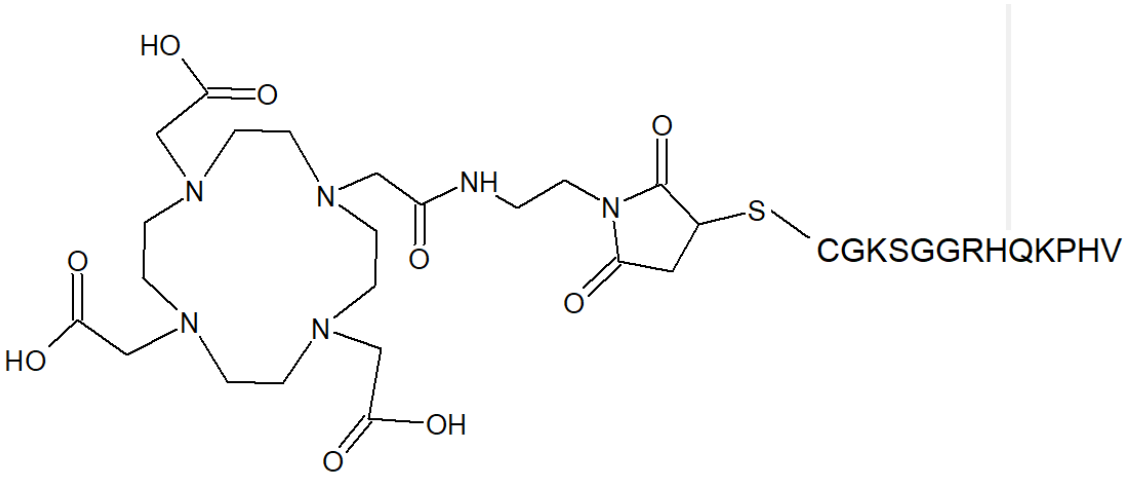

Fig. 68: MacroP structure.

MATERIALS AND METHODS

Materials

Ammonium acetate ($AcONH_4$) (Merck); arsenazo III (Sigma-Aldrich); maleimido-monoamide-DOTA (MMA-DOTA) (Macrocyclics); phosphate buffer pH 2.5 and pH 7 for HPCE; TraceCERT®, Lead standard for AAS (Pb) (Sigma-Aldrich); trifluoroacetic acid (TFA) (Merck); VCAM-1 binding peptide (Innovagen). All chemicals were used as received, without further purification. The water used was purified with a Milli-Q system from Millipore.

Instruments

De Lama SteriPlus bench steam sterilizer; Hewlett Packard Series II 1090 liquid chromatograph; LTQ Orbitrap Velos Pro; Mettler Toledo Quattro MP220 Basic pHmeter; Mettler Toledo XS3DU electronic microbalance; EchoTherm™ SC25XT Torrey-Pines Scientific orbital mixing dry bath; Scaltec SBC 21 electronic analytical balance; Hewlett-Packard HP 8453 UV-Vis spectrophotometer; Waters 1525 binary pump HPLC; Waters 2992 photodiode array detector; Waters fraction collector III.

Methods

Synthesis of MacroP

In a 1.5 mL polypropylene tube, 1.13 mg of MMA-DOTA (1.4 μmol) were dissolved in 500 μL of ultrapure water. 1 mg of peptide (0.72 μmol) was solubilised in 500 μL of ultrapure water and added to the MMA-DOTA solution. The reaction was heated at 37°C, under orbital shaking at 400 rpm for 48h, in atmosphere of nitrogen.

Sterilization of reactions materials

The sterilization of the materials used for MacroP reactions was performed in autoclave at 120° under saturated steam pressure of 98 kPa over atmospheric pressure, for 30 minutes.

Analytical reversed-phase high-performance liquid chromatography (Analytical RP-HPLC)

Analytical RP-HPLC was performed on Hewlett Packard Series II 1090 with a UV-visible detector.

The analyses of the HPLC data were conducted on Hewlett-Packard HPLC ChemStation software. Reverse-phase HPLC chromatography was carried out using a RP 18, Waters X-Bridge C18, 3.5 µm, 4.6 x 150 mm and a Waters X-Bridge BEH C18 Sentry Guard Cartridge 3.5 µm, 4.6 x 20 mm.

Analysis of MacroP

For the analysis of the reaction mixture and the determination of MacroP purity, a RP-HPLC method was applied using a gradient solvent system at a flow rate of 1 mL/min. The gradient mixture was composed of 0.1% aqueous TFA (solvent A) and acetonitrile gradient grade (solvent B). Linear gradient from 6% to 16% B in 10 min. Post run to 6% B: 3 min. The chromatograms were acquired at 198, 210, 225 and 254 nm wavelengths. The injection volume was 10 µL and the samples were dissolved in ultrapure water.

Semi-preparative reversed-phase high-performance liquid chromatography (Semi-preparative RP-HPLC)

Semi-preparative RP-HPLC was performed on a Waters 1525 binary pump HPLC with a Waters 2992 photodiode array detector. The analyses of the HPLC data were conducted on Waters Empower^{TM} 3 software. Reverse-phase HPLC chromatography was carried out using a RP 18, Waters X-Bridge C18, 5 µm, 10 x 150 mm and a Waters X Bridge Prep C18, 5 µm, 10 x 10 mm Guard Cartridge. The pure product collections were conducted using a Waters fraction collector III.

Purification of MacroP

MacroP purification was performed by semi-preparative RP-HPLC, using a gradient solvent system at a flow rate of 3 mL/min. The gradient mixture was composed of 0.1% aqueous TFA (solvent A) and acetonitrile gradient grade (solvent B).

Linear gradient from 6% to 16% B in 10 min. Post run to 6% B: 3 min. The chromatograms were acquired at 198, 210, 225 and 254 nm wavelengths.
The injections were performed using a 500 µL loop, using the partial loop-fill injection method.

Mass spectrometry

The characterization of MacroP was performed by mass spectrometry.
The mass spectrometer LTQ-Orbitrap Velos Pro was operated in positive ionization mode.
Single MS survey scans were performed in the Orbitrap, recording a mass window between 150 and 2000 m/z. The Full Scan resolution was set to 120000. Samples were diluted 1:100 with a water/acetonitrile (50:50 v/v) solution containing 1% AcOH and introduced into the mass spectrometer by means of direct infusion at a flow rate of 5 µL/min with a syringe pump.

Determination of MacroP chelating efficiency

This determination has been exploited as a titrimetric method to evaluate the chemical purity of MacroP. The spectrophotometric assay is based on the decrease of the 656 nm absorption of the complex between Pb^{++} and Arsenazo (AA), for the concurrent formation of the Pb-DOTA complex.
A stock solution of Pb-(II)-AA(III), containing 67.62 µmol/L of Pb(II) and 140 µmol/L of AA(III), was prepared in $AcONH_4$ buffer (0.15 M, pH=7.00). Such stock solution must be stored protected from light, at a temperature of 2-6°C and used at room temperature within one day from its preparation.
A stock solution of 0.26 mM DOTA in $AcONH_4$ buffer (0.15 M, pH=7.00) was also prepared.
For the calibration curve (Fig. 69), six standard solutions were used, containing increasing concentrations of DOTA from 0 to 0.024 mM. For their preparation 3.4 mL of Pb(II)-AA(III) stock solution, 200 µL of 1 M NaCl (in 0.15 M $AcONH_4$ buffer) and a variable volume of DOTA stock solution (0-500 µL), depending on the desired final concentration, were mixed. The final 4.2 mL volume of each standard solution was reached by adding a suitable volume of $AcONH_4$ buffer (0.15 M, pH=7.00).

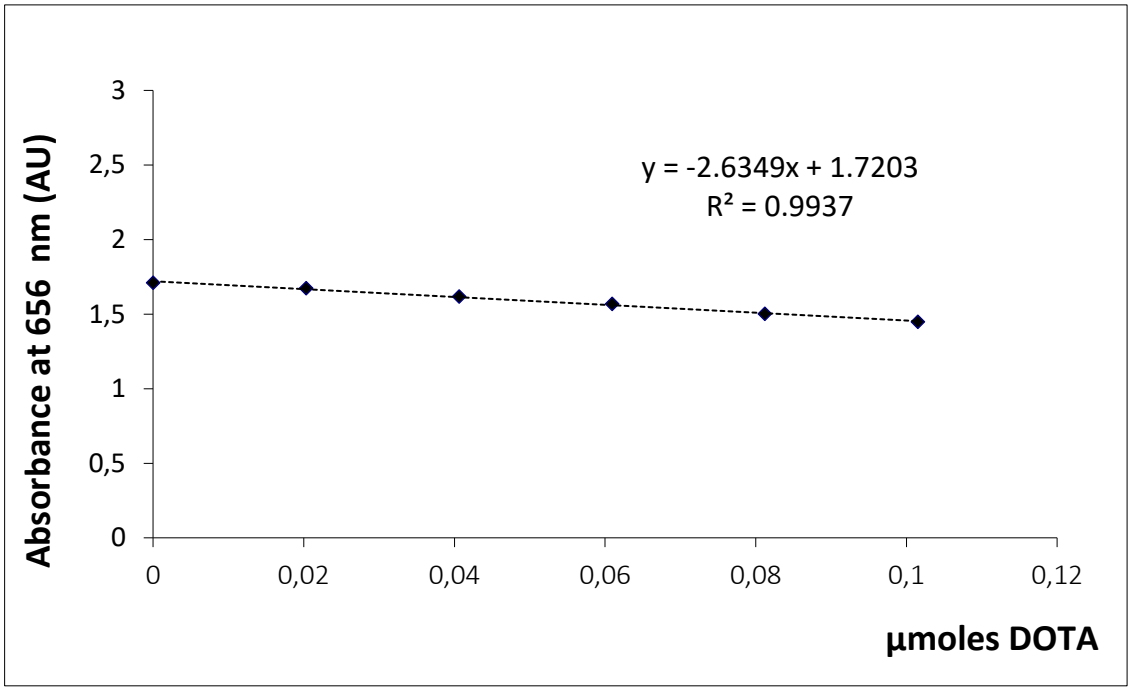

Fig. 69: Calibration curve for the spectrophotometric determination of MacroP chemical purity, by Pb-Arsenazo method.

The sample solution was prepared adding 40 µL of a 1.6 mM MacroP aqueous solution to a mixture containing 3.4 mL of Pb(II)-AA(III) stock solution, 200 µL of 1 M NaCl, 560 µL of $AcONH_4$ buffer (0.15 M, pH=7.00).

For each solution, absorbance at 656 nm was determined, 10 min after its preparation, at room temperature and protected from light.

The reading was corrected subtracting the absorbance of a mixture made of 4.0 mL of $AcONH_4$ buffer (0.15 M, pH=7.00) and 200 µL of 1 M NaCl.

RESULTS AND DISCUSSION

Synthesis of MacroP

The conjugation reaction between maleimido-monoamide DOTA (MMA-DOTA) and the VCAM-1 binding peptide was initially performed in phosphate buffer at pH 7, at 37°C for 2h, in accordance with the literature. To avoid the formation of byproducts in the reaction mixture, no reducing agent (e.g. TCEP or DTT) was added.

The reaction mixture was analysed by analytical RP-HPLC and by the comparison with standard solutions of MMA-DOTA and peptide in phosphate buffer at pH 7, the peaks of the chromatogram were identified (Fig. 70).

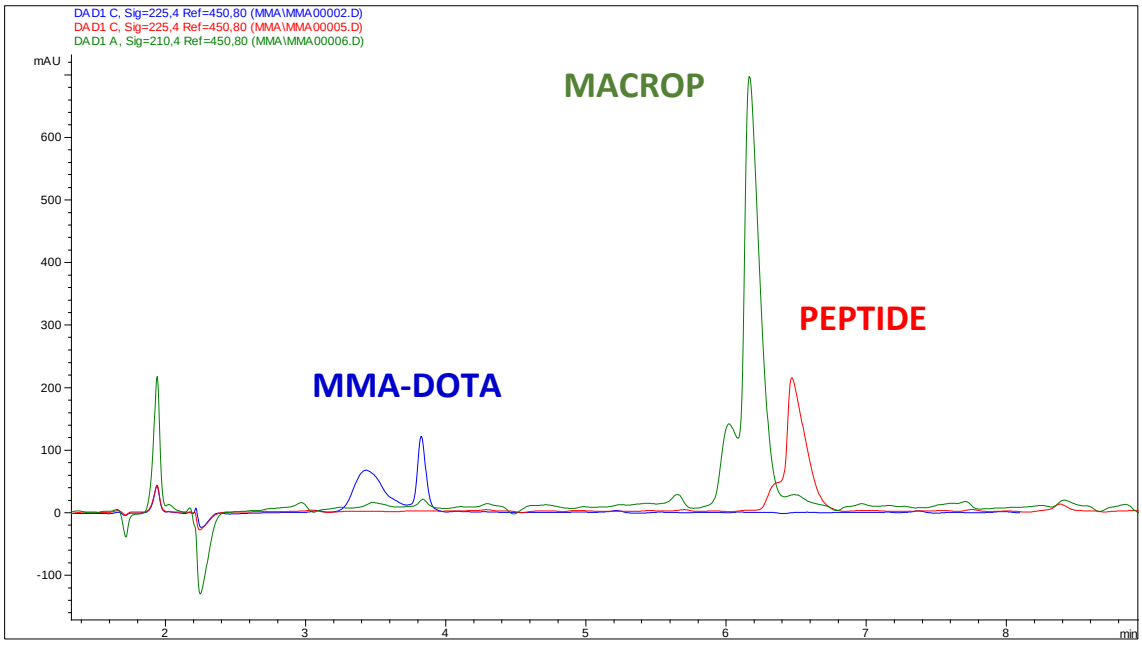

Fig. 70: RP-HPLC comparison between MMA-DOTA (blue) and peptide (red) standard solutions and the reaction mixture in phosphate buffer (green).

MMA-DOTA and the peptide were scarcely detectable in the reaction mixture and a new peak with t_R very similar to the peptide one appeared.

Since the MMA-DOTA solution in phosphate buffer showed two peaks, it was supposed that they could be related to the two ionic forms of the carboxylic groups, but, as a DOTA solution in phosphate buffer under the same analytical conditions showed only one peak, the 2 peaks were attributed to the maleimidic portion of the MMA-DOTA.

Successively, an aqueous solution of MMA-DOTA was analysed at the same concentration of the phosphate buffer solution and, as shown in Fig. 71, it presented only the second peak; therefore, the first peak resulted to be a MMA-DOTA derivative forming exclusively in phosphate buffer at pH 7.

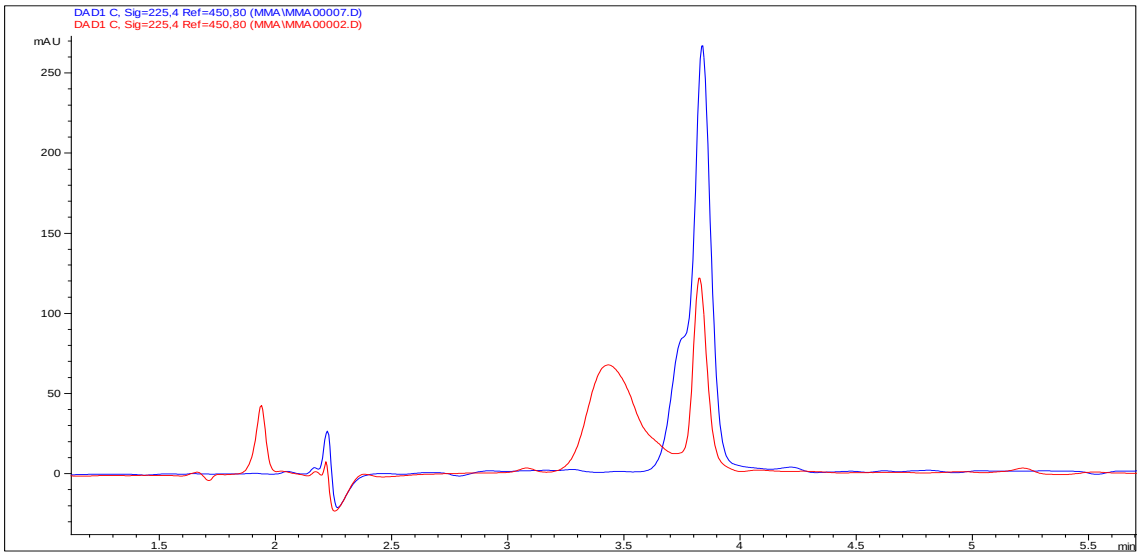

Fig. 71:RP-HPLC comparison between MMA-DOTA in phosphate buffer (red) and in water (blue).

Even if the reagents were hardly detectable in the final mixture at the experimental condition used, a prolongation of the reaction time was evaluated and the reaction mixture after 19h was analysed by RP-HPLC and compared to the previous reaction (Fig. 72).

Under the new conditions, MMA-DOTA disappeared, but the supposed peak of MacroP decreased and some new unknown peaks formed.

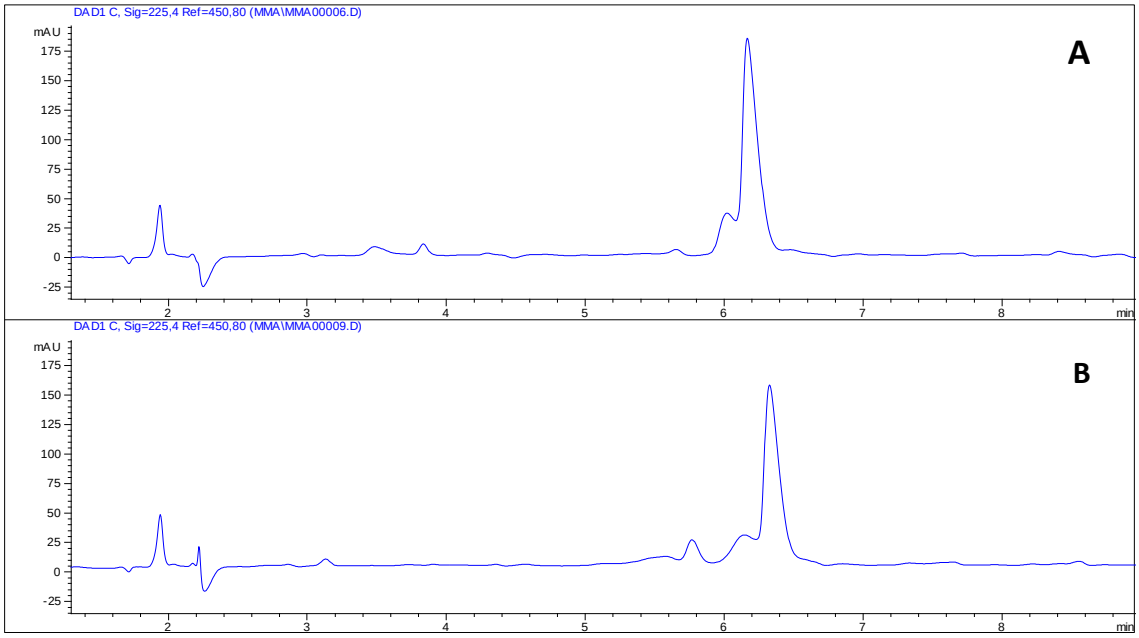

Fig. 72: RP-HPLC comparison between the reaction mixtures at 2h(A) and 19h(B).

Hence, to reduce the formation of impurities and increase the amount of the supposed product, the reaction was also repeated using ultrapure water as reaction medium.

Fig. 73 shows the RP-HPLC comparison between the reaction mixtures in phosphate buffer and in water, after stirring at 37°C for 19h.

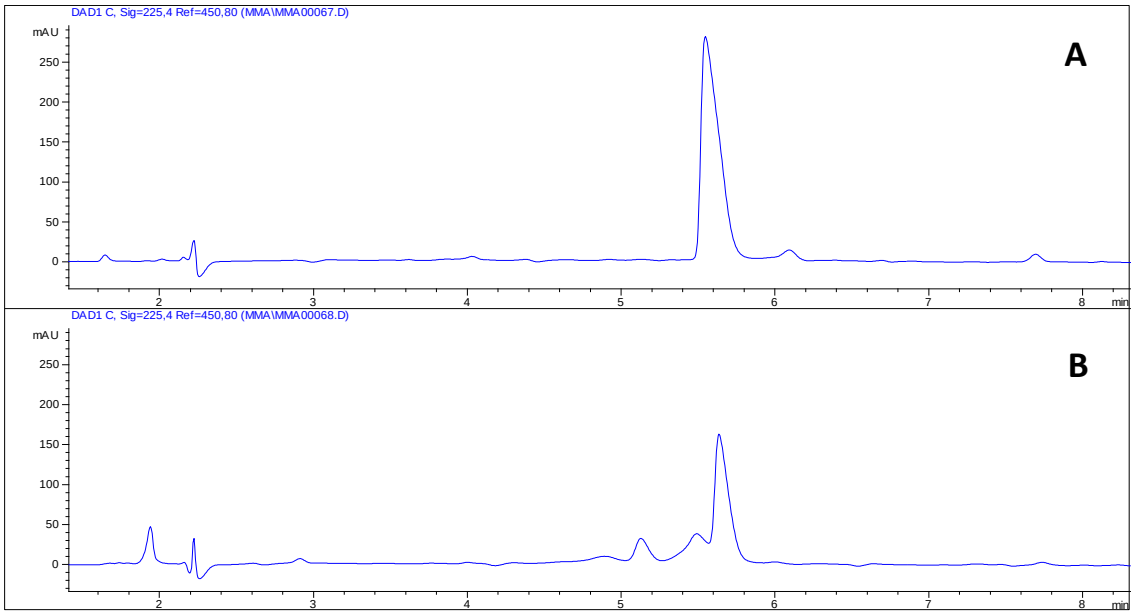

Fig. 73: RP-HPLC comparison between reaction mixtures in water(A) and in phosphate buffer(B).

Carrying out the reaction in water, a remarkable increase of the peak of interest was obtained, furthermore, within the detection limits of the analytical method applied, it was not possible to detect any residual MMA-DOTA.

Since a small amount of unreacted peptide and of its impurity were present in the reaction mixture carried out in water, an excess of MMA-DOTA was added.

Fig. 74 shows the RP-HPLC comparison between the reaction mixture before and after the addition of the reagent.

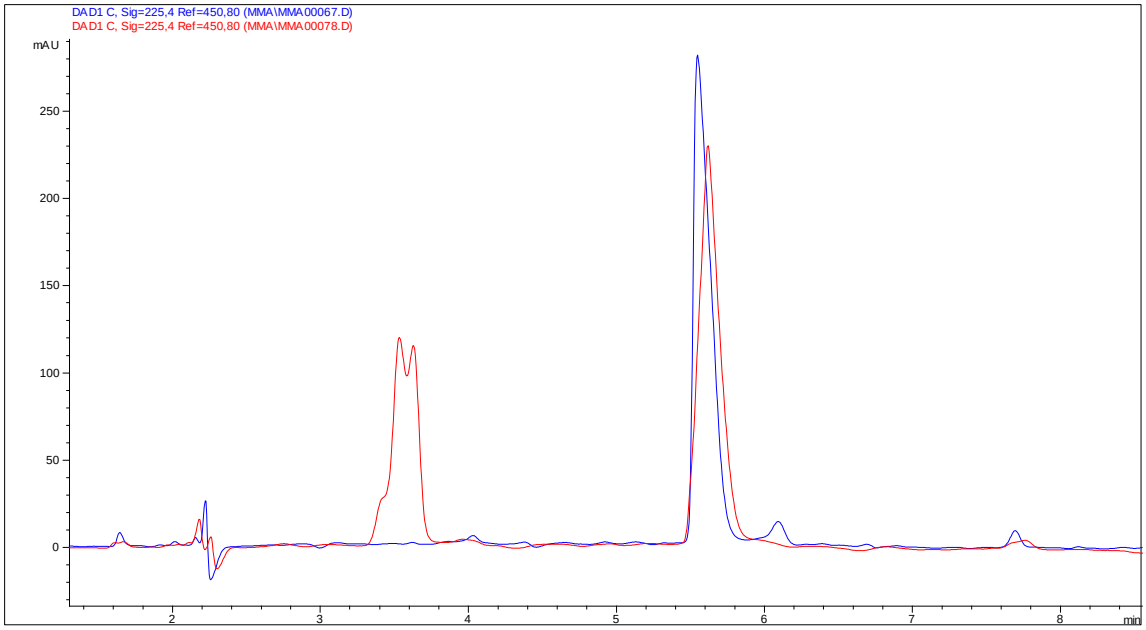

Fig. 74: RP-HPLC comparison between reaction mixtures in water before (blue) and after the addition of MMA-DOTA (red).

The chromatogram after adding MMA-DOTA showed that the peptide had disappeared and a slight increase of the area of the peak of interest had occurred.

Therefore, further modifications to the reaction conditions were applied:

1. The amount of MMA-DOTA was increased from a molar ratio of 1.2 to 2 with respect to the amount of peptide;
2. The reaction time was extended to 48h.

The obtained reaction mixture, whose chromatogram is shown in Fig. 75, showed increased product formation and the presence of unreacted MMA-DOTA.

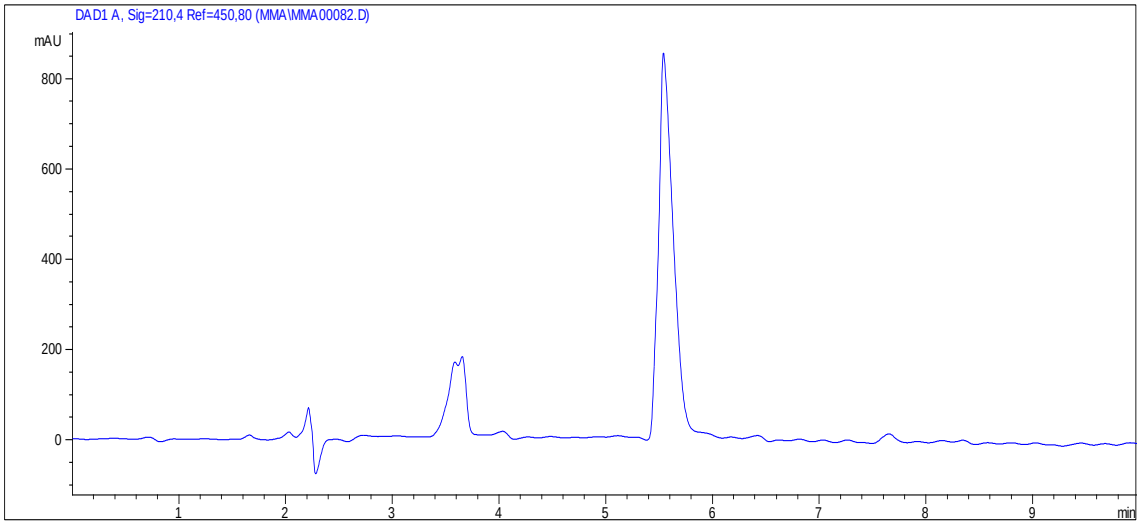

Fig. 75: Chromatogram of the reaction mixture in water after 48h.

MacroP was purified by semi-preparative RP-HPLC and, since it was impossible to weigh the final amount of product, for the small scale of the reaction, its concentration was estimated. In fact by the total amount of MMA-DOTA used as reagent and by the excess in the reaction mixture, the reacted mmol of the DOTA derivative, corresponding to the mmol of conjugate formed, were calculated.

Characterization of MacroP

The product was analysed by analytical RP-HPLC (Fig. 76) and mass spectrometry (Fig. 77), resulting highly pure.

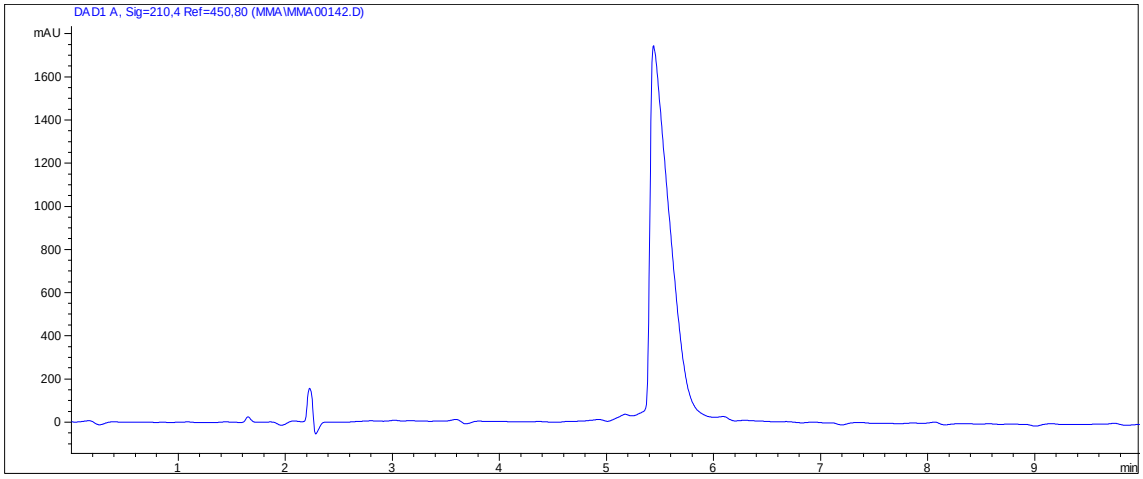

Fig. 76: Purified MacroP.

The mass spectrometry analysis of MacroP was performed by a LTQ Orbitrap Velos Pro, in order to confirm the identity of the substance and to identify the thioether bond between the thiol group of the VCAM-1 binding peptide and the maleimide of MMA-DOTA.

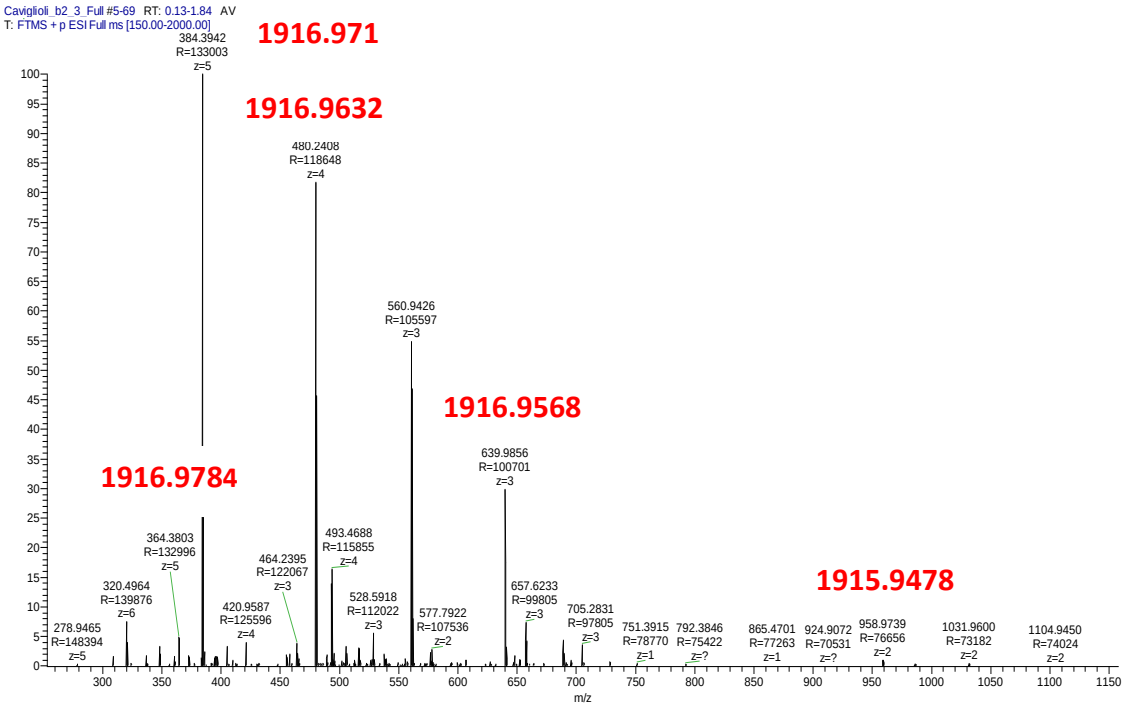

Fig. 77: Mass spectrum of MacroP.

The calculated monoisotopic mass is 1915.9, but the presence of peaks with a mass of 1916.9 is justified by the abundance of the different isotopes of the elements in the molecule.

In fact, mass spectrometry cannot detect single molecules but is influenced by the millions of copies of a molecule that includes different isotope species.

In mass spectrometry, the monoisotopic mass is most often used: it is the sum of the masses of the atoms in a molecule using the principle (most abundant) isotope mass of each atom instead of the isotope averaged atomic mass (atomic weight).

The mass spectral peak representing the monoisotopic mass is not always the most abundant isotopic peak in a spectrum, although it stems from the most abundant isotope of each atom type. In fact, as the number of atoms in a molecule increases, the probability for the entire molecule to contain at least one heavy isotope increases.

Fig. 78 shows the isotopic distribution of the principal m/z peaks of the MacroP mass spectrum. It is possible to note that the molecular ion with mass 1916.9 is more abundant than the one with mass 1915.9.

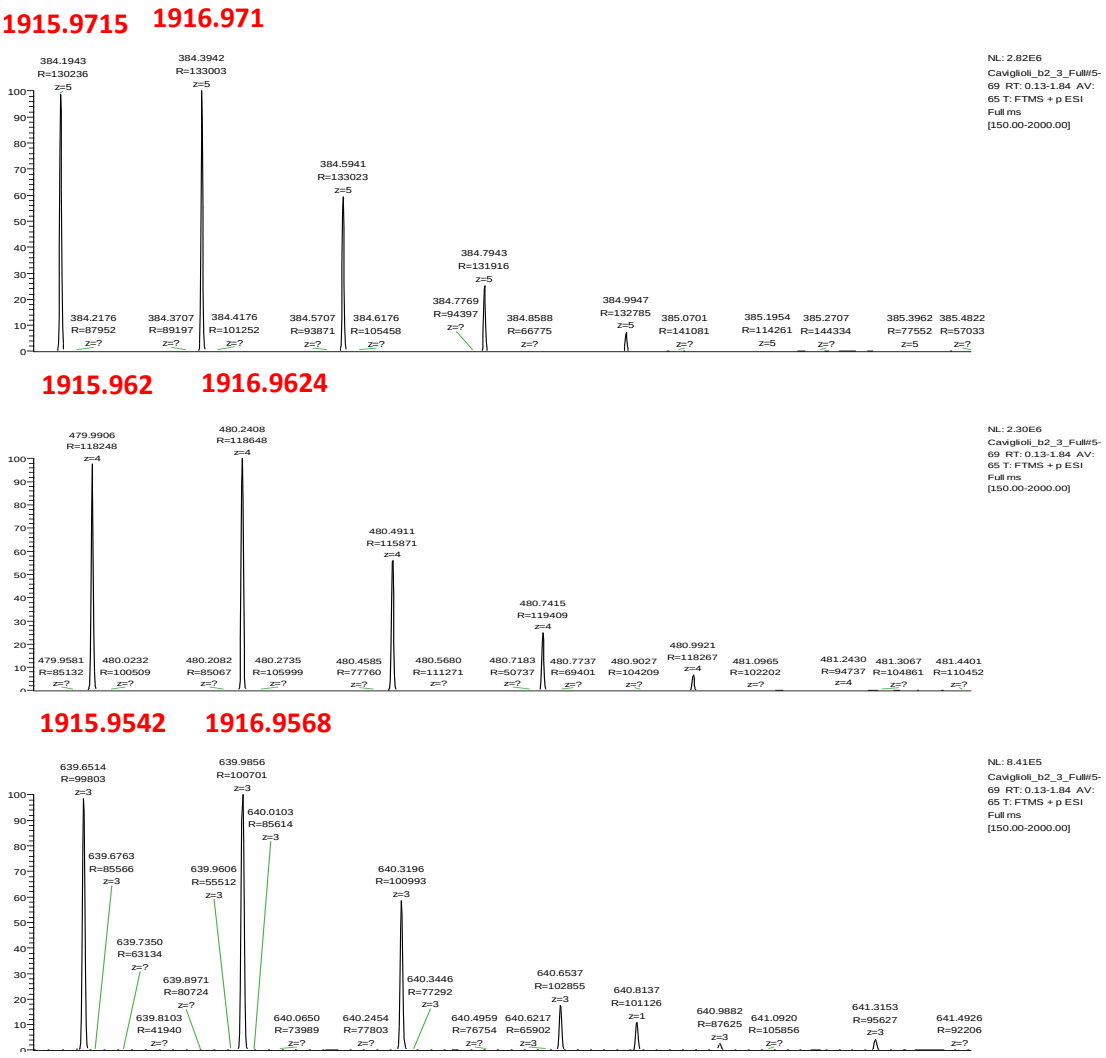

Fig. 78: Isotopic distribution of MacroP.

By the MS^2 fragmentation spectrum obtained from the peak with m/z of 384.39, it was possible to identify the fragments related to the cleavage of the aminoacids occurred at the peptide amide bond and the relative y ions (Fig. 79).

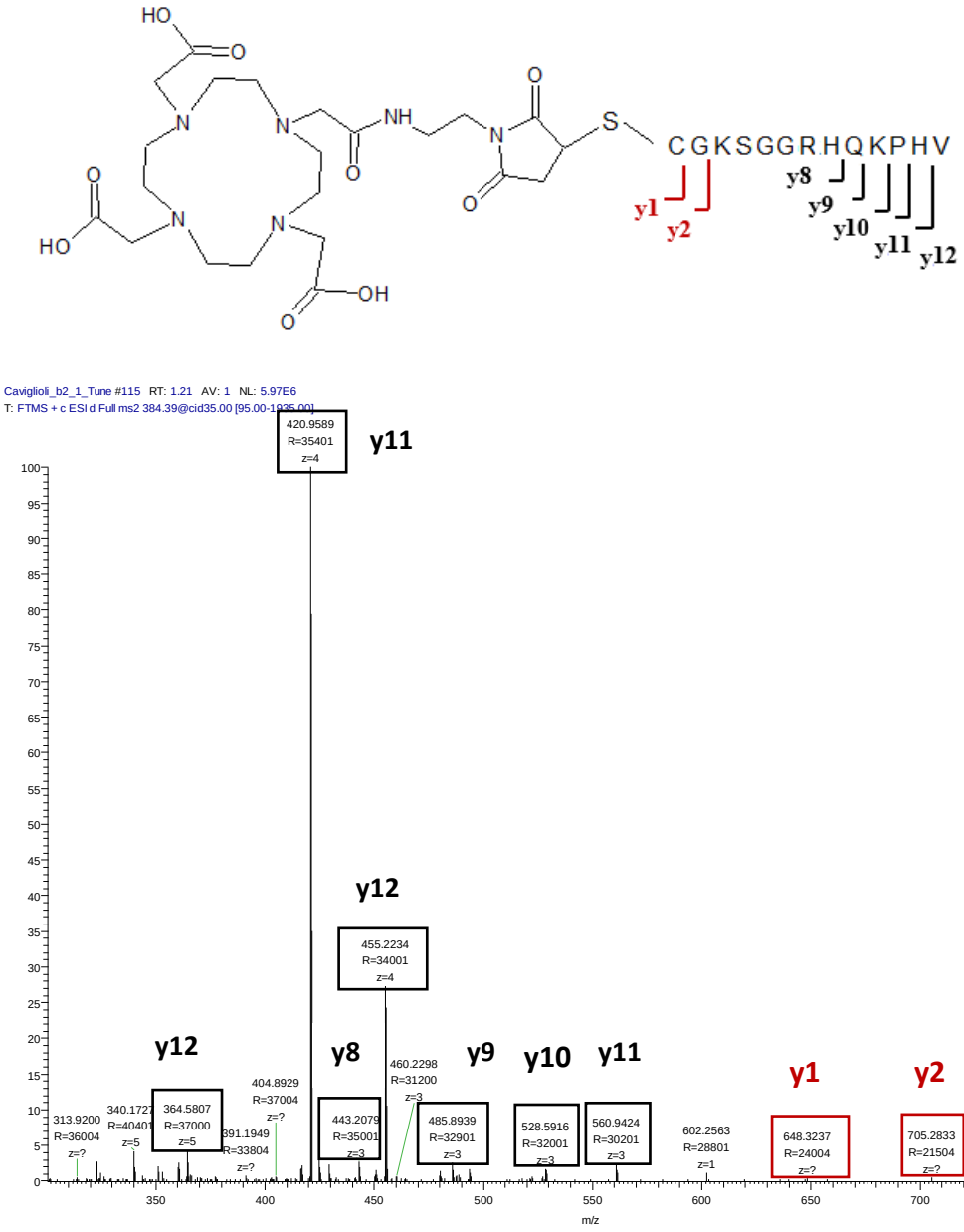

Fig. 79: MS^2 fragmentation spectrum of the peak with m/z 384.39.

The presence of ions y1 and y2 is related to the fragments of the DOTA derivative conjugated respectively with the cysteine and the cysteine-glycine, indicative of the formation of the thioether bound.

These fragments are also visible in the MS^3 fragmentation spectrum of the peak with m/z 420.96 (Fig. 80).

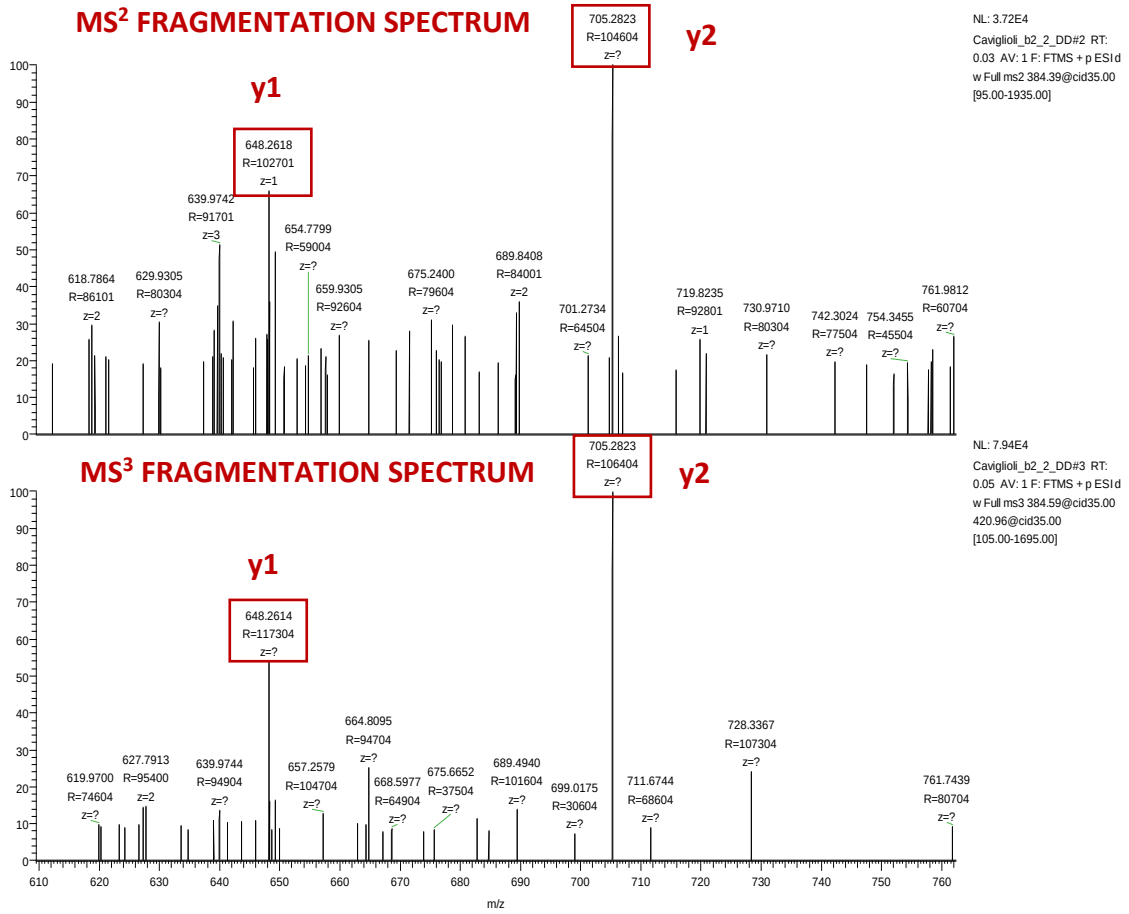

Fig. 80: MS^2 and MS^3 fragmentation spectra of the peaks with m/z 384.39 and 420.96, respectively.

Since during the synthesis and purification a metallic contamination could occur and cause the incapacity of MacroP to chelate the radionuclide, the complexing capacity of the product was evaluated, before radiolabeling.

On this purpose, a method developed by Caviglioli et al. [56] was used based on the decrease of the 656 nm absorbance of a complex between lead and arsenazo, for the concurrent formation of the complex between the metal and the DOTA derivative.

By a calibration curve, measuring the UV absorption of the product, the amount of chelating macrocycle was calculated.

The chemical purity estimated by this method differed by 25% from the concentration of the product in the reaction mixture calculated as previously described. This might be due to accuracy issue in the RC-HPLC method or to metals contamination in the arsenazo test.

CONCLUSION

A new radiopharmaceutical, consisting of a DOTA derivative conjugated with the VCAM-1 binding peptide, has been synthesized and purified, in order to acquire diagnostic images of early stage atherosclerotic plaques.

4. CHAPTER 3

Radiolabeling and in vitro test

INTRODUCTION

Radionuclides

A radiopharmaceutical is any medicinal product which, when ready for use, contains one or more radionuclides (radioactive isotopes) included for a medicinal purpose (directive 2001/83/EC). The radionuclide is integral to the medicinal application of the preparation, making it appropriate for one or more diagnostic or therapeutic applications [57].

A radionuclide is a nuclide containing an unstable arrangement of protons and neutrons ("parent radionuclide") that transforms spontaneously to either a stable or another unstable combination of protons and neutrons ("daughter nuclide"), with a constant statistical probability, by emission of radiation ("radioactive transmutation" or "radioactive disintegration" or "radioactive decay").

As the nucleus contains protons and neutrons, such transformations involve reactions of sub-atomic particles. The stability of the nucleus predominantly depends on the total number of nucleons (protons and neutrons), as well as on the ratio of the protons (p) to the neutrons (n). Generally, a proton-rich (or neutron-deficient) nuclide would transform to reduce the proton content, while a neutron-rich nuclide would transform vice versa.

Such transformations may involve emission of charged particles, capture of electron from the extra-nuclear orbits by the nucleus or isomeric transition.

The charged particles emitted from the nucleus may be alpha (α) particles or beta (β) particles. Beta particles may be either negatively charged β^- (negatrons and generally equivalent to electrons) or positively charged β^+ (positrons).

The emission of charged particles from the nucleus may be accompanied by the emission of gamma (γ) rays, which are energetic photons of electromagnetic radiation and do not have any charge or mass.

Gamma rays are also emitted in a process called isomeric transition (IT), where an excited state of a radionuclide decays to the de-excited state, with no changes in atomic, mass or neutron number.

The emissions of gamma rays may be partly replaced by the ejection of electrons, known as internal conversion (IC) electrons, due to the interaction of the gamma ray with the extranuclear orbital electrons.

This phenomenon, like the process of electron capture, causes a secondary emission of X-rays (due to the vacancies created in the electronic orbits, which are then filled by reorganization of the electrons from the outer orbits in the atom).

This secondary emission of X-rays may itself be partly replaced by the ejection of outer electrons known as Auger electrons, due to the interaction of the X-rays with the outer electrons.

Radioactive decay

Radioactivity decays at an exponential rate with a particular decay constant and is a characteristic of each radionuclide.

The exponential decay (decay curve) is described by the equation: $A_t = A_o\, e^{-\lambda t}$

A_t = the radioactivity at time t,

A_o = the radioactivity at time t = 0,

λ = the decay constant characteristic of each radionuclide,

e = the base of Napierian logarithms.

The time in which a given quantity of a radionuclide decays to half its initial value is termed the half-life ($t_{1/2}$). The half-life ($t_{1/2}$) is related to the decay constant (λ) by the equation: $t_{1/2} = 0.693/\lambda$

The radionuclide is generally identified by its half-life or by the nature and energy of its radiation or radiations emitted or by both, as prescribed in the Pharmacopoeia monograph.

The penetrating power of each radiation varies considerably according to its nature and its energy. Alpha particles, which are the heaviest among the radiations, have the minimum penetration, followed by the beta particles and gamma rays.

The modes of radioactive decay are:

-Alpha decay (α): radioactive nuclei having too many nucleons (n and p) often undergo alpha decay, in order to achieve nuclear stability. An alpha particle has a mass of 4 units and a charge of +2 units.

-Negatron decay (β^-): radioactive nuclei having neutrons in excess to what is needed for a stable configuration mostly undergo β^- decay, in order to achieve nuclear stability.

Negatrons have the same mass and electrical charge of orbital electrons, but they originate from the nucleus at the instant of decay, when a neutron turns into a proton.

Such transformation results in increase in atomic number by 1, while the mass does not change significantly.

The β^- decay phenomenon could be expressed with the following nuclear reaction:

$$n \rightarrow p + \beta^- + \nu^*$$

ν^* represents an "anti-neutrino", a sub-atomic entity that does not have any mass or charge, but can possess energy. The ν^* is important for accounting for the conservation of momentum, spin and energy.

-Positron decay (β^+): radioactive nuclei having less neutrons than what is needed for a stable configuration undergo positron β^+ decay in order to achieve stability, if adequate energy is available from the nucleus for the transformation of a proton to a neutron. Such a transformation results in decrease in atomic number by 1, while the mass does not change significantly.

The β^+ decay phenomenon could be expressed with the following nuclear reaction:

$$p \rightarrow n + \beta^+ + \nu$$

As in the case of β^- decay, in order to conserve momentum, spin and energy, a sub- atomic entity that does not have any mass or charge but carrying some energy is emitted, known as "neutrino" and represented by ν.

-Electron capture (EC): radioactive nuclei having less neutrons than what is needed for a stable configuration and not having adequate energy available to undergo positron β^+ decay follow another route named "electron capture", in order to achieve stability. In this decay mode an orbital electron is captured and taken into the nucleus, thus facilitating the conversion of a proton to a neutron, resulting in a nuclide with decrease in atomic number by 1. An electron capture reaction can be written as:

$$^+p + e^- \rightarrow n + \nu$$

-Gamma decay (γ): gamma rays are electromagnetic rays coming out of a nucleus as a result of the difference in nuclear energy levels of the excited and the ground states of the daughter nuclide when a nuclear transmutation takes place. Most radioactive decays are accompanied by γ rays, although this is not essential.

Since γ rays carry the energy arising out of the difference in nuclear energy levels, these are often highly energetic, with energy higher than those of X-rays.

-Isomeric transition (IT): when an excited nucleus de-excites by emission of a delayed gamma ray, the daughter nucleus is a nuclear isomer of the parent and the process is called

isomeric transition. As mentioned earlier, gamma rays are emitted owing to the energy difference in the nuclear states of the excited and the ground states of the daughter nuclide after a transmutation or decay. Such γ ray emissions are very quick and happen within nanoseconds.

However, if the de-excitation of the daughter nuclide from the excited state to ground state does not occur easily (due to rules that govern such transitions), then such transitions become slow and the excited state of the nuclide is referred to as "metastable" state, indicated by the symbol "m" after the atomic number (e.g. ^{99m}Tc). Nuclear isomers have the same number of protons and the same number of neutrons, although they are arranged in a more stable configuration in the daughter nucleus.

Radionuclide production

The practical ways of producing radionuclides for use in, or as radiopharmaceutical preparations, are by neutron bombardment of target materials (generally in nuclear reactors); charged particles bombardment of target materials (in accelerators such as cyclotrons); nuclear fission of heavy nuclides of target materials (generally after neutron or particle bombardment); and from a radionuclide generator.

Regarding neutron or charged particle bombardment, the nuclear reaction and the probability of its occurrence in unit time are dependent on the nature and physical properties of the target material and the nature, energy and quantity of the incident particles. The nuclear transformation occurring through particle bombardment may be written in the form:

target nucleus (bombarding particle, emitted particle or radiation) produced nucleus.

Examples: $^{58}Fe(n,\gamma)^{59}Fe$; $^{18}O(p,n)^{18}F$

Nuclear fission is based on the fact that a small number of nuclides with a high atomic number are fissionable and the most frequently used reaction is the fission of uranium-235 by neutrons in a nuclear reactor. Iodine-131, molybdenum-99 and xenon-133 may be produced by nuclear fission of uranium-235.

Radionuclide generator systems use a relatively long-lived parent radionuclide that decays to a daughter radionuclide, usually with a shorter half-life.

The parent radionuclide and the daughter radionuclide exist in transient or secular equilibria depending on the $t_{1/2}$ ratio of parent and daughter radionuclides.

The daughter radionuclide is separated from the parent radionuclide using a chemical or physical process. The duration for which the generator can be used will depend on the $t_{1/2}$ of the parent radionuclide.

The target material is contained in a holder in gaseous, liquid or solid state, in order to be irradiated by a beam of particles. It is necessary to ascertain that no interaction can occur between the container and its contents under the irradiation conditions (temperature, pressure, time).

For neutron bombardment, the target material is commonly contained in quartz ampoules or high purity aluminium or titanium containers. For charged particle bombardment, the holder for target material is usually built of aluminium or another appropriate metal, with a low cross-section for the irradiating particles and also having a good thermal conductivity to remove the generated heat.

Positron emission tomography (PET)

PET is a non-invasive imaging technique that visualizes the distribution and accumulation of positron-emitting tracers in the whole body with high sensitivity providing functional and molecular information on tissues. With its high sensitivity for radiotracers even in picomolar amounts, PET allows for excellent depiction of specific metabolic activity, molecules and receptors *in vivo* [58].

PET utilizes positron-emitting radioligands. After the emission from the parent nucleus, the energetic positron traverses a few millimeters through the tissue until it becomes thermalized by electrostatic interactions with the electrons and the atomic nuclei of the medium and combines with a free electron to form a positronium. The positronium decays by annihilation, generating a pair of gamma rays which travel in nearly opposite directions with an energy of 511 keV each. The opposed photons from positron decay can be detected by using pairs of collinearly aligned detectors in coincidence. This “electronic collimation” is the reason why PET is much more sensitive (factor >100) than SPECT, the other conventional nuclear medical technique, using radionuclides directly emitting gamma rays, detected by cameras and lead collimators.

The detector pairs of a PET system are installed in a ring-like pattern (Fig. 81), which allows measurement of radioactivity along lines through the organ of interest at a large

number of angles and radial distances. Subsequently, this angular information is used in the reconstruction of tomographic images of regional radioactivity distribution [59].

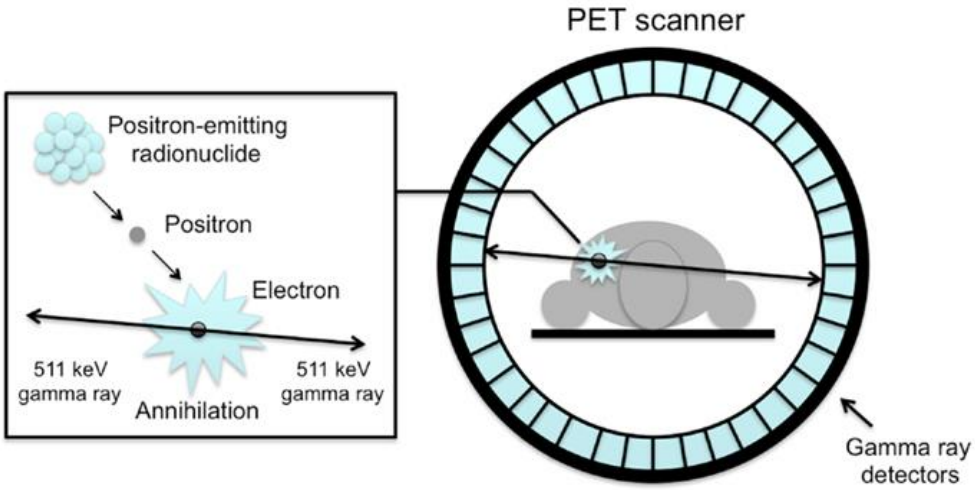

Fig. 81: Positron emission and positron-electron annihilation.

The most common positron emitting isotopes are reported in Table 4.

Table 4: Principal PET radiotracers.

Isotope	Half-life
C-11	20.4 min
N-13	9.98 min
O-15	2.03 min
F-18	109.8 min
K-38	7.64 min
Cu-62	9.74 min
Cu-64	12.7 h
Ga-68	68.1 min
Rb-82	1.25 min
I-124	4.18 d
Zr-89	78.4 h

The primary advantage of PET over other imaging modalities is the high sensitivity and pharmacological specificity that makes it highly suitable for imaging of chemicals in very low concentrations (nanomolar to subpicomolar).

Disadvantages of PET are radiation exposure, limited spatial and temporal resolution, and cost. The costs of PET are elevated because it uses very short-lived radionuclides that necessitate the maintenance of an onsite cyclotron in proximal vicinity and trained staff for its maintenance. Moreover, for PET, the "synthesis time" must be very rapid to accommodate the quickly decaying radionuclides.

PET images do not contain detailed anatomical information, for this reason hybrid imaging, associating PET with computed tomography (CT), has become a standard component of medical imaging.

The use of this hybrid technique permits to combine the metabolic and molecular information of PET with the anatomical detail of CT.

Gallium-68

Gallium is a metal of the group 13 in the periodic table and has 24 isotopes with known half-lives and mass numbers 61 to 84. Among these, two are stable: ^{69}Ga and ^{71}Ga with natural abundances of 60.1% and 39.9% respectively. Among Ga radioisotopes, three have raised interest in the nuclear medicine field: ^{66}Ga, ^{67}Ga and ^{68}Ga (Table 5) [60].

Table 5: Physical properties of important gallium radioisotopes.

Radionuclide	Half-life	Radiation	Production
^{66}Ga	9.5 h	β^+ (56%)	Cyclotron
^{68}Ga	68.1 min	β^+ (89%)	Generator
^{67}Ga	78.26 h	γ	Cyclotron

Gallium-68 is a positron emitter with a half-life of 68.1 min and dominantly decays via 1.92 MeV positron emission (89%) and electron capture (11%).

Germanium-68 decays by pure electron capture (EC) to the ground state of ^{68}Ga with a half-life of 270.95 days. Gallium-68 in turn decays by a combination of EC and positron emission primarily to the ground state of ^{68}Zn [60].

The use of a ^{68}Ge/^{68}Ga generator system ensures direct access to a short-lived PET radionuclide within the PET facility or nuclear medicine department for a period of up to one year without the on-site availability of a cyclotron. Furthermore, the relatively short half-life and hydrophilic nature are favourable for the rapid renal clearance and reduce effective dose for the patient [61].

The interesting physical properties and availability of gallium-68 make it an interesting nuclide for developing new PET tracers offering new opportunities for researchers to design various ^{68}Ga-radiopharmaceuticals [60].

Gallium is usually found in oxidation state of +3 in aqueous solutions and, due to high positive charge and small ionic radius, is quite acidic (with a pKa of 2.6) and found in hydrated form. Thus, Ga cation has low water solubility in normal pH media without the presence of suitable donors. Due to its strong affinity for the hydroxide ion, at very high pH it also has a propensity to demetallate from its complexes and form the gallate anion $Ga(OH)_4^-$.

Likewise other classic hard acidic cations, Ga(III) is strongly bound by ligands including multiple anionic oxygen donor sites, although it has also shown good affinity for thiolates and amines usually forming Ga(III)- chelates up to its maximum coordinate number of 6 in a pseudo-octahedral geometry.

Most commonly used Ga chelates in radiopharmaceutical development consist of amine and phenol groups. Presently the most prevalent bifunctional ligands used in developing ^{68}Ga-labeled compounds are from macrocyclic compounds with nitrogen heteroatoms including DOTA and NOTA chelates [60].

In this chapter, the radiolabeling of BisDOTA and MacroP, performed in collaboration with the division of nuclear medicine of the IEO in Milan and the radiopharmacy laboratories of San Martino hospital in Genoa and Sant'Andrea in La Spezia, will be reported.

Furthermore, the *in vitro* test performed on NAMP-avidin-BisDOTA and MacroP will be discussed.

MATERIALS AND METHODS

Materials

Ammonium acetate ($AcONH_4$) (Merck); antibody CD106 (VCAM-1) conjugated with the fluorescent dye phycoerythrin (PE) (Milteniy Biotec); attachment factor-coated plates (Thermo Fisher Scientific); avidin (Sigma Aldrich); culture medium EndoGRO-LS Complete Culture Media Kit (Millipore); high pure RNA isolation kit (Roche); human recombinant VCAM-1 (Sigma Aldrich); human TNF-α (Milteniy Biotec); iScript cDNA synthesis kit (Bio-Rad); ITLC SG (Varian); maleimido-monoamide-DOTA (MMA-DOTA) (Macrocyclics); Microcon®-30 centrifugal filters (Merck); MKC18F silica gel TLC plates (Whatman); ITLC-SG paper strips; phosphate buffer pH 2.5 e pH 7 for HPCE; sodium acetate trihydrate (Merck); saline for human use; trypsin (Gibco); water for injections (B.Braun); 30% HCl ultra-pure (Merck). All chemicals were used as received, without further purification. The water used was purified with a Milli-Q system from Millipore.

Instruments

ALC PK 120 centrifuge; BD FACSCanto II (BD Biosciences); CFX96 touch real-time PCR (Bio-Rad); LigandTracer® White (Ridgeview Instruments AB, Uppsala, Sweden); Packard BioScience Cyclone CT; Hewlett Packard Series II 1090 liquid chromatograph; Merck Hitachi LaChrom L-7100/L7100 HPLC; Mettler Toledo XS3DU electronic microbalance; Eckert & Ziegler Eurotope Modular Lab-Pharm Tracer®; Eckert & Ziegler Eurotope Modular Lab Standard®; SsoFastTM EvaGreen mix (Bio-Rad); Torrey-Pines Scientific EchoTherm™ SC25XT orbital mixing dry bath; LTQ Orbitrap Velos Pro; Perkin Elmer Radiomatic 150TR flow scintillation analyzer; Scaltec SBC 21 electronic analytical balance; Thermo Scientific UltiMate 3000 UHPLC systems.

Methods

NAMP-avidin binding

A stock solution of avidin was prepared by dissolving 0.5 mg of protein in 200 µL of ultrapure water. 100 µL of this solution (3.8×10^{-6} mmol) were mixed with 100 µL of approx. 0.17 mM NAMP aqueous solution (17×10^{-6} mmol). The reaction mixture was heated at 37°C, under 400 rpm orbital shaking for 2h.

NAMP-avidin binding analysis by ultrafiltration

The reaction mixture containing NAMP and avidin was placed in an ultrafiltration system with a regenerated cellulose membrane with 30 kDa NMWL-nominal molecular weight limit, and washed with 250 µL of ultrapure water at 14000 g for 20 min at 15°C. The retentate was recovered by inverted spinning at 1000 g for 3 min.

NAMP-avidin-BisDOTA binding

To 36 µL of the retentate derived from NAMP-avidin ultrafiltration (1.13×10^{-6} mmol) 15 µL of a 1 mg/mL BisDOTA solution (11.3×10^{-6} mmol) were added. The reaction mixture was heated at 25°C, under orbital shaking at 400 rpm for 1h.

Another similar test was performed, in which NAMP, avidin and BisDOTA were mixed in a molar ratio of 2:1:2 respectively and incubated at 25°C under orbital shaking at 400 rpm for 1h.

NAMP-avidin-BisDOTA analysis by ultrafiltration

The reaction mixture containing NAMP, avidin and BisDOTA were transferred in an ultrafiltration system with a a regenerated cellulose membrane having a 30 kDa cut-off, and washed with 250 µL of ultrapure water at 14000 g for 20 min, at 15°C.

The retentate was recovered by inverted spinning at 1000 g for 3 min.

Capillary Electrophoresis (CE) analysis

CE analyses were performed using an Agilent Technologies 7100 Capillary Electrophoresis. The separations were carried out in a bare fused-silica capillary 50 µm (i.d.) x 64.5 cm (L) x 50 cm (l) (G1600-61239), thermostated at 30°C.

Before use, the capillary was activated with 1 M NaOH aqueous solution, 0.1 M NaOH aqueous solution and washed with ultrapure water; the conditioning and the run were performed with 50 mM sodium phosphate buffer pH 2.5. Before sample injection, a preconditioning with this buffer was performed for 120 s.

Samples were injected hydrodynamically applying a 100 mbar pressure for 2 s, followed by injection of buffer by applying a 100 mbar pressure for 1 s. The run was carried out with a gradient voltage from 0 to 30 kV in 0.2 min (positive polarity). Electropherograms were acquired at 198, 205, 215, 254 and 300 nm wavelengths.

Radiolabeling of BisDOTA with Gallium-68

Two different methods were used for BisDOTA radiolabeling.

BisDOTA1 method: the radiolabeling was performed with the Eckert & Ziegler Eurotope Modular Lab Standard® automated synthesis system.

^{68}Ga was eluted from ^{68}Ge/^{68}Ga generator with 6 mL of 0.1 M HCl solution and concentrated on a Strata-X-C ion exchange cartridge (SCX). By rinsing the cation exchange column with 800 µL of 0.02 M HCl in acetone 98%, $^{68}GaCl_3$ was eluted into the reaction vial containing 2 mL of 0.2 M sodium acetate buffer (pH 4) and 7.6 nmol of BisDOTA. The reaction was carried out at 95°C for 400 seconds. Without purification, the radiolabeled product was analyzed by ITLC.

BisDOTA2 method: the radiolabeling and purification of BisDOTA were performed with the Eckert & Ziegler Eurotope Modular Lab Pharm-Tracer® automated synthesis system. The ^{68}Ge/^{68}Ga generator was eluted with 6 mL of 0.1 M HCl solution and $^{68}GaCl_3$ was trapped on the SCX. The radioactive was released from the cartridge to the sample solution with 5.5 M HCl in 5 M NaCl solution.

Solution A was prepared by dissolving 0.29 g of sodium acetate in 2 mL of B.Braun water and adding 128 µL of 30% HCl solution. The sample solution was prepared by mixing 400 µL of solution A with 2 mL of B.Braun water and 9.2 µL of a 1 mg/mL BisDOTA solution (7 nmol). The radiolabeling was performed at 95°C for 5 minutes and at the end saline at room temperature, was added for cooling. The purification was performed with a C18 ion exchange cartridge, preconditioned with ethanol/water 1:1 (v/v) and washed with water. The product was eluted from the cartridge with ethanol/water 1:1 (v/v) and diluted in saline.

Determination of BisDOTA radochemical purity (RCP)

The radiochemical purity of BisDOTA was determined by RP-HPLC.

The analysis was performed on a UltiMate 3000 UHPLC systems with a Dionex UltiMate 3000 variable wavelength detectors and GABI Star (Raytest).

Reverse-phase HPLC chromatography was carried out using a Pursuit C18, 3 µm 3.0 x 150 mm, 200 Å column. For BisDOTA analysis, a gradient method at a flow rate of 0.6 mL/min was applied. The gradient mixture was composed of 0.1% aqueous TFA (solvent A) and 0.1% TFA in acetonitrile gradient grade (solvent B). Linear gradient from 5% to 30% B in 20 min. Post run to 5% B: 3 min. The injection volume was 20 µL. The chromatograms were acquired at 220 nm wavelength.

NAMP-avidin-radiolabeled BisDOTA binding

12 µL of 0.031 mM NAMP-avidin solution (about 0.37 nmol) were added to 500 µL of radiolabeled BisDOTA solution (36 MBq). The reaction was performed at room temperature for 20 minutes.

Analysis of NAMP-avidin-radiolabeled BisDOTA complex by ITLC

Instant thin-layer chromatography was carried out on Whatman MKC18F silica gel plate (60 Å, size 2.5 x 7.5 cm, layer thickness 200 µm) without activation.

The sample application volumes were 5 µL and 0.9% NaCl:acetonitrile 1:1 (v/v) was used as mobile phase for the development by ascending chromatography. The radiochromatographic profile was determined by an autoradiographic system that uses a high performance storage phosphor screen.

MacroP-VCAM-1 binding

A stock solution of VCAM-1 was prepared by dissolving 50 µg of protein in 100 µL of ultrapure water. 24 µL of this solution diluted 1:1 with water (0.08 nmol) were mixed with 26 µL of approx. 3.2 µM MacroP aqueous solution (0.08 nmol). The reaction mixture was incubated at 37°C, under 400 rpm orbital shaking for 2h.

Radiolabeling of MacroP with Gallium-68

Two different methods were used for MacroP radiolabeling.

MacroP1 method: the radiolabeling was performed with Eckert & Ziegler Eurotope Modular Lab Standard® automated synthesis system.

^{68}Ga was eluted from ^{68}Ge/^{68}Ga generator with 6 mL of 0.1 M HCl solution and concentrated on a SCX. $^{68}GaCl_3$ was eluted with 800 µL of 0.02 M HCl in acetone 98% into the reaction vial containing 2 mL of 0.2 M sodium acetate (pH 4) and 0.027 µmol of MacroP.

The reaction was carried out at 95°C for 400 seconds and, after cooling, the solution was manually injected with a syringe in a C18 light reverse phase silica cartridge, preconditioned with ethanol/water 1:1 (v/v). The cartridge was washed with water for removing free ^{68}Ga and the product was eluted with ethanol 50% and diluted in saline.

MacroP2 method: the radiolabeling and purification of MacroP were performed with the Eckert & Ziegler Eurotope Modular Lab Pharm-Tracer® automated synthesis system. The ^{68}Ge/^{68}Ga generator was eluted with 6 mL of 0.1 M HCl solution and $^{68}GaCl_3$ was trapped on the SCX. The radioactive was released from the cartridge to the sample solution with 5.5 M HCl in 5 M NaCl solution.

Solution A was prepared by dissolving 0.29 g of sodium acetate in 2 mL of B.Braun water and adding 128 µL of 30% HCl solution. The sample solution was prepared by mixing 400 µL of solution A with 2 mL of B.Braun water and 15 µL of 0.833 M MacroP solution. The radiolabeling was performed at 95°C for 5 minutes and at the end some saline, stored at 2-8°C overnight, was added for cooling. The purification was performed with a C18 ion exchange cartridge, preconditioned with ethanol/water 1:1 (v/v) and washed with water. The product was eluted from the cartridge with ethanol/water 1:1 (v/v) and diluted in saline.

Determination of MacroP radiochemical purity (RCP)

The radiochemical purity of MacroP was determined by ITLC and by RP-HPLC.

The ITLC was performed on ITLC-SG paper strips and using 2 different mobile phases: 0.1 M sodium citrate buffer (pH = 5) and 1 M $AcONH_4$ in water/methanol 1:1 (v/v). The sample application volumes were 5 µL.

The radiochromatographic profile was determined by an autoradiographic system that uses a high performance storage phosphor screen.

Two RP-HPLC methods were used for the ^{68}Ga-MacroP analysis.

RPH1 method: RP-HPLC was performed on a Merck Hitachi LaChrom L-7100/L7100 HPLC with a L-7400 UV-visible detector and a Radiomatic 150TR flow scintillation analyzer, with Vydac Everest C18, 5 µm, 4.6 x 150 mm, 300 Å as stationary phase. For MacroP analysis, a gradient method at a flow rate of 1 mL/min was applied. The gradient mixture was composed of 0.1% aqueous TFA (solvent A) and 0.1% TFA in acetonitrile gradient grade (solvent B). Linear gradient from 6% to 16% B in 10 min. Post run to 6% B: 3 min. The injection volume was 20 µL. The chromatograms were acquired at 220 nm wavelength.

RPH2 method: RP-HPLC was performed on a UltiMate 3000 UHPLC systems with a Dionex UltiMate 3000 variable wavelength detectors and GABI Star (Raytest).

Reverse-phase HPLC chromatography was carried out using a Pursuit C18, 3 µm 3.0 x 150 mm, 200 Å column. For MacroP analysis, a gradient method at a flow rate of 0.6 mL/min was applied. The gradient mixture was composed of 0.1% aqueous TFA (solvent A) and 0.1% TFA in acetonitrile gradient grade (solvent B). Gradient elution: 0-2 min 100% B; 2-7 min linear gradient from 100% to 40% B; 7-12 min 40% B. Post run to 100% B: 1 min, and 2 min waiting time. The injection volume was 20 µL. The chromatograms were acquired at 220 nm wavelength.

Cell culture

Human Umbilical Vein Endothelial Cells (HUVEC) were obtained from human umbilical cords collected from full-term women immediately after cesarean section at the Gynecology and Obstetrics department of International Evangelic Hospital in Genoa, with informed consent using the guidelines approved by the Institutional Committee. Each cord vein was individually processed for obtaining endothelial cells through mechanical dissociation of the tissue and collagenase digestion.

Cells were maintained in culture medium EndoGRO-LS Complete Culture Media Kit seeded on attachment factor-coated plates.

For labeling experiments $8x10^5$ cells were plated in Petri dishes in EndoGRO Basal Medium (SCME-BM) and allowed to attach overnight prior stimulation with 20 ng/mL of TNF-alpha (TNF-α). Cells without TNF-α treatment served as control.

RNA extraction and quantitative real-time PCR (qRT-PCR)

Total RNA was extracted using the high pure RNA isolation kit, according to the manufacturer's instruction, and reverse transcribed into cDNA using the iScript cDNA synthesis kit.

Single stranded cDNA products were analyzed by real-time PCR using the SsoFast™ EvaGreen mix on a CFX96 Touch real-time PCR.

Cycling conditions were set at 94° C for 30 s, 60°C for 30 s and 72° C for 30 s, for 37 cycles.

The specific primer pairs used for polymerase chain reaction amplification were designed on the mature transcripts and are shown in Table 6.

Table 6: List of primer designed for the quantification of specific mRNAs by qRT-PCR in HUVECs

mRNA species	Sense	Sequence 5'-3'
Human VCAM-1	Forward	GACCACATCTACGCTGAC
	Reverse	GCAACTGAACACTTGACTG
GAPDH	Forward	ACCCACTCCTCCACCTTTGA
	Reverse	CTGTTGCTGTAGCCAAATTCGT
28S	Forward	CCCAGTGCTCTGAATGTCAA
	Reverse	AGTGGGAATCTCGTTCATCC

Levels of target genes in each sample were normalized on the basis of glyceraldehyde-3-phosphate dehydrogenase (GAPDH) and 28S amplification and reported as relative values. All qRT-PCR runs included negative controls without mRNA templates and cDNA transcription to check reagents for contaminations.

Fluorescence active cells sorting (FACS) analysis of cell adhesion molecule expression

The surface expressions of VCAM-1 on HUVECs were evaluated by a flow cytometry analysis using a fluorescence-activated cell sorter system.

After stimulation with 20 ng/ml TNF-α, the time-course experiment was performed by FACS analysis at time 0, 4h, 18h and 24h. Control and TNF-α stimulated HUVEC were detached with trypsin, washed in PBS and analyzed for VCAM-1 expression using the antibody CD106 (VCAM-1) conjugated with the fluorescent dye phycoerythrin. Appropriate IgG isotype-matched antibodies and unstained cells were used as negative control. Data were acquired on BD FACSCanto II and analyzed by BD FACSDiva software.

NAMP-avidin-^{68}Ga-BisDOTA in vitro test on TNF- α stimulated HUVEC

After removing TNF- α from the culture medium, HUVEC were incubated at 37°C with 4 nmol of NAMP for 20 minutes and afterwards with 3.5 nmol of avidin for 10 minutes. After washing and replacing the culture medium, the binding assay of ^{68}Ga-BisDOTA with the NAMP-avidin complex, bound to the VCAM-1 expressed on HUVEC, was monitored using LigandTracer® White, according to the manufacturer's instructions.

Culture dish, containing 4 mL cell culture medium, was placed on the cell dish holder of the instrument and before starting the assay, 6 MBq of ^{68}Ga-BisDOTA were added to the culture medium. The binding of radioactivity to cell-containing areas and reference areas was recorded. The same procedures were also applied to a control dish seeded with unstimulated HUVEC.

^{68}Ga-MacroP in vitro test on TNF- α stimulated HUVEC

The binding assay of ^{68}Ga-MacroP with VCAM-1 expressed on HUVEC was monitored using LigandTracer® White, according to the manufacturer's instructions.

Culture dish, containing 3 mL cell culture medium, was placed on the cell dish holder of the instrument and before starting the assay, the culture medium was replaced with 3 mL of the saline solution containing 5MBq of ^{68}Ga-MacroP. The binding of radioactivity to cell-containing areas and reference areas was recorded. The same procedures were also applied to a control dish seeded with unstimulated HUVEC.

RESULTS AND DISCUSSION

NAMP-avidin- BisDOTA binding

With the aim of exploiting the strong affinity of the biotin-avidin system, our idea was to use NAMP for a 3-steps or 2-steps pretargeting.

In 3-steps pretargeting NAMP should be injected in vivo first, in order to target the VCAM-1 expressed on the surface of endothelial cells in correspondence of the atherosclerotic lesion, followed by avidin injection, and finally by the injection of a radiolabeled biotin. Generally in this kind of pretargeting must be also considered a chasing step, for example with biotinylated albumin for removing unbound avidin from the blood.

In 2-steps pretargeting, NAMP, previously bound to avidin in a molar ratio of 1:1, should be injected to target the VCAM-1 expressed on the endothelial cells, followed by the parenteral administration of a radiolabeled biotin.

As radiolabeled biotin, a modified biotin by conjugation with two molecules of DOTA (BisDOTA) was used (Fig. 82).

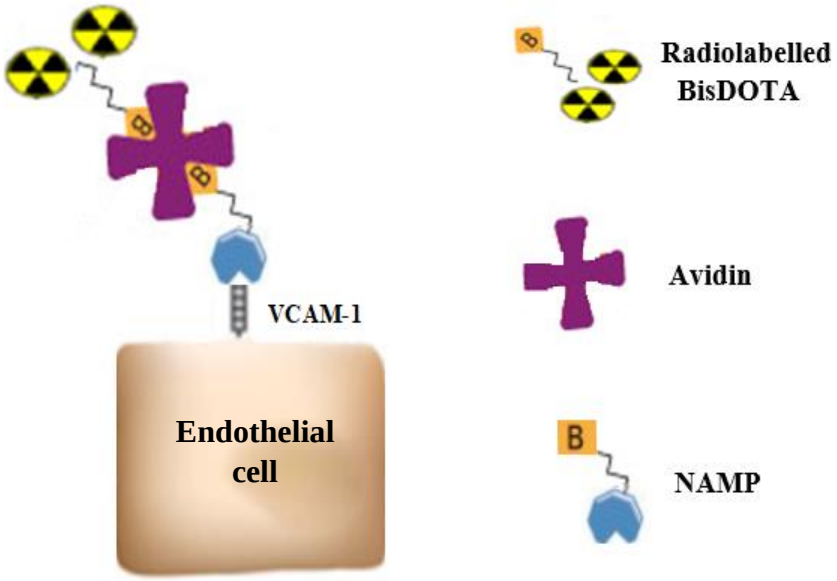

Fig. 82: NAMP pretargeting system.

Since only a small percentage of radioactivity really localizes on the lesion, it is important that the biotin is labeled with a high specific activity. Generally, the maximum allowed stoichiometry of a DOTA-conjugated molecule is one metallic radionuclide per molecule, and this may limit the imaging detection of VCAM-1 presence on the tissue. We thought to increase the potentiality of this diagnostic approach using biotin derivatives carrying at least two DOTA groups, that can be labeled with at least two radionuclides to increase the radionuclide signal localized on the receptor.

Pratesi et al. [62] synthesized several biotin derivatives carrying two DOTA groups per molecule (BisDOTA), in order to deliver a higher radiation dose to the tumor, for therapeutically purpose. Substantially, biotin has been modified through bifunctional spacers of different lengths and chemical structures and conjugated with two molecules of DOTA (Fig. 83).

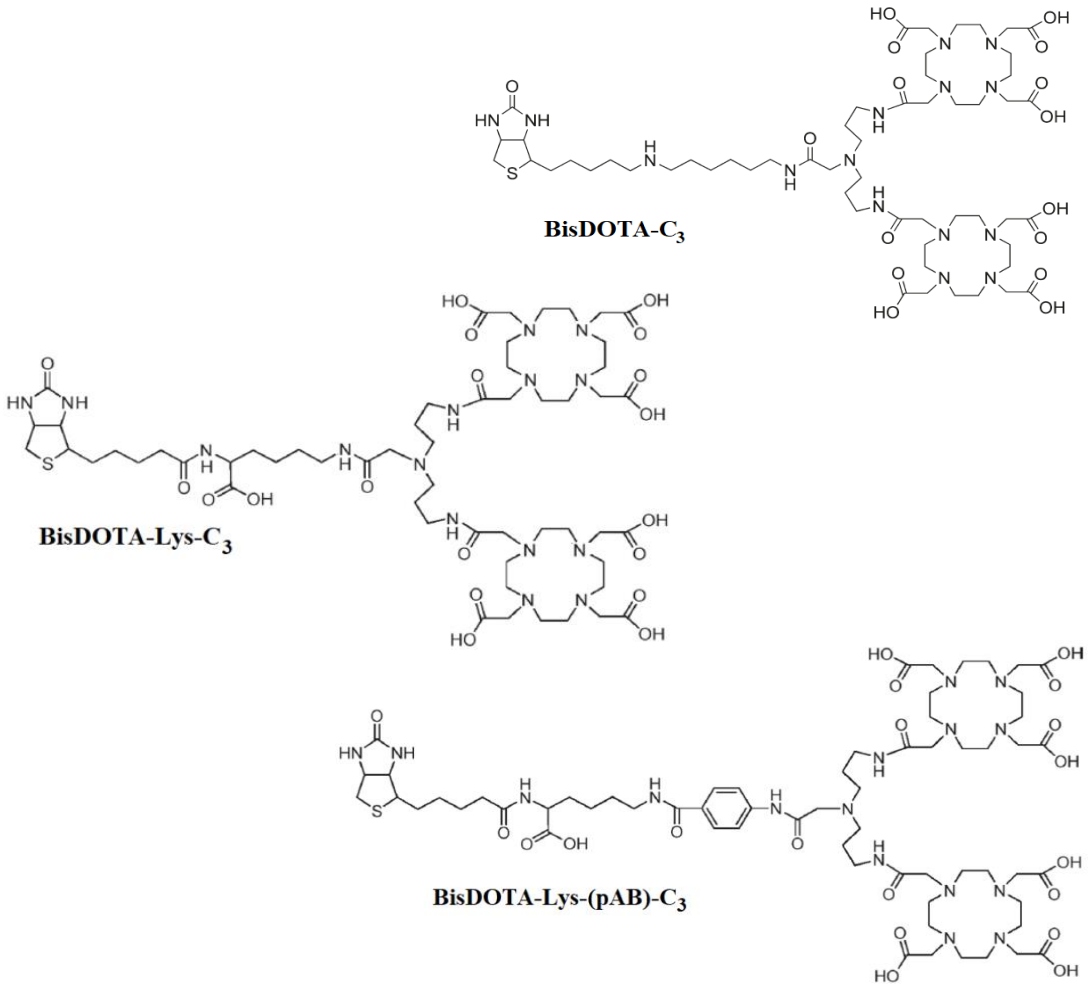

Fig. 83: BisDOTA structures.

The BisDOTA-Lys derivatives showed an avidin binding capacity higher than BisDOTA-C_3 and very similar to the native biotin [62]. For this reasons, BisDOTA-Lys-C_3 was selected for a preliminary binding test with NAMP and avidin.

First, NAMP capability of binding avidin was tested by RP-HPLC and CE.

Since avidin can theoretically bind up to four molecules of biotin, a NAMP/avidin molar ratio of four was applied and, after a 2h incubation, the solution was ultrafiltered on a 30kDa cut-off filter, since the MW of NAMP-avidin complex is 67000 Da.

The ultrafiltrate was analysed by RP-HPLC in order to verify the presence of unbound NAMP, while the retentate was examined by CE.

To assay the possible aspecific binding of NAMP to the filter, ultrafiltration in the absence of avidin was also carried out and the ultrafiltrate was analysed by RP-HPLC.

In Fig. 84, the comparison between the ultrafiltrates is shown: when avidin was used, no detectable unbound NAMP passed through the filter.

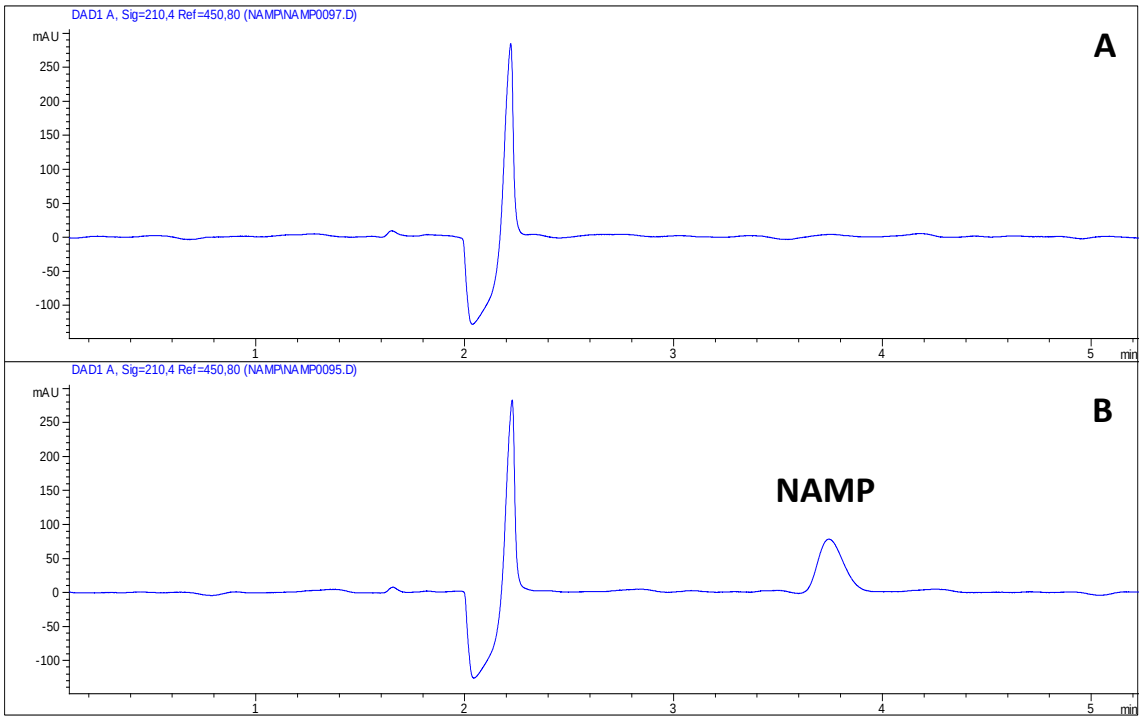

Fig. 84: RP-HPLC comparison between the ultrafiltrates in presence (A) and in absence of avidin (B).

The retentate was analysed by CE and compared with standard solutions of avidin and NAMP.

After establishing the reproducibility of the electrophoretic method by repeated injections of the solutions at different concentrations, it was noted that the electropherogram showed a peak with a t_R slightly different from the avidin peak and with a different peak profile (Fig. 85).

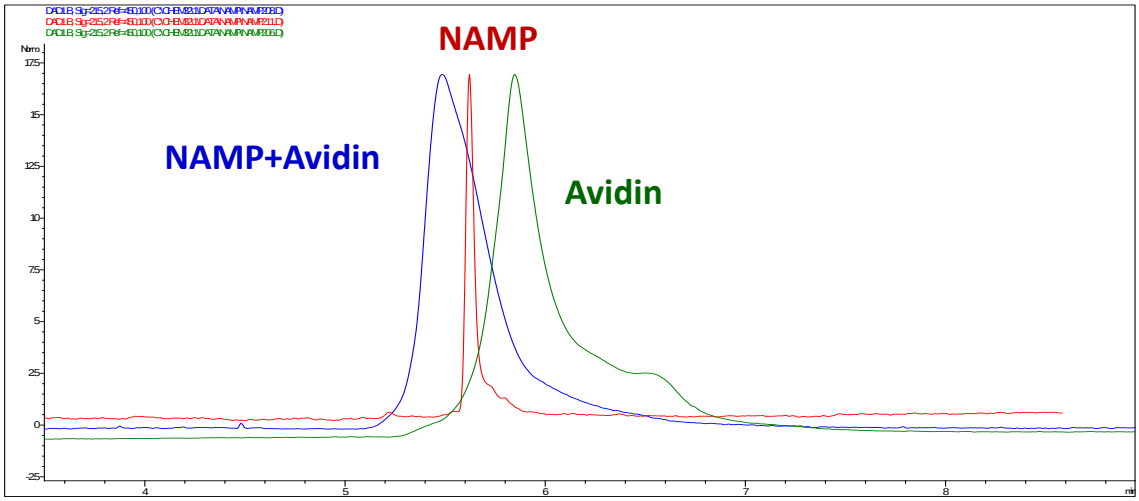

Fig. 85: CE comparison between retentate (blue), NAMP (red) and avidin (green).

Analysing a biotin-avidin complex by CE, the modification in avidin peak profile due to the complexation was evident, although no variation in the t_R was observed (Fig. 86).

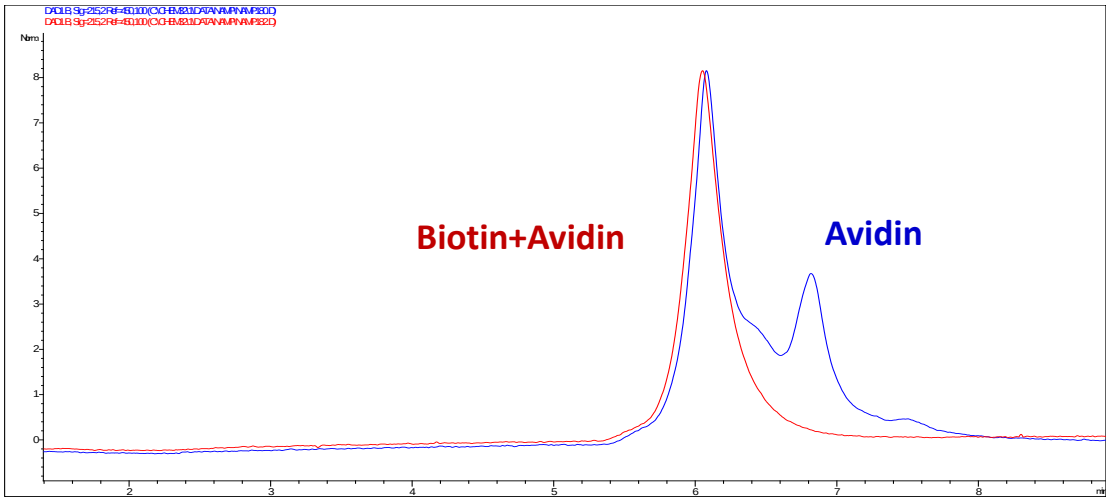

Fig. 86: CE comparison between biotin-avidin (red) and avidin (blue).

This might be explained by considering the mass of the peptide moiety in NAMP, which, influencing the m/z ratio, causes the t_R variation of the NAMP-avidin complex.

On the basis of some papers [63, 64, 65], a study was conducted demonstrate the binding between NAMP and avidin by mass spectrometry.

For observing noncovalent complexes of a protein by ESI-MS, it is necessary to apply specific conditions (“ native conditions”) in order to avoid protein denaturation and, in the case of avidin, the dissociation of the tetrameric structure, itself a noncovalent association of four subunits. Briefly the conditions were:

- dissolve the sample using solution conditions closer to those of physiological interest and more suitable for preserving weak structural associations [63];
- use of an extended mass-to-charge ratio instrumental range (> 3000), essential for the observation of the active form of avidin, and, thereby, the avidin-biotin complex [64];
- careful manipulation of the inlet capillary heating in order to observe noncovalent complexes by ESI-MS and to avoid the dissociation of the noncovalent tetramers of avidin into the individual subunits [64].

The retentate was diluted 1:4 in aqueous 10 mM ammonium acetate buffer at pH 8 (conc. about 0.1 mg/mL) and analysed by Orbitrap, without success. Probably a better setting of the ESI conditions has to be developed.

To the retentate of NAMP-avidin ultrafiltration, a BisDOTA solution was added in order to verify the formation of NAMP-avidin-BisDOTA complex by CE.

From the comparison between the electropherograms of the reaction mixture and of a BisDOTA solution at the same concentration, it is possible to note that the BisDOTA peak disappears in the presence of NAMP-avidin complex (Fig. 87).

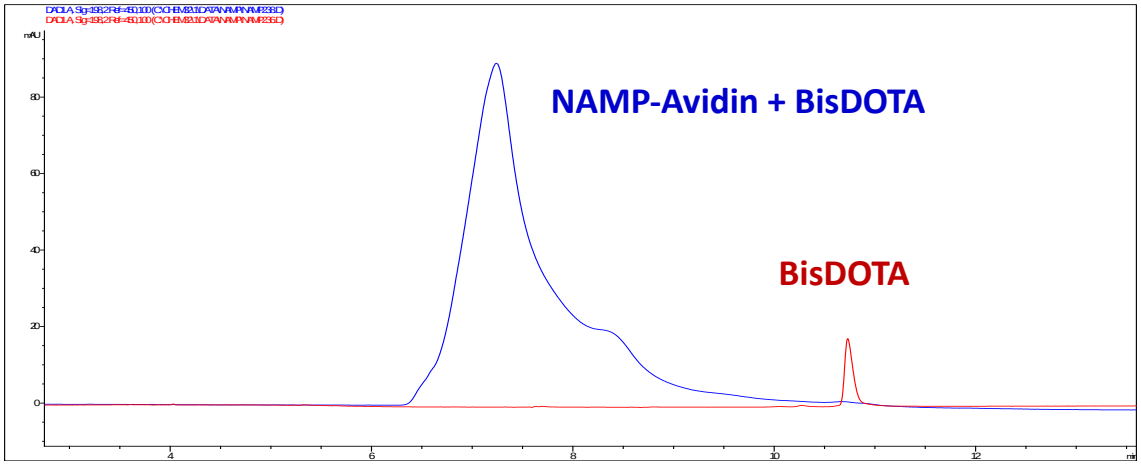

Fig. 87: CE comparison between NAMP-avidin + BisDOTA and a BisDOTA standard solution.

A further test was performed, mixing NAMP, avidin and BisDOTA for 1h at 37°C and ultrafiltering the solution as described before.

In Fig. 88 the comparison between the electropherograms of the ultrafiltrate and of BisDOTA and NAMP standard solutions is shown: within the limits of detection of the applied method, BisDOTA and NAMP were not found in the ultrafiltrate.

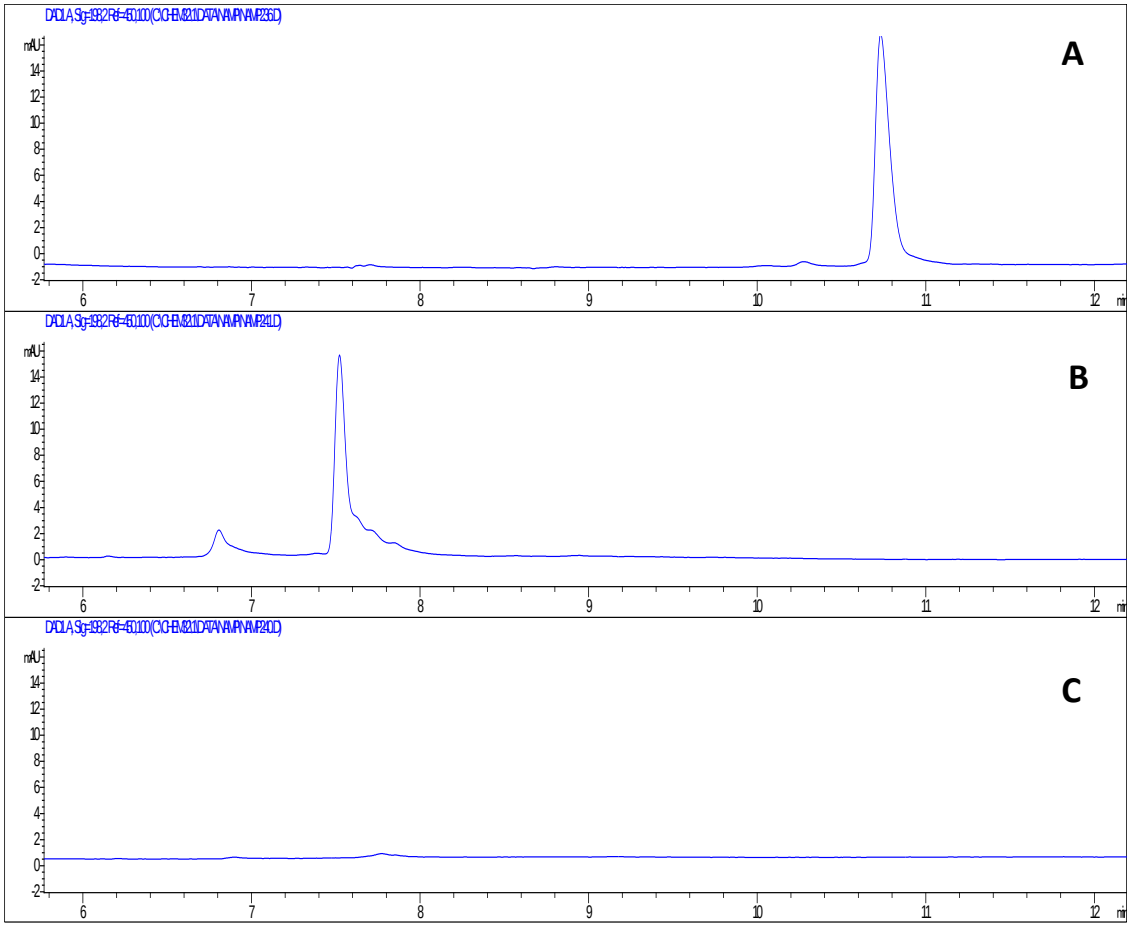

Fig. 88: CE comparison between BisDOTA (A) and NAMP(B) standard solutions and the ultrafiltrate from NAMP, avidin and BisDOTA mixture (C).

The retentate was analysed by CE, but no significant differences were found in comparison with the electropherogram of the NAMP-avidin complex.

Radiolabeling of BisDOTA

BisDOTA was radiolabeled with ^{68}Ga by using *BisDOTA1 method*, in order to develop a preliminary test for evaluating the formation of NAMP-avidin-radiolabeled BisDOTA complex.

The radiolabeling was performed in collaboration with the IEO, using the Eckert & Ziegler Eurotope Modular Lab Standard® automated synthesis system.

This system, designed specifically for the synthesis of radiopharmaceuticals, is made of three parts: the modules assembled according to the specific radiopharmaceutical being synthesized; the synthesis cassette on which the appropriate chemicals, reagents, filters, column etc. are attached; and the computerized system that runs the modules which in turn run the valves and syringes on the cassette, producing the required radiopharmaceutical.

After the radiolabeling, it was necessary to set up an ITLC method for product control.

The method should be able to distinguish the free radiolabeled BisDOTA from the BisDOTA bound to the complex. To this purpose, it was decided to use a reverse stationary phase and three different mobile phases were tested in order to obtain the migration of free radiolabeled BisDOTA, and its complex remaining at the starting line. The mobile phase were saline:acetone 1:1, 1M aqueous ammonium acetate buffer:methanol 1:1 and saline:acetonitrile 1:1.

The mobile phase in which the radiolabeled BisDOTA was able to migrate with a higher Rf was the third, so this mobile phase was selected for the complex analysis.

Fig. 89 shows the ITLC comparison between radiolabeled BisDOTA and NAMP-avidin-radiolabeled BisDOTA complex. A shift of the radiolabeled product Rf from 0.6 to 0 occurred and, since avidin does not migrate under the applied chromatographic conditions, this preliminary test can be considered as a positive result.

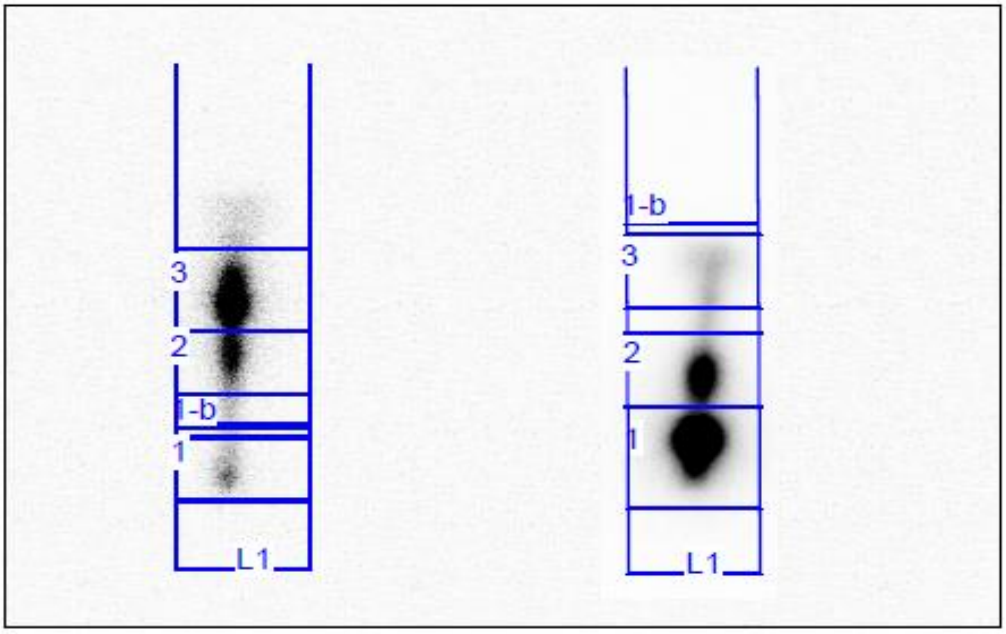

Fig. 89: ITLC comparison between ^{68}Ga-BisDOTA (left) and NAMP-avidin-^{68}Ga-BisDOTA complex (right).

In order to perform an *in vitro* test on endothelial cells, optimized ^{68}Ga-BisDOTA radiolabeling and purification procedures were performed at the San Martino's Hospital of Genoa.

The *BisDOTA2 method* was applied and the radiochemical purity of the product was analyzed by RP-HPLC (Fig. 90).

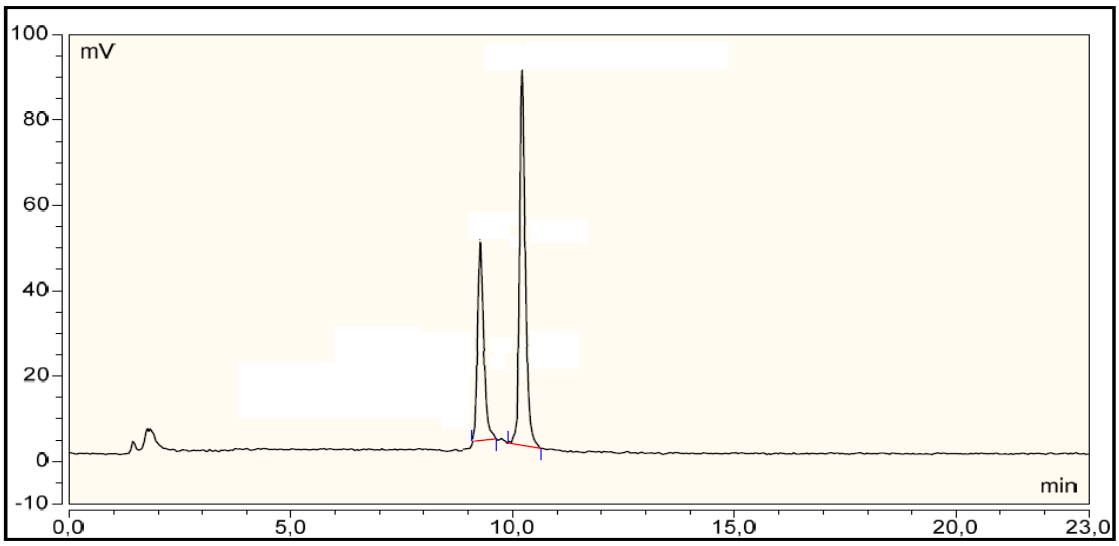

Fig. 90: RP-HPLC of ^{68}Ga-BisDOTA.

Since the chromatogram showed two peaks, it was supposed that they could be related to the mono-radiolabeled and bis-radiolabeled BisDOTA.

Although more analysis should be carried out, the in vitro test on TNF-α stimulated HUVEC was performed.

MacroP binding with VCAM-1

MacroP ability of binding VCAM-1 was tested by CE. MacroP and VCAM-1 were mixture in equimolar amount and after 400 rpm stirring at 37°C for 2 h, the solution was analyzed by CE and compared with a MacroP standard solution at the same concentration (Fig. 91)

It's possible to note a decrease of MacroP peak after the incubation with VCAM-1, which indicated the affinity of MacroP to VCAM-1.

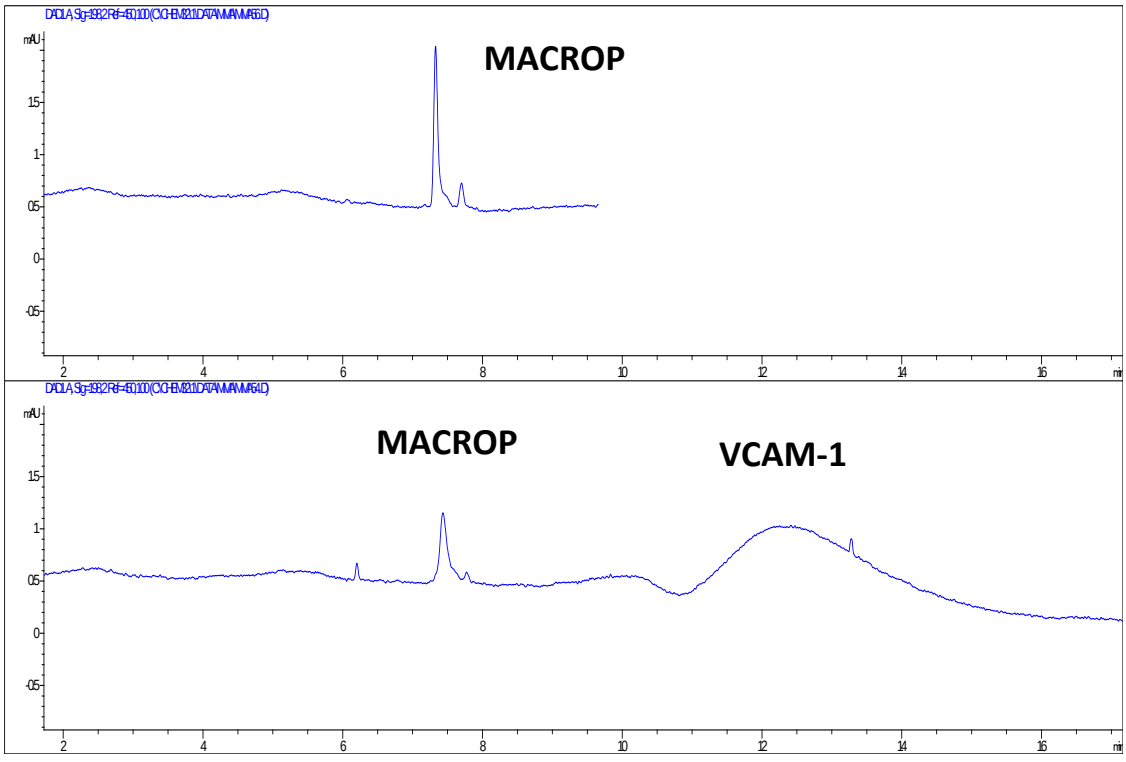

Fig. 91: CE comparison between MacroP standard solution and MacroP-VCAM-1 complex.

Radiolabeling of MacroP

Firstly, MacroP radiolabeling was performed in collaboration with the IEO, using the Eckert & Ziegler Eurotope Modular Lab Standard® automated synthesis system.

The used radiolabeling conditions were very similar to those applied for the synthesis of ^{68}Ga-DOTATOC, a radiopharmaceutical used for neuroendocrine tumors diagnosis (NETs). Its structure includes a molecule of DOTA conjugated with an octapeptide, analogue of somatostatin, able to bind various subtypes of somatostatin receptors over-expressed by NETs (Fig. 92).

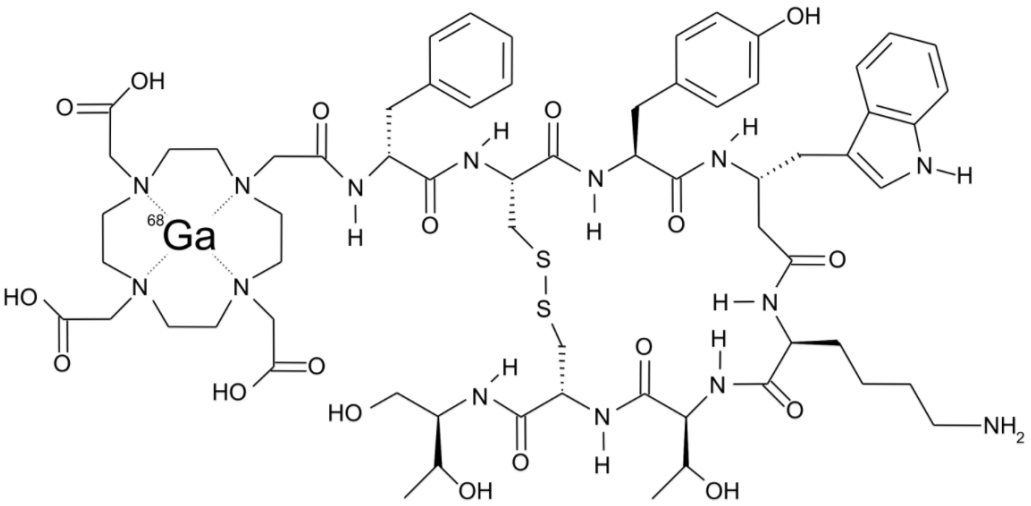

Fig. 92: Structure of ^{68}Ga-DOTATOC.

For ^{68}Ga-DOTATOC radiolabeling and purification, mainly two methods are used: the acetone-based labeling procedure and the Mueller method, that differs for the solvent used for the elution of ^{68}Ga from the SCX.

Briefly, after the elution of ^{68}Ge/^{68}Ga from the generator, ^{68}Ga is trapped on the SCX while ^{68}Ge and other metallic impurities are eluted in the waste.

By the acetone method, ^{68}Ga is eluted from the SCX with a 0.02 M HCl solution in 98% acetone into the reaction vial containing the DOTATOC peptide dissolved in acetate buffer.

By the Mueller method, ^{68}Ga is eluted using a mixture of 12.5 μL of 5.5 M HCl solution and 500 μL of 5 M NaCl solution. This method was introduced to avoid the presence of traces of acetone in the final product.

Since the radiopharmaceutical laboratory of the IEO uses the acetone method for ^{68}Ga-DOTATOC radiolabeling, a similar method was applied for MacroP radiolabeling (*MacroP1 method*).

Before radiolabeling, to assess MacroP stability to the reaction conditions, the compound was dissolved in 0.2 M ammonium acetate buffer (pH 4), 800 µL of 0.02 M HCl acetone solution were added, and the mixture was heated at 95°C for 400 seconds; after cooling, a RP-HPLC was carried out using a standard MacroP solution at lower concentration as reference, and no differences were found.

Subsequently, MacroP was radiolabeled and directly analysed by ITLC and RP-HPLC, before purification.

For the ITLC analysis, two different mobile phases were used:

-0.1 M sodium citrate buffer (Fig. 93) in which the product does not migrate, while free gallium migrates with the solvent front;

-1 M ammonium acetate in water/methanol 1:1 (Fig. 94) in which the hydrolysed gallium remains at the application line, while the product migrates.

The product RCP resulted to be higher than 97% with both methods.

The product was also analysed by RP-HPLC using the *RPH1 method* and the obtained RCP resulted to be higher than 90% (Fig. 95).

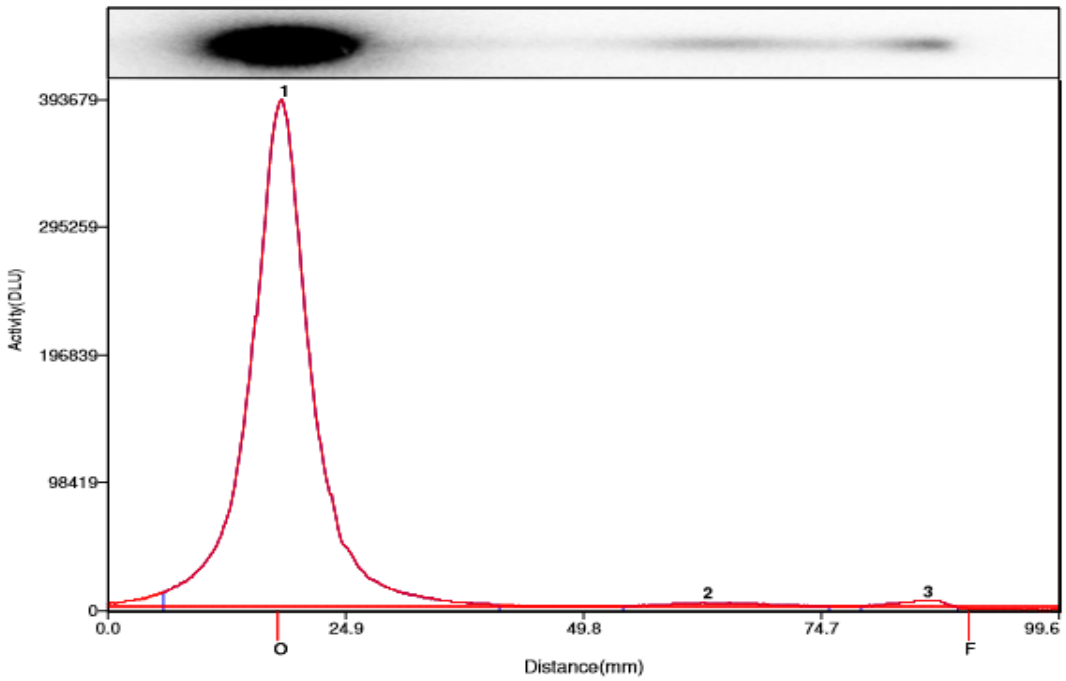

Fig. 93: ITLC of raw ^{68}Ga-MacroP in 0.1 M sodium citrate buffer.

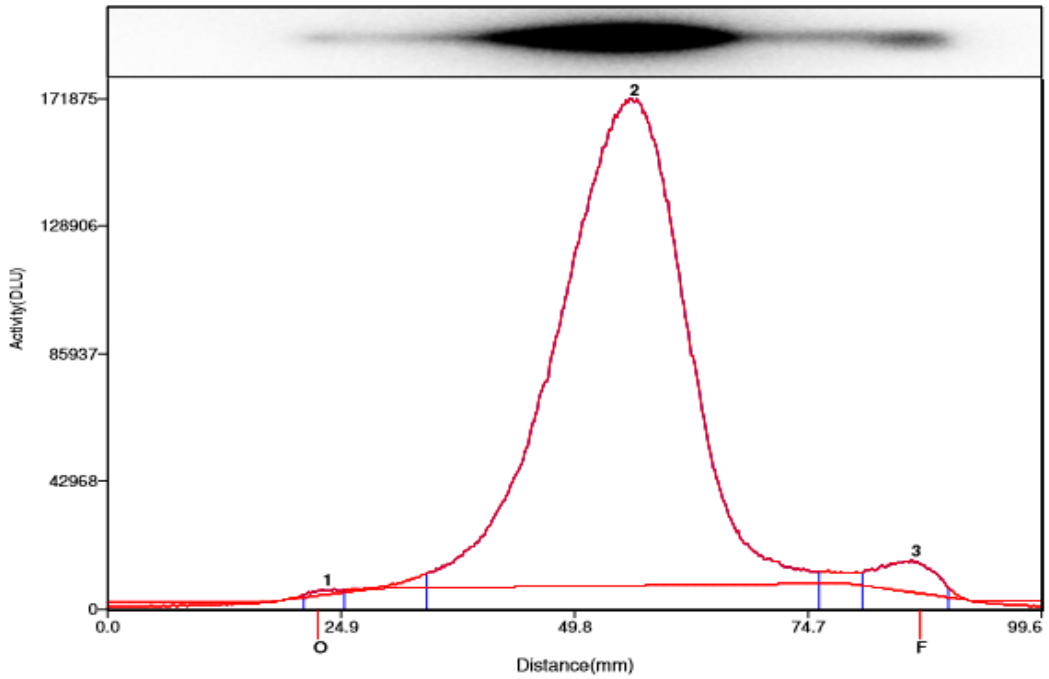

Fig. 94: ITLC of raw ^{68}Ga-MacroP in 1 M ammonium acetate in water/methanol 1:1.

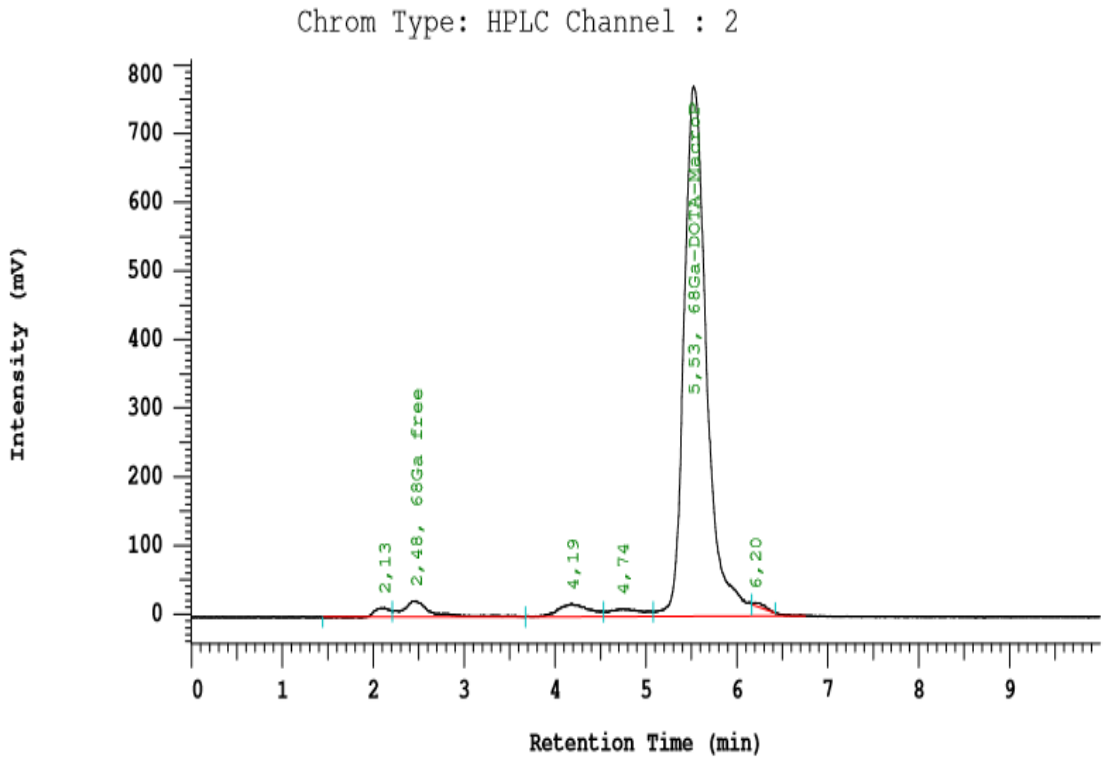

Fig. 95: RP-HPLC of raw ^{68}Ga-MacroP.

Although the product was fairly pure, it was manually injected in a C18 light reverse phase silica cartridge for purification, but, unlike ^{68}Ga-DOTATOC, ^{68}Ga-MacroP was not retained in the cartridge at the applied conditions.

Assuming that the failure of the purification procedure could be ascribed to traces of acetone still contained in the product, MacroP radiolabeling was repeated using the *MacroP2 method*, deriving from the Mueller one with slight modifications, performed in the radiopharmacy laboratory of Sant'Andrea hospital in La Spezia.

This time the product purification was successfully obtained, with a RCP, measured by ITLC, higher than 96%.

A preliminary stability test of the product in saline, performed by ITLC analysis at room temperature at 0, 2, 3 and 4h (Table 7), gave positive results.

Table 7: Stability study of ^{68}Ga-MacroP in saline.

Time (hour)	RCP (%)
0	96.6
2	95.6
3	95.9
4	95.9

The obtained radioactivity yield (see "Definition and terminology") was 45%, so some modifications of the radiolabeling procedure were attempted to enhance it.

First, the amount of MacroP was increased and secondly a cooled saline was employed for the final elution of the product, in order to increase the C18 cartridge performance.

The new radioactivity yield was 57% with a RCP equal to 97%, when calculated by ITLC, and of 99%, when measured by RP-HPLC *RPH2 method* (Fig. 96).

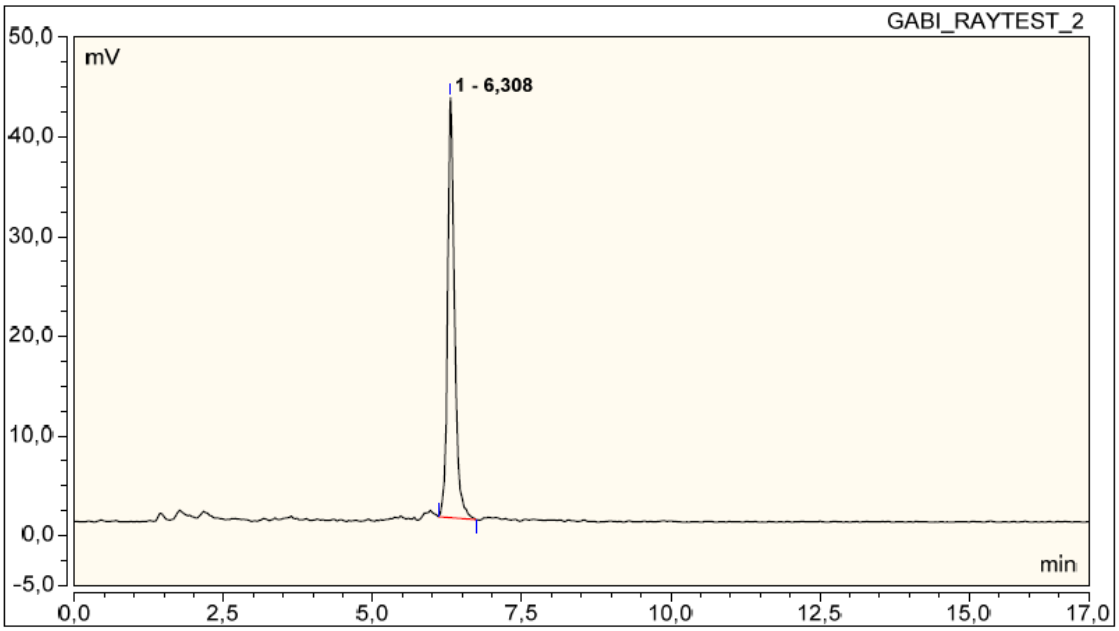

Fig. 96: RP-HPLC of pure ^{68}Ga-MacroP.

The radiolabeling and purification procedures optimized at Sant'Andrea Hospital have been transferred to San Martino's Hospital in order to perform an *in vitro* test on endothelial cells.

In this case, the radioactivity yield was quite low, approx. 40%; however, since only very small amounts of radioactivity are necessary for *in vitro* tests, the product was used anyway.

In vitro cell tests

In vitro cell tests were performed on human umbilical vein endothelial cells (HUVEC) stimulated overnight with 20 ng/mL TNF-α, for the expression of VCAM-1.

The expression of VCAM-1 on HUVECs was evaluated after TNF- α stimulation for 4, 18 and 24 hours by qRT-PCR and FACS analysis.

To assess the VCAM-1 mRNA level in HUVECs, a quantitative assay utilizing reverse transcription–polymerase chain reaction was performed. As shown in Fig. 97, TNF-α incubation showed a stimulatory effect on VCAM-1 mRNA levels in HUVECs as corrected by GAPDH and 28S transcripts.

The maximum of the VCAM-1 expression was observed within 18h stimulation, then the mRNA expression descended.

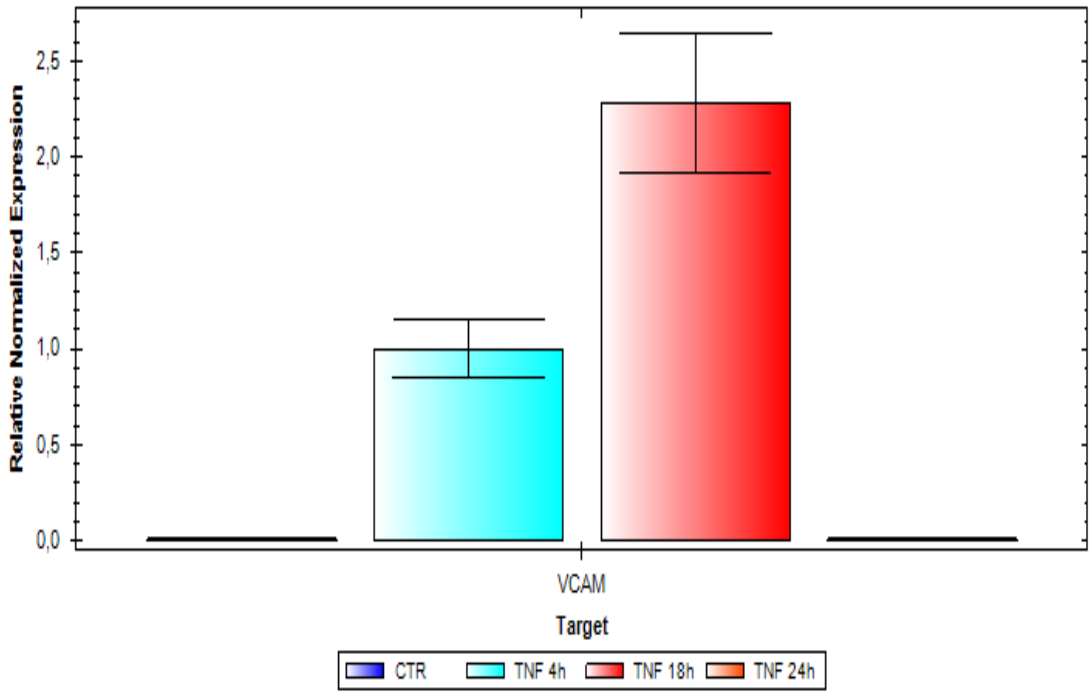

Fig. 97: VCAM-1 mRNA expression on HUVEC before (CTR) and after TNF- α stimulation for 4, 18 and 24 hours.

This result was confirmed by flow cytometry analysis of the surface expression of VCAM-1 on HUVECs at 0, 4, 18 and 24 h TNF- α stimulation, using the antibody CD106 (VCAM-1) conjugated with the fluorescent dye phycoerythrin.

Histograms in Fig. 98 plot the fluorescence intensity (on the x-axis) against the cell count (on the y-axis). The P3 gate identify a region of the plot in which the cells are vital and show a high fluorescence intensity, which is related to an increased VCAM-1 expression. An increase of the fluorescent intensity is visible at 4h and mostly at 18h, while it decreases at 24h.

This is more marked by the comparison between the % total of vital cells and the mean fluorescent intensity at 0, 4, 18 and 24 h TNF- α stimulation of HUVEC (Table 8).

While, the % of total vital cells is approximately similar for 4, 18 and 24h stimulation, the mean fluorescent intensity is higher at 18h and decreases drastically at 24h.

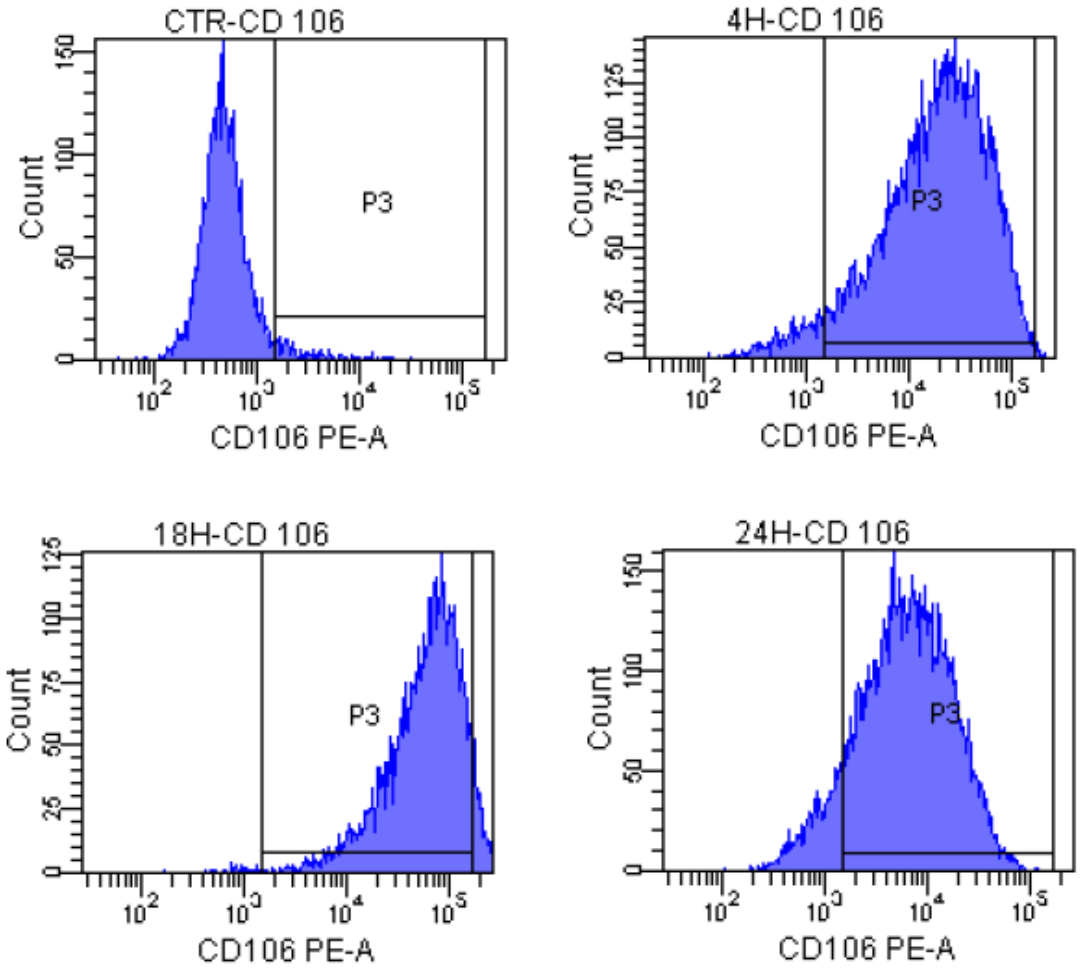

Fig. 98: Flow cytometric histogram for control cells (upper plot on the left), 4h (upper plot on the right), 18h (lower plot on the left) and 24h (lower plot on the right) TNF-α stimulated HUVECs.

Table 8: Comparison between the % of total vital cells and the mean fluorescent intensity for TNF-α stimulated HUVEC at different times.

TNF-α stilmulation time (h)	**% total cells**	**Mean fluorescent intensity**
0 (CTR)	2.8	4.348
4	71	31.338
18	63	69.394
24	73.2	10.778

For NAMP *in vitro test*, TNF- α stimulated and unstimulated HUVEC were incubated with NAMP and subsequently avidin, before adding 6 MBq of ^{68}Ga-BisDOTA in 4 mL of the culture medium.

Regarding MacroP, since the ^{68}Ga-MacroP specific radioactivity (see "Definition and terminology") was lower than ^{68}Ga-BisDOTA's, the culture medium was replaced with 3 mL of the saline solution containing 5 MBq of radiolabeled MacroP.

The results were analysed by using the *Ligandtracer® technology*, based on repeated differential measurements of surface-associated proteins.

Cells are seeded in a local part of a cell dish and the opposite side is used as a reference. The dish is placed on an inclined, slowly rotating support and the liquid containing the labeled ligand is added (Fig. 99).

The detector, mounted over the upper part, registers the additional activity of molecules bound to the cells. Each revolution results in a peak, which is an accurate measurement of the amount of bound. The peak height is followed over time, providing an accurate estimation of the kinetics of the interaction.

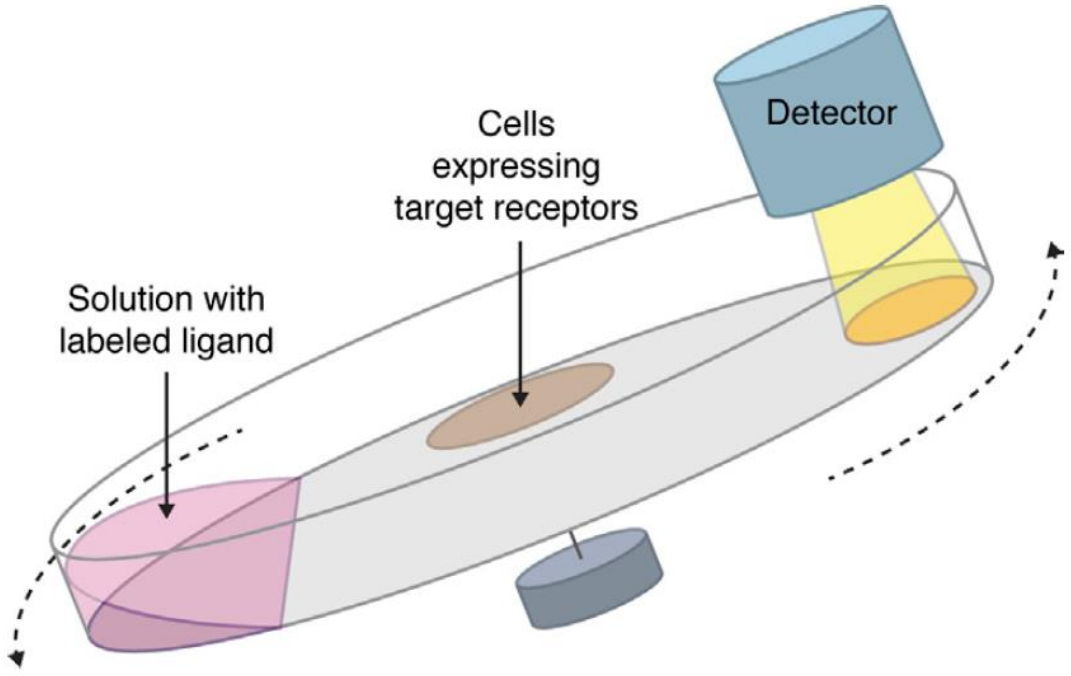

Fig. 99: Operating mechanism of ligand tracer.

By a reprocessing of the instrument's data, it is possible to obtain a comparison plot between the radioactivity signal, subtracted by the background signal, of the TNF-α stimulated and unstimulated HUVEC (control cells).
An increase of the signal is related to the uptake of the radioactivity by the cells, that is not visible in the control cells.

Fig. 100 and Fig. 101 show the plots respectively of NAMP-avidin-BisDOTA and MacroP in vitro tests.

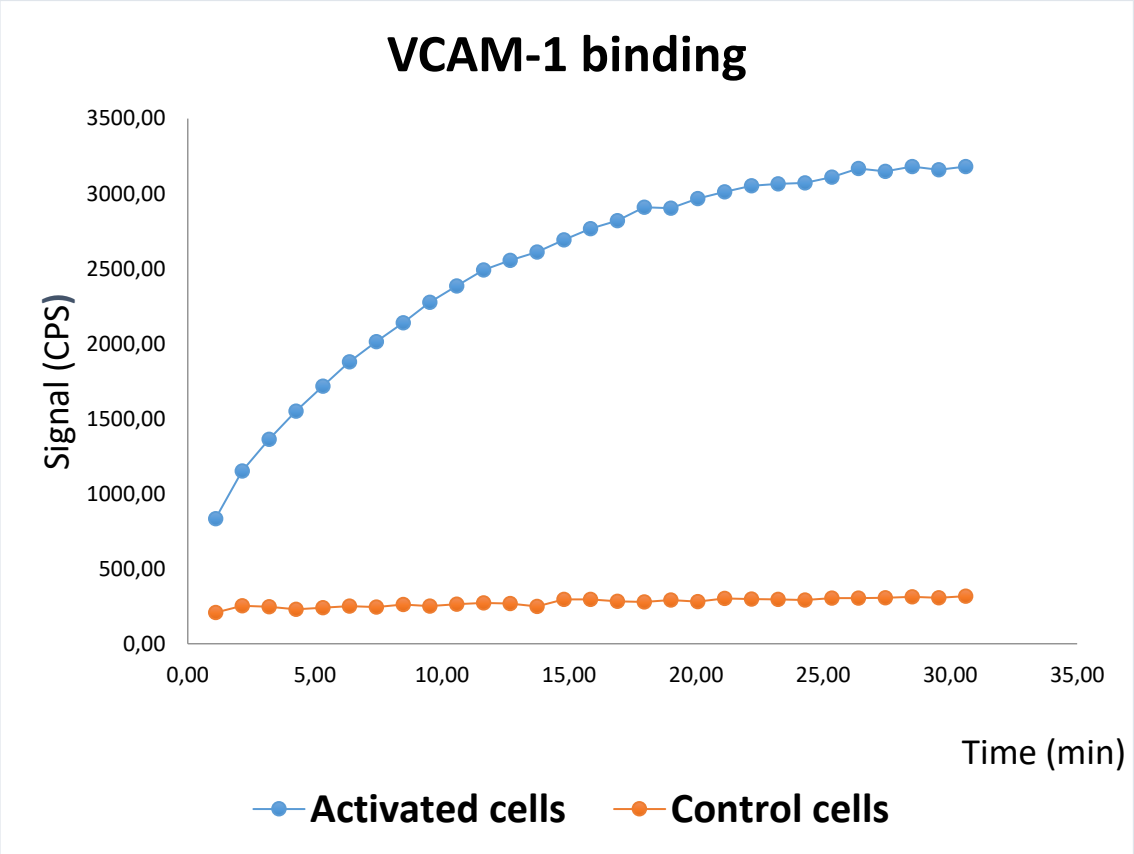

Fig. 100: ^{68}Ga-BisDOTA-avidin-NAMP uptake of activated and unstimulated HUVECs.

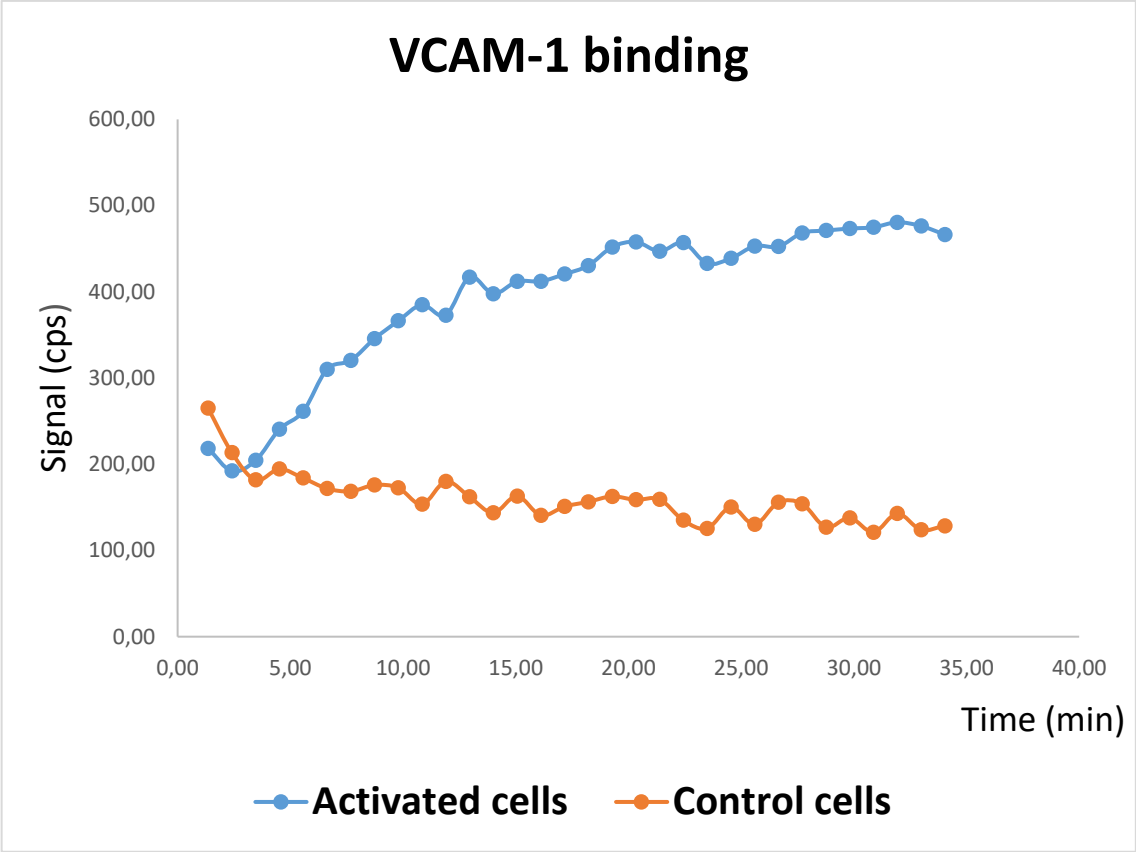

Fig. 101: ^{68}Ga-MacroP uptake of activated and unstimulated HUVECs.

Both synthesized molecules showed the ability to bind VCAM-1 expressed on TNF-α stimulated HUVEC.

Furthermore these tests demonstrated that the affinity of peptide "VHPKQHRGGSKGC" is preserved when it is conjugated with the ^{68}Ga-labeled macrocycle.

CONCLUSIONS

Two new radiopharmaceuticals, NAMP and MacroP, were successfully synthesized and characterized.

In accordance with preliminary tests, NAMP retain the ability to bind avidin, so it might be suitable for a pretargeting, which include the injection of a radiolabeled biotin modified by conjugation with two molecules of DOTA (BisDOTA), in order to increase the radiosignal on the atherosclerotic lesion.

BisDOTA has been successfully radiolabeled with ^{68}Ga, but in future could be complexed with a longer half-life radionuclide more suitable for a pretargeting system with a prolonged circulation time.

In vitro cell tests on NAMP showed the ability of the molecule to bind VCAM-1 expressed on HUVEC and the possibility to use pretargeting for diagnostic imaging. Studies on animal models will be carried out to verify the applicability of this system in vivo, whose main advantage would be the prolonged circulation time of the radiolabeled BisDOTA, with consequent high radioactivity accumulation into the lesion.

The other new radiopharmaceutical, MacroP has been successfully radiolabeled with ^{68}Ga and *in vitro* tests confirmed its ability to bind the VCAM-1.

Since MacroP is a biomolecule with a low molecular weight, it might show short plasma half-life and fast renal clearance, favouring a greater signal-to-noise ratio and a better safety for the patient.

On the other hand, the short circulating time could impair the accumulation of labeled compound on early lesion sites, reducing the radiosignal.

These studies allow to ask the authorization to perform the *ex vivo* tests for both the radiopharmaceuticals, on portions of human artery excised close to the atheromatous plaque, and proceed with *in vivo* test on animal models.

5. Definitions and terminology

Decay correction

Decay correction is used to compute the decay rate or number of particles at a point in time relative to when they were measured. This is necessary when comparing measurements obtained at different points in time. For example, the decay rate of a parent radionuclide is proportional to the number of atoms; as time passes, some of the atoms decay into daughter nuclides, reducing the number of parent atoms.

Radioactive decay corrections are calculated from the exponential equation (see page 98), or from decay tables, or are obtained from a decay curve plotted for the particular radionuclide involved.

Isotopes

Isotopes of an element are nuclides with the same atomic number "Z" but different mass numbers "A". They have similar chemical properties.

Nuclide

An elemental species characterized by (a) its mass number "A", (b) its atomic number "Z" and also by (c) its nuclear energy state.

Radioactivity

The phenomenon of emission of radiation owing to the spontaneous transformation or disintegration of a radionuclide is known as "radioactivity". However, the term "radioactivity" is also used to express the physical quantity (activity or strength) of this phenomenon. The radioactivity of a preparation is the number of nuclear disintegrations or transformations per unit time.

Radioactivity yield

Radioactivity yield is the amount of radioactive product expressed in Bq (MBq, GBq) that is obtained from a starting amount of radioactivity (e.g., eluted from a generator) and is not corrected for decay. A "nondecay-corrected radiochemical yield" in % is significantly dependent on losses due to the technical manipulations used, and on their duration, in addition to the yield of the labeling reaction.

Radiochemical purity

The radiochemical purity is the ratio, expressed as a percentage, of the radioactivity of the radionuclide of interest in a stated chemical form to the total radioactivity of that radionuclide present in the preparation. In the context of radiopharmaceuticals, radiochemical purity is an important quality parameter that needs to be within the stipulated limits. The relevant radiochemical impurities are listed with their limits in the individual Pharmacopoeial monographs for each radiopharmaceutical.

Radiochemical impurities may originate from radionuclide production; subsequent chemical processing; incomplete preparative separation; and chemical changes during storage. In principle, any method of analytical separation may be used in the determination of radiochemical purity. For example, the monographs for radiopharmaceutical products may include paper chromatography, thin-layer chromatography, instant thin-layer chromatography, electrophoresis, size-exclusion chromatography, gas chromatography, and liquid chromatography.

In paper and thin-layer chromatography, a volume equal to that described in the monograph is deposited on the starting line as prescribed in the general methods for chromatography. After development of the chromatogram, the support is dried and the positions of the radioactive areas are detected by autoradiography or by measurement of radioactivity over the length of the chromatogram using suitable collimated counters or by cutting the strips and counting each portion. The positions of the spots or areas permit chemical identification by comparison with solutions of the same chemical substances (non-radioactive) using a suitable detection method. Radioactivity may be measured by integration using an automatic-plotting instrument or a digital counter. The ratios of the areas under the peaks give the ratios of the radioactive concentration of the chemical substances. When the strips are cut into portions, the ratios of the quantities of radioactivity measured give the ratio of concentrations of the radioactive chemical species.

Instant thin-layer chromatography is a rapid, miniaturized thin layer assay method developed to determine the labeling efficiency of radiopharmaceuticals.

The assay uses specific cellulose backed silica gel chromatography strips as solid phase. Its advantages are: it is easy to use, rapid and can be incorporated easily in a routine quality control programme.

Radionuclide

Nuclides containing an unstable arrangement of protons and neutrons transform spontaneously to either a stable or another unstable combination of protons and neutrons with a constant statistical probability by emission of radiation. These are said to be radioactive and are called radionuclides. The initial unstable nuclide is referred to as the "parent radionuclide" and the nuclide after transformation as the "daughter nuclide". Such a transformation is also known as "radioactive transmutation" or "radioactive disintegration" or "radioactive decay".

Radionuclidic purity

The radionuclidic purity is the ratio, expressed as a percentage, of the radioactivity of the radionuclide of interest to the total radioactivity of the radioactive preparation. In the context of radiopharmaceuticals, radionuclidic purity is an important quality parameter and it is mandatory that the radionuclidic impurities are within the stipulated limits. Such radionuclidic impurities arise during the radionuclide production and are, hence, dependent on the production route. In the context of radiopharmaceuticals the acceptable limits for the possible radionuclides are listed in the individual monographs.

Specific radioactivity

The "specific radioactivity", sometimes also referred as "specific activity", is the radioactivity of a radionuclide per unit mass of the element or of the chemical form of the radioactive preparation.

Specific radioactivity is usually calculated taking into account the radioactive concentration (radioactivity per unit volume) and the concentration of the chemical substance being studied, after verification that the radioactivity is attributable only to the radionuclide (radionuclidic purity) and the chemical species (radiochemical purity) concerned.

Units of radioactivity

In the International System (SI), the unit of radioactivity is one nuclear transmutation per second and is expressed in Becquerel (Bq), named after the scientist Henri Becquerel. The old unit of radioactivity was Curie (Ci), named after the scientists Marie Curie and Pierre Curie, the pioneers who studied the phenomenon of radioactivity.

One Ci is the number of disintegrations emanating from 1 g of Radium-266, and is equal to 3.7×10^{10} Bq.

Absolute radioactivity measurements require a specialized laboratory, but identification and measurement of radiation can be carried out relatively by comparison with standardized preparations provided by reference laboratories recognized by international or national authorities.

Yield of reaction

The yield of a reaction is the amount of the product in a reaction. The percentage yield is calculated by the ratio between the weight of product obtained after purification and the theoretical weight of product, calculated by the moles of limiting reagent, per cent.

6. BIBLIOGRAPHY

1. Douglas G. and Channon K.M. *The pathogenesis of atherosclerosis.* Medicine (2014); 42(9):480-484.
2. Lusis A.J. *Atherosclerosis.* Nature (2000); 407(6801):233–241.
3. Zmysłowski A. and Szterk A. *Current knowledge on the mechanism of atherosclerosis and pro-atherosclerotic properties of oxysterols.* Lipids in Health and Disease (2017); 16:188.
4. Huo Y., Hafezi-Moghadam A. and Ley K. *Role of vascular cell adhesion molecule-1 and fibronectin connecting segment-1 in monocyte rolling and adhesion on early atherosclerotic lesions.* Circulation Research (2000); 87:153-159.
5. Yu X.H., Fu Y.C., Zhang D.W., Yin K. and Tang C.K. *Foam cells in atherosclerosis.* Clinica Chimica Acta (2013); 424:245–252.
6. Moore K., Sheedy F. and Fisher E. *Macrophages in atherosclerosis: a dynamic balance.* Nature Reviews Immunology (2013); 13(10):709–721.
7. Rensen S.S.M., Doevendans P.A.F.M. and van Eys G.J.J.M. *Regulation and characteristics of vascular smooth muscle cell phenotypic diversity.* Netherlands heart journal (2007); 15:100–8.
8. Anlamlert W., Lenbury Y. and Bell J. *Modelling fibrous cap formation in atherosclerotic plaque development: stability and oscillatory behaviour.* Advances in Difference Equations (2017); 2017:195.
9. Falk E. *Pathogenesis of Atherosclerosis.* Journal of the American College of Cardiology (2006); 47:C7–12.
10. Lafont A. *Basic aspects of plaque vulnerability.* Heart (2003); 89:1262–1267.
11. Finn A.V., Nakano M., Narula J., Kolodgie F.D. and Virmani R. *Concept of vulnerable/unstable plaque.* Arteriosclerosis, thrombosis, and vascular biology (2010); 30:1282-1292.
12. Stefanadis C., Antoniou C.K., Tsiachris D. and Pietri P. *Coronary atherosclerotic vulnerable plaque: current perspectives.* Journal of the American Heart Association (2017); 6:e005543.
13. Gallino A., Stuber M., Crea F., Falk E., Corti R., Lekakis J., Schwitter J., Camici P., Gaemperli O., Di Valentino M., Prior J., Garcia-Garcia H.M., Vlachopoulos C., Cosentino F., Windecker S., Pedrazzini G., Conti R., Mach F., De Caterina R. and Libby P. *"In vivo" imaging of atherosclerosis.* Atherosclerosis (2012); 224:25-36.

14. Joshi F.R., Lindsay A.C., Obaid D.R., Falk E. and Rudd J.H.F. *Non-invasive imaging of atherosclerosis.* European Heart Journal – Cardiovascular Imaging (2012); 13:205–218.
15. Zimarino M., Prati F., Marano R., Angeramo F., Pescetelli I., Gatto L., Marco V., Bruno I. and De Caterina R. *The value of imaging in subclinical coronary artery disease.* Vascular Pharmacology (2016); 82:20–29.
16. McAteer M.A. and Choudhury R.P. *Targeted molecular imaging of vascular inflammation in cardiovascular disease using nano- and micro-sized agents.* Vascular Pharmacology (2013); 58:31–38.
17. Quillard T. and Libby P. *Molecular imaging of atherosclerosis for improving diagnostic and therapeutic development.* Circulation Research (2012); 111:231-244.
18. Tarkin J.M., Dweck M.R., Evans N.R., Takx R.A.P., Brown A.J., Tawakol A., Fayad Z.A. and Rudd J.H.F. *Imaging atherosclerosis.* Circulation Research (2016); 118:750-769.
19. Albelda M.T., Garcia-Espana E. and Frias J.C. *Visualizing the atherosclerotic plaque: a chemical perspective.* Chemical Society reviews (2014); 43(8):2858.
20. Evans N.R., Tarkin J.M., Chowdhury M.M., Warburton E.A. and Rudd J.H.F. *PET imaging of atherosclerotic disease: advancing plaque assessment from anatomy to pathophysiology.* Current Atherosclerosis Reports (2016); 18: 30.
21. Ulyanova T., Scott L.M., Priestley G.V., Jiang Y., Nakamoto B., Koni P.A. and Papayannopoulou T. *VCAM-1 expression in adult hematopoietic and nonhematopoietic cells is controlled by tissue-inductive signals and reflects their developmental origin.* Blood (2005); 106:86-94.
22. Tsourkas A., Shinde-Patil V.R., Kelly K.A., Patel P., Wolley A., Allport J.R. and Weissleder R. *In Vivo imaging of activated endothelium using an anti-VCAM-1 magnetooptical probe.* Bioconjugate Chemistry (2005); 16(3):576-581.
23. Kelly K.A., Allport J.R., Tsourkas A., Shinde-Patil V.R., Josephson L. and Weissleder R. *Detection of vascular adhesion molecule-1 expression using a novel multimodal nanoparticle.* Circulation research (2005); 96:327–336.
24. Nahrendorf M., Jaffer F.A., Kelly K.A., Sosnovik D.E., Aikawa E., Libby P. and Weissleder R. *Noninvasive vascular cell adhesion molecule-1 imaging identifies*

inflammatory activation of cells in atherosclerosis. Circulation (2006); 114:1504–1511.

25. Kelly K.A., Nahrendorf M., Yu A.M., Reynolds F. and Weissleder R. *In vivo phage display selection yields atherosclerotic plaque targeted peptides for imaging.* Molecular Imaging and Biology (2006); 8:201–207.
26. Nahrendorf M., Keliher E., Panizzi P., Zhang H., Hembrador S., Figueiredo J.L., Aikawa E., Kelly K., Libby P. and Weissleder R. *^{18}F-4V for PET-CT imaging of VCAM-1 expression in inflammatory atherosclerosis.* JACC: Cardiovascular Imaging (2009); 2(10):1213–1222.
27. Dimastromatteo J., Broisat A., Perret P., Ahmadi M., Boturyn D., Dumy P., Fagret D., Riou L.M. and Ghezzi C. *In vivo molecular imaging of atherosclerotic lesions in ApoE$^{-/-}$ mice using VCAM-1–specific, ^{99m}Tc-labeled peptidic sequences.* The Journal of Nuclear Medicine (2013); 54:1–8.
28. Broisat A., Hernot S., Toczek J., De Vos J., M. Riou L.M., Martin S., Ahmadi M., Thielens N., Wernery U., Caveliers V., Muyldermans S., Lahoutte T., Fagret D., Ghezzi C. and Devoogdt N. *Nanobodies targeting mouse/human VCAM1 for the nuclear imaging of atherosclerotic lesions.* Circulation research (2012); 110:927-937.
29. Paganelli G. and Chinol M. *Radioimmunotherapy: is avidin-biotin pretargeting the preferred choice among pretargeting methods?* European Journal of Nuclear Medicine and Molecular Imaging (2003); 30(5):773–776.
30. Sakahara H. and Saga T. *Avidin–biotin system for delivery of diagnostic agents.* Advanced Drug Delivery Reviews (1999); 37:89–101.
31. Yao Z., Zhang M., Kobayashi H., Sakahara H., Nakada H., Yamashina I. and Konishi J. *Improved targeting of radiolabeled streptavidin in tumors pretargeted with biotinylated monoclonal antibodies through an avidin chase.* The Journal of Nuclear Medicine (1995); 36:837-841.
32. Paganelli G., Belloni C., Magnani P., Zito F., Pasini A., Sassi I., Meroni M., Mariani M., Vignali M., G. Siccardi A.G. and Fazio F. *Two-step tumour targeting in ovarian cancer patients using biotinylated monoclonal antibodies and radioactive streptavidin.* European Journal of Nuclear Medicine (1992); 19:322-329.

33. Prakash S., Hazari P.P., Meena V.K., Jaswal A., Khurana H., Kukreti S. and Mishra A.K. *Biotinidase resistant ^{68}Gallium-radioligand based on biotin/avidin interaction for pretargeting: synthesis and preclinical evaluation.* Bioconjugate Chemistry (2016); 27(11):2780−2790.
34. Wilbur D.S., Hamlin D.K., Chyan M.K., Kegley B.B. and Pathare P.M. *Biotin reagents for antibody pretargeting. 5. Additional studies of biotin conjugate design to provide biotinidase stability.* Bioconjugate Chemistry (2001); 12:616-623.
35. Szalecki W. *Synthesis of norbiotinamine and its derivatives.* Bioconjugate Chemistry (1996); 7:271-273.
36. Foulon C.F., Alston K.L. and Zalutsky M.R. *Synthesis and preliminary biological evaluation of (3-iodobenzoyl) norbiotinamide and ((5-iodo-3-pyridinyl)carbonyl) norbiotinamide: two radioiodinated biotin conjugates with improved stability.* Bioconjugate Chemistry (1997); 8:179-186.
37. Wilbur D.S., Hamlin D.K., Pathare P.M. and Weerawarna S.A. *Biotin reagents for antibody pretargeting: synthesis, radioiodination, and in vitro evaluation of water soluble, biotinidase resistant biotin derivative.* Bioconjugate Chemistry (1997); 8:572–584.
38. Wilbur D.S., Pathare P.M., Hamlin D.K., Buhler K.R. and Vessella R.L. *Biotin reagents for antibody pretargeting: III. Synthesis, radioiodination, and evaluation of biotinylated starburst dendrimers.* Bioconjugate Chemistry (1998); 9:813–825.
39. Wilbur D.S., Chyan M.K., Pathare P.M., Hamlin D.K., Frownfelter M.B. and Kegley B.B. *Biotin reagents for antibody pretargeting: IV. Selection of biotin conjugates for in vivo application based on their dissociation rate from avidin and streptavidin.* Bioconjugate Chemistry (2000); 11:569–583.
40. Wilbur D.S., Hamlin D.K., Chyan M.K., Kegley B.B. and Pathare P.M. *Biotin reagents for antibody pretargeting: V. Additional studies of biotin conjugate design to provide biotinidase stability.* Bioconjugate Chemistry (2001); 12:616–623.
41. Song H.Y., Ngai M.H., Song Z.Y., MarcAry P.A., Hobley J. and Lear M.J. *Practical synthesis of maleimides and coumarin-linked probes for protein and antibody labeling via reduction of native disulfides.* Organic & Biomolecular Chemistry (2009); 7:3400-3406.

42. Parodi F. *Isocyanate-derived polymers.* Comprehensive Polymer Science Vol.5 (Step Polymerization). Eds.; Pergamon: Oxford (1989); 23:387-412.
43. Kastrinsky D.B. and Barry C.E. III. *Synthesis of labeled meropenem for the analysis of M. tuberculosis transpeptidases.* Tetrahedron Letters (2010); 51:197-200.
44. Shafer D.E., Inman J.K. and Lees A. *Reaction of Tris(2-carboxyethyl)phosphine (TCEP) with maleimide and α-haloacyl Groups: anomalous elution of TCEP by gel filtration.* Analytical Biochemistry (2000); 282:161–164.
45. Burns J.A., Butler J.C., Moran J. and Whitesides G.M. *Selective reduction of disulfides by tris(2-carboxyethyl)phosphine.* Journal of organic chemistry (1991); 56:2648-2650.
46. Kantner T. and Watts A.G. *Characterization of reactions between water-soluble trialkylphosphines and thiol alkylating reagents: implications for protein-conjugation reactions.* Bioconjugate Chemistry (2016); 27:2400−2406.
47. Getz E.B., Xiao M., Chakrabarty T., Cooke R. and Selvin P.R. *A comparison between the sulfhydryl reductants tris(2-carboxyethyl)phosphine and dithiothreitol for use in protein biochemistry.* Analytical Biochemistry (1999); 273:73-80.
48. Fontaine S.D., Reid R., Robinson L., Ashley G. W. and Santi D.V. *Long-term stabilization of maleimide−thiol conjugates.* Bioconjugate Chemistry (2015); 26:145−152.
49. Tyagarajan K., Pretzer E. and Wiktorowicz J.E. *Thiol-reactive dyes for fluorescence labeling of proteomic samples.* Electrophoresis (2003); 24:2348–2358.
50. Nair D.P., Podgórski M., Chatani S., Gong T., Xi W., Fenoli C.R. and Bowman C.N. *The thiol-Michael addition click reaction: a powerful and widely used tool in materials chemistry.* Chemistry of materials (2014); 26:724−744.
51. Wysocki V.H., Resing K.A., Zhang Q. and Cheng G. *Mass spectrometry of peptides and proteins.* Methods (2005); 35:211-222.
52. Dupré M., Cantel S., Martinez J. and Ennjalbal C. *Occurrence of C-terminal residue exclusion in peptide fragmentation by ESI and MALDI tandem mass spectrometry.* Journal of the American Society for Mass Spectrometry (2012); 23:330-346.
53. Liu S. *The role of coordination chemistry in the development of target specific radiopharmaceuticals.* Chemical Society Reviews (2004); 33:445–461.

54. Bhattacharyya S. and Dixit M. *Metallic radionuclides in the development of diagnostic and therapeutic radiopharmaceuticals.* Dalton Transactions (2011); 40:6112–6128.
55. Price E.W. and Orvig C. *Matching chelators to radiometals for radiopharmaceuticals.* Chemical Society Reviews (2014); 43:260.
56. Caviglioli G., Parodi B., Cafaggi S., Russo E., Cirrincione P., Chinol M. and Paganelli G. *A conjugate of human albumin and 2-(4-isothicyanatobenzyl)-1,4,7,10-tetraazacyclododecane-1,4,7,10-tetraacetic acid useful for the localization of radionuclides for diagnostic and therapeutic purposes.* PCT UGE003BWO; 2011.
57. *International Pharmacopeia, Radiopharmaceuticals: general monograph.*
58. Cyran C.C., Paprottka P.M., Eisenblätter M., Clevert D.A., Rist C., Nikolaou K., Lauber K., Wenz F., Hausmann D., Reiser M.F., Belka C. and Niyazi M. *Visualization, imaging and new preclinical diagnostics in radiation oncology.* Radiation Oncology (2014); 9:3.
59. Ziegler S.I. *Positron Emission Tomography: principles, technology, and recent developments.* Nuclear Physics A (2005); 752:679c–687c.
60. Jalilian A.R. *An overview on Ga-68 radiopharmaceuticals for positron emission tomography applications.* Iranian journal of nuclear medicine (2016); 24(1):1-10.
61. Kilian K. *^{68}Ga-DOTA and analogs: current status and future perspectives.* Reports of practical oncology and radiotherapy (2014); 19:S13–S21.
62. Pratesi A., Bucelli F., Mori I. Chinol M., Verdoliva A., Paganelli G., Rivieccio V., Gariboldi L. and Ginanneschi M. *Biotin derivatives carrying two chelating DOTA units. Synthesis, in vitro evaluation of biotinidases resistance, avidin binding, and radiolabeling tests.* Journal of medicinal chemistry (2010); 53(1):432–440.
63. Light-Wahl K.J., Schwartz B.L. and Smith R.D. *Observation of the noncovalent quaternary associations of proteins by electrospray ionization mass spectrometry.* Journal of the American Chemical Society (1994); 116:5271-5278.
64. Schwartz B.L., Light-Wahl K.J. and Smith R.D. *Observation of noncovalent complexes to the avidin tetramer by electrospray ionization mass spectrometry.* Journal of The American Society for Mass Spectrometry (1994); 5:201-204.

65. Eckart K. and Syiess J. *Electrospray ionization mass spectrometry of biotin binding to streptavidin.* Journal of the American Society for Mass Spectrometry (1995); 6:912-919.